Rigid block analysis of masonry structures with geometrical and material nonlinearity

Department of Architecture, Construction and Design
Ph.D. Program in
DESIGN FOR HERITAGE:
KNOWLEDGE AND LANDSCAPE
SSD: ICAR/08–SCIENZA DELLE COSTRUZIONI

Final Dissertation

Rigid Block Analysis of Masonry Structures with Geometrical and Material Nonlinearity

---

by
Elena Di Mare

Supervisors:

Prof. Mario Daniele Piccioni
Prof. Aguinaldo Fraddosio
Prof. Elio Sacco

Coordinator of Ph.D. Program:
Prof. Carlo Moccia

Course XXXVI, 01/11/2020-23/04/2024

Rigid Block Analysis of Masonry Structures with Geometrical and Material Nonlinearity

by Elena Di Mare

Table of contents

List of Figures

List of Tables

Abstract

Structural modeling of masonry constructions is a critical area of research, essential for preserving the architectural heritage worldwide, and for the structural safety of a high number of contemporary buildings.

Rigid block models prove to be an effective approach, especially for historic masonry constructions. They can effectively represent the effects of the high compressive strength and the low deformability of the blocks in comparison to the low strength and stiffness of joints. The nonlinear response of masonry structures substantially depends on the behavior of the interfaces due to unilateral contact and frictional effects. Moreover, the evolution of mechanisms in masonry structures involves finite rotations, and therefore large displacements, a further source of structural nonlinearity. Neglecting large displacements by approximating the deformed configuration by the undeformed one might lead to non-negligible errors.

The above modeling choices are adopted in the distinct element method [6], also implemented in some well-known commercial software. However, these codes are not specifically conceived for masonry structures but for simulating the mechanical behavior of granular materials such as soil, rocks, and powders. This motivates ongoing research on the development of rigid block models directly aimed at the structural assessment of masonry structures [73, 79].

In this context, a masonry rigid block model is proposed, based on a careful determination of the tangent stiffness interface matrix in presence of geometrical and material nonlinearity [64, 86]. This innovative approach can be approximated and simplified in the case of moderate rotations in large displacements [19, 22].

In particular, a consistent formulation for a 2D interface model in large displacements is established by introducing a co-rotational reference system coincident with the middle-line between the two deformed sides of the interface shared by two rigid blocks.

A numerical procedure, based on the backward Euler time-integration scheme, is introduced, and the time step is solved adopting a displacement driven predictor-corrector

algorithm. For the solution, the classical iterative Newton-Raphson scheme is adopted by linearizing nonlinear terms.

The model is discussed through numerical simulations on different masonry structures, conducted in both displacement control and arc-length control scenarios. The results include a comparison of solutions obtained with finite rotation and moderate rotation theories.

Keywords: Masonry, Distinct element modeling, Rigid block modeling, Geometrical nonlinearity, Damage-friction

1 Introduction

Modeling decohesion between interconnected mechanical components or analyzing the initiation and propagation of fractures is a complex task in advanced failure mechanics applied to materials and structures. Decohesion experiencing large displacements occurs across a diverse field of applications.

In many engineering scenarios, material nonlinearity concentrates in small regions bounded by thin layers where substantial strain gradients are present. These layers are often so small that they can be substituted in mathematical formulations with an interface model with zero thickness. Constitutive relationships define the connection between stresses acting on the interface and discontinuities in displacement, forming the basis of interface models.

To effectively handle coupled geometrical and material nonlinearities, it is essential to have interface elements formulated for large displacements. This study proposes a cohesive interface model specifically designed for large displacement analyses in masonry structures composed of rigid elements.

Rigid block models prove to be an effective approach especially for historic masonry constructions, since can effectively represent the effects of the high compressive strength and the low deformability of the blocks with respect to the low strength and stiffness of joints, where deformability is concentrated.

This dissertation is based on the Cohesive Zone Model (CZM) introduced by Dugdale [1] and Barenblatt [2]. Originally implemented to analyze the area before a crack tip, this model has become a versatile tool for various applications, all linked by the fundamental concept of a mechanical interface. CZMs have become essential components in computational frameworks, especially in the nonlinear finite/discrete element method. CZMs are widely used due to their adaptability in addressing various fracture states and their ease of numerical implementation. This facilitates the integration of interface elements into both research and commercial codes.

The above modeling choices are adopted in the distinct/discrete element method

(DEM) [6]. Upon reviewing the scientific literature, it is evident that standard finite element (FE) codes can be utilized to achieve discontinuum idealizations by incorporating joint [8, 33] or interface elements [58]. This approach allows for the representation of masonry as a continuous material that is divided by joints. On the other hand, DEMs view the material as an assembly of distinct bodies, i.e., the masonry units, that interact along their boundaries. The line between finite and discrete element codes has become less clear as these methods have adopted features from one another. For instance, blocks in discrete element models no longer need to be assumed rigid and may have internal finite element meshes. Similarly, finite element models are being utilized to represent discontinuities at smaller scales, such as using joint elements to partition bricks into small polygonal particles to study fracturing. A review of the main models based on the discrete element and related numerical techniques for the analysis of masonry is presented in the work of Lemos [54].

Nowadays, DEM is implemented in some well-known commercial software. However, these codes for performing structural analysis of masonry constructions seem to be a closed system. Users are limited to choices in terms of constitutive laws and analysis approaches determined by the software owner. In such cases, it becomes difficult to understand the results of the analysis or, worse, there is a risk of obtaining results that do not accurately represent the behavior of the structures. Ongoing research is being conducted to develop rigid block models specifically for the structural assessment of masonry structures [73, 79]. In this context, the challenge is to formulate a DEM code specifically suited for studying the behavior of masonry constructions, considering the nonlinear response of masonry structures.

This dissertation proposes a numerical approach for studying large displacements within a 2D framework by introducing a cohesive interface model that combines damage and friction, an innovative constitutive model in the context of DEM commercial software. The approach employs rigid block elements and cohesive zone models.

Among all DEMs, the use of the rigid block model provides a new perspective on

fracture mechanics. This is based on experimental and phenomenological evidence for masonry, where the study of the interface is more important than the deformability of each block.

The cohesive interface model combining damage and friction, initially developed by Alfano and Sacco [51], undergoes further development to accommodate large displacements for rigid blocks. When blocks experience significant rotations, the problems become markedly nonlinear, potentially introducing issues related to solution convergence and causing a significant slowdown in analysis time due to increased computational demands. After a thorough exploration of the scientific literature pertaining to the DEM, a potential error mitigation strategy is identified by incorporating a second-order approximation of sine and cosine functions associated with rotations within the rotation matrix [28, 30, 35]. To address this, before introducing finite rotations, an error mitigation technique is employed through the implementation of the Moderate Rotations approximation [19]. This method expands the series of sine and cosine functions of the rotation of each block's centroid within the rotation matrix. Although the problem is inherently nonlinear, this approach could help reduce the computational burden associated with the analysis.

The objective of this dissertation is concerned with the development of a rigid block model with a consistent interface element procedure for taking into account the combined effect of friction and damage when large displacements occur. Because the code is developed and implemented in-house, users can switch between finite rotations, moderate rotations, and small displacements depending on the nature of the problem and structure.

After presenting the kinematics of rigid blocks and the interface, the consistent derivations begin with the analysis of the interface contribution to the discrete version of the Principle of Virtual Work of the whole structural system, followed by linearization. As shown in the next sections, the resulting derivation leads to a simple and compact operational formulation in which the geometrical and the material contribution to the

element stiffness matrix are clearly identified. In addition to this, one of the most appealing aspects of the model herein proposed relies on its formulation within three scenarios: large displacements involving finite rotations, large displacements considering the approximation of moderate rotations, and small displacements. The numerical procedures for the three cases are presented.

The dissertation is organized as follows.

In Section 2, the motivations of the presented work are illustrated, highlighting the difficulties in the study of nonlinear problems, which allows difficulties in the choice of formulation models for masonry structures.

In Section 3 mechanical models including nonlinearity are discussed, with a specifical attention regarding the startegy adopted for study the mechanical behavior of masonry structures. Two main topics are discussed in detail: rigid block models and interface models.

In Section 4 the governing equations of the 2D-Rigid Block Model with Interfaces are presented: rigid block and interface kinematics, and equilibrium equations are formulated. The constitutive models used in the investigation are outlined in Section 5, with a specific enphasis on the CZM combining damage and friction. Section 6 addresses the main issues regarding the numerical procedure, based on the backward Euler time-integration scheme. The time step is solved by adopting a displacement-driven predictor-corrector algorithm. For the solution, the classical iterative Newton-Raphson scheme is employed to linearize nonlinear terms.

The algorithm is then validate through numerical simulations presented in Section 7 concerning masonry structures, with particular emphasis on arch structures, conducted under both displacement control and arc-length control scenarios. The same simulations are performed with finite rotations and moderate rotations, and are compared with limit analysis and small displacement scenarios.

2 General Aspects

The model proposed in this dissertation addresses two intricate challenges. Firstly, it tackles the complexities associated with the study of nonlinear phenomena, which are fundamental for understanding the real behavior of structures in various engineering applications. Secondly, it explores the intrinsic difficulties posed by masonry as a material, which is inherently complex. The coexistence in the literature of different modeling approaches underscores the complexity of modeling nonlinear phenomena in masonry structures [76].

This section contextualizes the motivations behind the exploration of this field, considering the abundance of articles addressing mechanical models for the study of both geometrical and material nonlinear phenomena in scientific literature from the 1960s to the present day, as demonstrated by the provided references. Research on modeling nonlinearity in masonry structures continues to investigate the interaction between geometrical and material nonlinearities, an aspect not yet rigorously analyzed in the related literature.

2.1 Introduction to Nonlinear Problems

The field of structural engineering poses many nonlinear problems, such as those resulting from material responses, geometric complexities, and contact interactions. This introductory exploration aims to clarify the nature of structural nonlinearity before discussing the linearization process that occurs under specific assumptions:

1. Linear material response: The structure's material responds linearly to changes in applied loads. This means that stress and deformation are directly proportional, as shown by the stress-strain curve represented by a straight line.

2. Small displacements and deformations: The governing equations can be formulated in the structure's undeformed configuration, although the equilibrium is

achieved in a deformed configuration. It is important to note that small deformations may not necessarily correspond to small displacements. For example, rigid body movements can result in large displacements with deformations equal to zero. Therefore, the assumption of small displacements is relaxed to explore phenomena such as stability analysis, which is beyond the scope of linear theory.

3. Bilateral constraints: Constraints within the structure are considered bilateral.

If these assumptions are met, the structural problem can be effectively addressed using the linear theory of structures, offering simplified resolution and facilitating the derivation of analytical or semi-analytical solutions. It is possible to demonstrate that, under mild constitutive restrictions, (i) a unique solution to the structural problem exists, (ii) the total potential energy of the system, composed of material and a set of applied loads, is defined.

However, linear theory is less representative when dealing with problems that involve large displacements, significant deformations, or nonlinear material behaviors. In such complex scenarios, nonlinear approaches are necessary to obtain more accurate and realistic solutions.

The following subsections will discuss the three main types of nonlinearity sources in structural problems: material nonlinearity, geometrical nonlinearity, and contact nonlinearity.

The purpose of this analysis is to explain the complexities of structural behavior beyond linear assumptions and address the computational challenges of solving nonlinear problems, while acknowledging the absence of solution uniqueness.

2.1.1 Material Nonlinearity

Material nonlinearity plays a crucial role in structural analysis and engineering design. It refers to the nonlinear behavior exhibited by a material, which can vary in response to factors such as current deformations, deformation history, deformation rate, temper-

ature, pressure, and other influential parameters. The variability of material behavior under different stress levels adds complexity to mathematical models used to describe it.

Nonlinear material models are widely used in engineering applications, such as accommodating large strain behavior in (visco)elasto-plasticity and hyperelasticity, which are particularly suitable for rubber and rubber-like materials. To ensure safe and reliable design of structures and engineering components subjected to complex loading scenarios, it is essential to conduct a comprehensive investigation into how materials respond considering nonlinear effects.

In Bathe's formulation [63], there are two types of analyses: those that consider only material nonlinearity and those that also address the effects of geometrical nonlinearity. By analyzing the first case, the formulation can be used to categorize cases of purely material nonlinearity, which involve infinitesimal displacements and strains with a nonlinear stress-strain relation. Conventional engineering stress and strain measures can be used to describe the response.

When small displacements, rotations, and deformations (SD-SR-SS) occur with nonlinear material behavior, this scenario is analyzed using materially nonlinear-only analysis (MNO), as shown in Table 1. The only nonlinearity stems from the relationship between stresses and deformations.

Table 1: Classification of nonlinear analyses [63].

Definition	**Kinematics**	**Stress-strain Relationships**	**Formulation Used**	**Stress-Strain Measures**
Material Nonlinearity	SD-SR-SS	NL	MNO	Eng. stress and strain
Geometrical Nonlinearity (i)	LD-LR-SS	LIN or NL	TL UL	IIPK, GL C, A
Geometrical Nonlinearity (ii)	LD-LR-LS	LIN or NL	TL UL	IIPK, GL C, log

2.1.2 Geometrical Nonlinearity

Geometrical nonlinearity becomes evident when the magnitude of displacements significantly affects the structural response.

During a seismic event, geometrical nonlinearity can manifest in different scenarios. In the context of Bathe's conventional classification [63], two predominant cases emerge: large displacements, large rotations but small strains (LD-LR-SS), or large displacements, large rotations, and also large strains (LD-LR-LS).

In the first scenario, the material undergoes large rigid body displacement and rotations, but is essentially subjected to infinitesimally small strains (LD-LR-SS) measured in a body-attached coordinate frame. The stress-strain relationship of the material can exhibit linearity or nonlinearity. In this setting, two alternative "Lagrangian" formulations are used to describe the deformation process based on a reference configuration. The Updated Lagrangian (UL) formulation is employed when the reference configuration undergoes updates at each step of the time-dependent analysis. The UL formulation utilizes the Cauchy (C) tensor as the stress measure and the Almansi (A)

tensor as the strain measure, providing insight into the evolving material response. On the other hand, the Total Lagrangian (TL) formulation is useful when the reference configuration remains unchanged and aligns with the undeformed configuration. In this case, the stress can be measured using the second Piola-Kirchhoff (IIPK) tensor, and the strain can be measured using the Green-Lagrange (GL) tensor.

In the second, more general case, the material undergoes large displacements, rotations, and strains (LD-LR-LS). The stress-strain relation typically exhibits nonlinearity. The UL and TL formulations are applicable in this scenario, with no restrictions on the magnitudes of displacements and deformations. In the UL formulation, the Cauchy (C) tensor can be used as the stress measure, and the logarithmic (log) tensor can be used as the deformation measure. In the TL formulation, the stress can be measured using the second Piola-Kirchhoff (IIPK) tensor, while the deformation can be characterized by the Green-Lagrangian (GL) tensor.

A revised summary of Bathe's work is presented in the Table 1, utilizing the symbols described above (i.e., LD = Large Displacements).

Scenarios involving geometrical linearity or nonlinearity effects can be described as follows:

- Small displacements that do not affect equilibrium conditions fall under the first-order theory, where equilibrium equations are formulated in the undeformed configuration.
- Small displacements but influential to equilibrium conditions, known as the second-order theory, where equilibrium is assessed in the deformed configuration.
- Large displacements but small deformations. Notably, within this group, the case where deformations are negligible is emphasized, representing the displacement of a rigid body with finite rotations.
- Large displacements and large deformations.

In particular, large displacements are studied by considering both finite rotations and moderate rotations. The distinction between finite rotations and moderate rotations lies in the magnitude of the rotations involved. Finite rotations typically represent larger angular displacements, while moderate rotations refer to smaller angular displacements. Implementing both finite and moderate rotations in nonlinear analyses allows for selecting of the most suitable type for studying structures in large displacements, depending on the nature of the problem being addressed. Using both theories provides a more comprehensive analysis of structural behavior under large displacements [11, 25, 84].

In this scenario, another type of formulation comes into play: the Co-rotational (CR) model. In the context of Lagrangian formulations, the CR case can be viewed as a variant of the Total Lagrangian formulation.

The TL formulation maintains the reference configuration, which is the undeformed configuration. On the other hand, the CR formulation considers locally co-rotated rotations, providing a more precise description of the structure's behavior during large rotations. Both formulations maintain the reference configuration unchanged, but the CR case includes a specific consideration of co-rotated rotations [38]. In Lagrangian kinematics, the TL, UL, and CR descriptions follow the body or element as it moves. The deformed configuration is any configuration taken during the analysis process and does not need to be in equilibrium. It is also referred to as the current, strained, or spatial configuration in the literature. The CR description introduces a new component by splitting the motion tracking into two parts (see Fig. 1):

(i) The base configuration, which serves as the origin of the displacements. The starting configuration of the body at the beginning of the analysis is referred to as the initial or undeformed configuration. In the literature of continuum mechanics, this is also known as the material configuration.

(ii) The co-rotated configuration varies from element to element and, in some CR variants, from node to node. The CR configuration of each element is obtained by a rigid

body motion of the element's base configuration. The coordinate system used is Cartesian and follows the element like a "shadow" or "ghost". Deformations of the element are measured with respect to the CR configuration.

In general, there has been some confusion in the literature regarding the differences between the CR and UL formulations. First, the Co-rotational formulation has an advantage over the Updated (and Total) Lagrangian approach in that the number of degrees of freedom involved in the formulation at the element level is reduced by the number of rigid body modes. Another important advantage of the CR formulation is that the volume integrations are generally performed over the simple undeformed shape of the element. In contrast, a strict implementation of the UL formulation requires the integrations to be performed over the complicated deformed shape of the element at the last computed configuration.

Based on the existing literature, the CR case has been properly formulated and extended to include nonlinear geometry effects in interface elements [37, 40]. Displacement, strain and stress quantities for the general deformed configuration are related to the mid-plane of the interface, which is assumed to be a co-rotating reference plane. Element kinematics and equilibrium conditions are imposed with respect to this plane. This aspect will be discussed below.

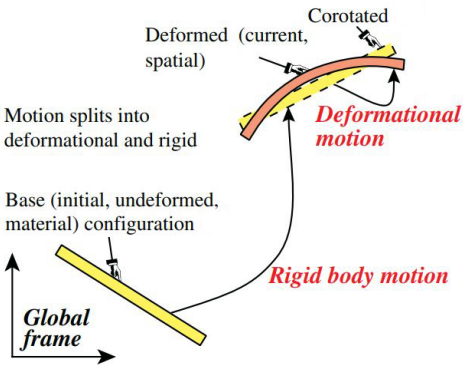

Figure 1: The CR kinematic description. Deformation from co-rotated to deformed (current) configuration [38].

2.1.3 Contact Nonlinearity

Beyond the analysis categories detailed in Table 1, another type of nonlinear analysis addresses scenarios in which boundary conditions undergo alterations during the motion of the considered body. Generally, changes in boundary conditions leading to contact nonlinearity may occur in any of the problems listed in Table 1.

Contact nonlinear analysis is a pivotal aspect of structural studies, particularly when considering scenarios involving surfaces that come into contact and interact during the motion of the considered body. In these analyses, alterations in boundary conditions may lead to significant changes in structural response.

The examples below demonstrate instances where contact nonlinearity is evident, appearing in both geometrical and material nonlinear analyses.

- Significant Deformations: In cases marked by substantial deformations or displacements, surfaces within a structure may engage in contact and subsequent separation. It is important to handle these contact interactions accurately to achieve reliable and realistic analytical outcomes.

- Unilateral Contact Analysis: Unilateral contact occurs when one surface can exert influence on the other without reciprocal effects. Accurate analysis of unilateral contact requires specialized methodologies within nonlinear analyses. For example, in the case of masonry structures, implementing no-tension behavior, which is typical of some masonry constructions, is a nonlinear contact case. The following section will detail the last aspect of constitutive models of masonry.

- Friction Phenomena: Frictional forces often accompany contact phenomena and significantly influence structural behavior. Therefore, a meticulous analysis of contact and friction is indispensable for a comprehensive understanding of how these forces manifest within the structure. For instance, CZMs consider this aspect before implementation.

The study of contact becomes particularly important when employing discontinuous modeling methods such as the Finite Element Method (FEM) or Discrete Element Method (DEM) [23]. These methods typically use the point contact hypothesis to represent the interaction between blocks through contact points. Each force is a function of the relative block displacement at that point. For instance, an edge-edge contact is simulated by two point contacts. This approach is advantageous due to its generality and simplicity, as it can handle various types of geometric interaction and permit large displacements. This approach enables a seamless transition between face-to-face contact and point contact, such as the interaction between a vertex and a face. However, joint elements of FE codes cannot address vertex-edge contacts. Point contacts have the added advantage of allowing independent meshing of blocks without the need to match nodal points.

Several DE codes use edge-edge formulations for contact representation instead of point contacts. In this case, the contact surface is discretized into interacting line segments for each block. This allows for a linear variation of stresses on the contact surface. This hypothesis typically improves contact stress results, but it requires careful treatment of some situations that arise in large motion problems. When an edge-edge interaction changes to vertex-edge or vice versa, it is important to ensure continuity of interaction forces to prevent negative numerical effects.

When dealing with nonlinear contact problems, the computational cost of analyses can become significant. In discrete modeling codes, deformable contact approaches are commonly preferred [54]. Penalty coefficients for normal and shear contact stiffness allow users to specify the maximum allowable overlap size. Accurate contact representation is crucial for obtaining reliable results, especially in scenarios involving significant deformations, unilateral contact, and friction phenomena.

2.2 Masonry

The study of masonry is essential for preserving historic and cultural buildings because it is widely used in architectural heritage. It is also crucial for ensuring the structural safety of many contemporary buildings worldwide. Masonry is currently recognized for its intricate nonlinear mechanical properties, making it a significant area of research.

The story of masonry spans from ancient wonders to modern marvels, showcasing human endeavor, engineering prowess, and artistic flair. Masonry has been a significant construction technique throughout history, from early Mesopotamian civilizations to innovative ancient Roman structures, and from soaring Gothic constructions to immense Renaissance domes.

Since the beginning of civilization, approximately 10,000 years ago, humans have constructed permanent shelters and houses, marking the end of nomadic life. In ancient and medieval times, houses were built using natural materials found nearby, such as clay, stone, wood, and earth. As the need for taller and more resilient dwellings grew, masonry emerged as one of the most durable and efficient building techniques of all time. In areas where stone was scarce, earth was also used as a building material.

The oldest masonry structures have been found in the region of Israel (Mesopotamia) and date from 9000 to 8000 BC. Masonry fortified walls in Jericho (7000 B.C.) and rectangular brick houses in Çatal-Húyük, Anatolia (6500 B.C.) have also been found.

The simplicity of its manufacturing process and the availability of raw materials (earth, clay, stone) made it the most used, ancient and widespread construction technique. Despite the simplicity of the construction process, it is highly durable, resistant and flexible, which proved to be a very successful construction technique. Stone, brick or adobe units are laid on top of each other by hand, dry laid or bonded with mortar. The strength of the structure depends on the strength and cohesion of the units. It can be built with a single material or with a mixture of materials, can have several layers of different constitution and can use elements of different sizes. The main materials used to built masonry are: stone, clay brick, adobe and lime mortar. Early masonry

structures were built with locally found materials, because the scarcity of one material would force the adoption of a particular one. Later, the development of transportation and the evolution of civilization led to the use of specific materials according to their use, the type of building (public, military, residential) and the wealth of the owner. In general, historical masonry that has survived to the present day has the following characteristics: (i) the use of adobe and clay bricks and stone blocks with mortar to bind the units together or (ii) the use of dry joints (no mortar) stone masonry that relies on friction between the stones to remain stable.

Dry masonry is a construction technique that relies on precise placement of individual elements to ensure the integrity of the structure, without the use of mortar. However, the use of mortar became more widespread starting in the 4th century BC. Historical constructions, including large-scale structures, often used the technique of assembling blocks without mortar [61]. Dry masonry examples can still be found today, especially in rural areas of certain geographic regions. In the history of construction, there are other examples of masonry construction techniques. When two external façades, usually made of brick or stone elements, are bound together with a filling material, it is called rubble masonry. The ancient Roman technique, opus caementicium, is another example. Fig. 2 schematically illustrates the most important construction phases.

Masonry's evolution, adaptation to various cultures, and enduring influence on architectural design demonstrate remarkable structural integrity. This exploration reveals the rich history of masonry and explains why it continues to be relevant in modern architectural practices [29, 88].

Experts have recently reevaluated the performance of masonry, specifically its resistance to the effects of time. However, unlike steel and reinforced concrete, which have established safety methods of structural analysis, this building material does not have a well-defined structural model. The Italian building codes (D.M. 17/01/2018: Norme Tecniche per le Costruzioni - NTC2018 and Circolare 21/01/2019) define ma-

sonry constructions as vertical load-bearing structures made with masonry systems that can withstand vertical and horizontal forces. These structures are connected by floor structures at each level, possibly inclined in the roof, and by foundations. This technique is allowed for both simple and reinforced construction, even in seismic zones. The European building codes (EN 1996: Design of masonry structures) rigidly follow the elastic approach, even when it may not be the most suitable. Models are proposed that are modified from those used for concrete and steel framed structures to apply to masonry.

Although modeling and using masonry material in design can be challenging, it offers significant advantages that make it worthwhile. The simplicity of masonry construction is its hallmark. Stacking stones or bricks, with or without mortar, is a straightforward and effective approach that has stood the test of time. Therefore, masonry is still used in modern building practices. Additional important attributes include aesthetics, structural integrity, low maintenance, adaptability, acoustic absorption, and fire resistance. Structural masonry is a competitive choice for various applications, including load-bearing walls, earthquake-resistant infill panels, pre-stressed masonry cores, and low-rise buildings. However, the potential of innovative structural masonry applications is limited by delayed design guidelines compared to concrete and steel. This is due to a lack of comprehensive understanding and models for the behavior of individual units, joints, and masonry as a complex composite material. Current computational methods rely heavily on empirical and traditional approaches.

Numerical tools for analyzing or designing masonry structures are still an area of active research. Current approaches often struggle to accurately represent masonry behavior, which can make it difficult to apply the results to full-scale structures.

Figure 2: *Architecture: Maçonnerie*: Engravings from Denis Diderot and Jean Baptiste Le Rond d'Alembert: Encyclopédie, ou dictionnaire raisonné des sciences, des arts et des métiers (1751-72).

2.2.1 Conceptual Design

Masonry has been used for thousands of years and has played a crucial role in shaping architectural landscapes. Several authors in the literature emphasize the importance of studying the shape of ancient masonry constructions in order to understand the main characteristics of this material [4, 29, 43, 45, 61].

The history of masonry shows how it has evolved and adapted to different cultures, leaving a lasting impact on architectural design. Masonry techniques can be used to build various types of structures, emphasizing the importance of conceptual design closely linked to the structural function. Each type of structure serves a specific purpose and requires a skilled understanding of masonry principles for successful construction.

Common types of masonry structures include:

- Walls are vertical structures used to enclose or divide spaces. They can be load-bearing, supporting the weight of the structure, or non-load-bearing, serving primarily as partitions. In either case, they serve as essential structural elements, providing support or contributing to in-plane strength by acting as shear walls.

- Masonry foundations are essential for providing a stable base for a structure. They distribute the weight of the building and ensure its structural soundness. Their role in overall stability has been recognized since ancient times. For example, the Colosseum (80 AD) used a ring of concrete and huge stone blocks, 12 meters deep. Similarly, the medieval foundation for Amiens Cathedral was a grid foundation almost 8 meters deep.

- Piers and columns are vertical load-bearing elements that support arches, lintels, or other structural members.

- Arches are curved, load-bearing structures that distribute weight horizontally. They are commonly used in bridges, doorways, and architectural features for their strength and aesthetic appeal. Vaults are curved structures that form a ceiling or roof over a space. They distribute weight along their curved surface and are often used in architectural designs for their structural integrity and visual impact to allow for larger spans.

- Domes are structures that cover a circular or polygonal area, creating large open spaces without the need for supporting columns. They are commonly found in religious buildings such as churches and mosques.

Milani et al. outline a significant transformation in architectural engineering from corbel arches to double curvature vaults [87]. The development of structures has led to the development of intricate, self-supporting forms that have shaped marvels over time. The corbel arch, an ancient technique that relied on incremental stone or brick layers for construction, had limitations in its capabilities.

The Romans introduced the round arch, which distributed weight effectively, allowing for larger spans and increased stability. The Gothic period introduced the pointed arch, which allowed for even greater height and spaciousness in cathedral interiors. This led to innovations such as rib and groin vaults. In contrast, Roman architecture extensively used barrel vaults, which are semi-cylindrical structures that allow for immense

interior spaces without the need for supporting columns. Examples of this design can be seen in structures like the Pantheon and Hagia Sophia. The double curvature dome showcases the innovative spirit and limitless potential of architectural engineering's arch and vault engineering.

The Greek temples, Lion Gate, and Hooke's hanging chain (see Fig.3) are pioneering examples significant in the principles of masonry construction for different reasons. Greek temples represent a pinnacle of architectural achievement, showcasing advanced techniques in masonry, including precise column placement, intricate friezes, and careful use of entasis (subtle curvature in columns). These elements contribute to the structural integrity and exemplify proportions and aesthetics that are important in ancient Greek architecture. This demonstrates that masonry is not only about load-bearing, but also about achieving a harmonious and visually appealing design.

The Lion Gate at Mycenae showcases early experimentation with architectural forms, featuring a false arch. This pioneering use of structural elements demonstrates an early understanding of load distribution and architectural design principles.

Finally, the catenary is a mathematical curve that represents the natural shape of a suspended chain. Its unique property of experiencing only compression or tension forces, without any bending moment, makes it ideal for constructing arches. In the case of self-weight, structures built according to this curve experience only tensile stresses, such as support ropes in suspension bridges. Alternatively, they experience compressive stresses when the structure has the shape of an inverted catenary, as in dome structures. Arches designed using the catenary shape are structurally efficient, requiring less material and reducing construction costs.

In 1676, Robert Hooke presented an analogy in the form of an anagram: "ut pendet continuum flexile, sic stabit contiguum rigidum inversum". This means that just as a flexible rope hangs, an inverted rigid arch will stand. According to this analogy, the configuration assumed by a suspended rope under certain loads would be the same as that of a slender arch subject to the same loads when inverted. A substantial vein

of research has developed around the important recognition of the "optimal shape" of arches. This research began with Hooke's idea and was further developed by David Gregory on the arch as an inverted catenary [53]. It continued with the initial analytical formalizations of Leibniz, Johann Bernoulli, and Huygens, and culminated in the theoretical studies of Couplet, Bouguer, Bossut, and other 18th century authors [10]. This constitutes one of the most significant moments in reflecting on the relationship between form and structure in constructions.

In the 19th century, the theoretical reflection on building masonry bridges became so significant that it transformed the engineering problem into a metaphysical question of finding a single form that was completely suitable for the role and represented stability. On a more strictly constructive level, the famous creations of Gaudì represent the physical embodiment of the winning logic underlying Hooke's analogy.

These examples demonstrate the diverse nature of masonry, which includes structural stability, aesthetics, and the application of mathematical principles. They emphasize that masonry is not just a utilitarian construction method, but an art form that integrates science, engineering, and design principles.

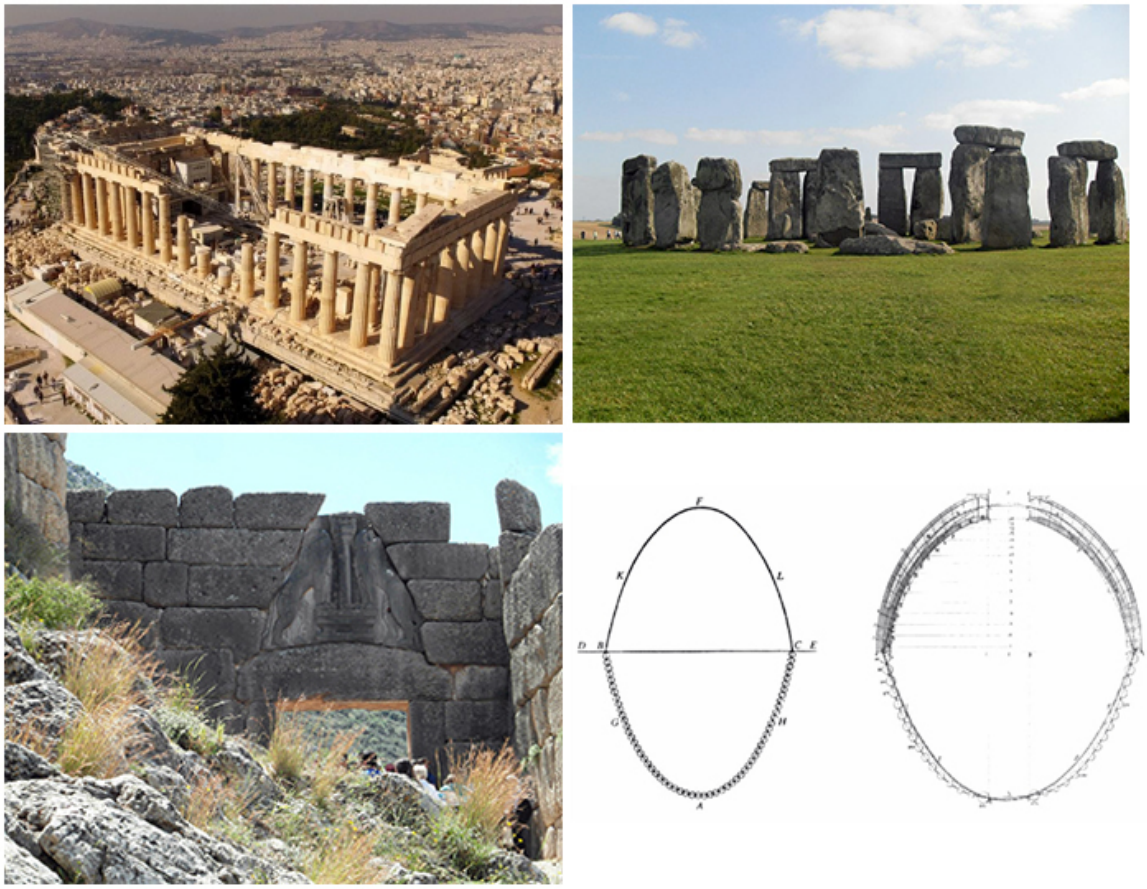

Figure 3: Top: The Parthenon (Acropolis of Athens, Greece, 447 BC 438 BC), despite centuries of wear and damage, remains a symbol of classical architecture. Stonehenge (England, around 2500 BC in the Neolithic period), the trilithon is the most common structure used in megalithic structures. Bottom: Lion's Gate (Citadel of Mycenae, Greece, around 1250 BC during the Late Bronze Age) is the first example of false vaulting. The catenary: Poleni's drawing of Hooke's analogy beteween an arch and a hanging chain, and his analysis of the Dome of St Peter's in Rome, 1748.

2.2.2 Identification of Mechanical Parameters

Assessing the mechanical properties of masonry can be challenging due to their variability. Additionally, determining the geometric properties of resistance elements can be problematic for rubble or irregular masonry. In contrast to reinforced concrete or steel structures, where the properties of the materials largely describe their phenomenological aspects, the mechanical behavior of masonry structures is heavily influenced by construction techniques.

Effective experimental techniques for in situ measurement are not available for all mechanical parameters. Furthermore, there is an issue of heterogeneity (as illustrated in Figure 4), as structures may have different mechanical properties in different regions. When modeling a masonry construction for structural analysis, the resulting outcome heavily relies on the mechanical parameter values used. This poses a risk of obtaining results that do not represent the real behavior of structures.

Identifying the type of masonry is the first step in determining the appropriate mechanical parameters. This can be a challenging task due to variations in construction methodologies and the presence of local defects, which can cause significant differences even within the same structural element. Identifying the mechanical parameters of masonry, particularly in historical buildings, can be difficult because of the uncertainties associated with the development of sophisticated models that are extremely sensitive to the choice of material properties. Performing destructive testing on historic buildings, either in situ or by removal of samples large enough to be representative, is often impossible due to preservation concerns. Non-destructive testing can provide valuable data without damaging the building, but it may not provide the precise material characterization information required for advanced modeling. Typically, laboratory tests are conducted on masonry samples that accurately represent the building. The response of masonry depends on its geometry, morphology, type of connection between layers, and the physical, chemical, and mechanical properties of its components, such as bricks, stones, and mortar. Masonry is a composite material that can be characterized by

considering these factors.

The first graphs of Fig.5 display two qualitative stress-displacement ($\sigma - \delta$) diagrams, one for uniaxial compression and one for tensile tests on masonry walls. The strength of the wall depends on the strength of its components, namely the blocks and mortar. Experimental evidence indicates that the compressive strength of masonry is significantly greater than its tensile strength. Masonry essentially behaves as a material elastic in compression up to about 80-90 % strength, although due to early formation of microcracks the stress-strain curve from uniaxial tests is definitely nonlinear. After reaching the critical point, the material undergoes permanent deformation and shows a softening branch with a gradual decrease in stresses and an increase in strain in both compression and tension. This behavior is typical of quasi-brittle materials.

Because the experimental tests [80] to determine the mechanical properties can be difficult and expensive, the standard provides tables for obtaining values for both compressive and shear strengths based on the type of masonry (see Table 2).

The Italian building code defines five fundamental mechanical properties of masonry, to be used in resistance criteria, and average specific weight for different types of masonry: average compressive strength (f), average shear strength in the absence of normal stresses (τ_0), average shear strength in the absence of normal stresses (f_{v0}), average value of the normal elasticity modulus (E), average value of the tangential elasticity modulus (G), and average specific weight (w) (see Table 3). The elasticity moduli can be indirectly evaluated by the characteristic compressive strength. Therefore, the essential properties to define are the strengths.

In this context, an interesting contribution is given by Borri defines the seven parameters of MQI (Masonry quality index) method and the relative qualitative judgments [65].

Figure 4: Ruins of Egnazia (Fasano, BR): Roman monuments, VIII century BC.

Table 2: Values of f_k for masonry in solid and partially solid artificial elements (values in N/mm^2), source Italian code D.M. 17/01/2018 (Tab. 11.10.VI).

Characteristic Compressive Strength f_{bk} of element	**Type of Mortar**			
	M15	M10	M5	M2.5
2.0	1.2	1.2	1.2	1.2
3.0	2.2	2.2	2.2	2.0
5.0	3.5	3.4	3.3	3.0
7.5	5.0	4.5	4.1	3.5
10.0	6.2	5.3	4.7	4.1
15.0	8.2	6.7	6.0	5.1
20.0	9.7	8.0	7.0	6.1
30.0	12.0	10.0	8.6	7.2
40.0	14.3	12.0	10.4	-

Table 3: Tipology of masonry, source Italian code D.M. 17/01/2018 (Tab. C8.5.I).

Masonry Type	**f** (N/mm^2)	τ_0 (N/mm^2)	f_{v0} (N/mm^2)	**E** (N/mm^2)	**G** (N/mm^2)	**w** (kN/m^3)
Disordered rubble masonry (pebbles, erratic and irregular stones)	1.0-2.0	0.018-0.032	-	690-1050	230-350	19
Masonry with rough blocks, with uneven thickness	2.0	0.035-0.051	-	1020-1440	340-480	20
Stone masonry with good texture	2.6-3.8	0.056-0.074	-	1500-1980	500-660	21
Irregular masonry of soft stone (tuff, limestone, etc.)	1.4-2.2	0.028-0.042	-	900-1260	300-420	13-16
Regular masonry of soft stone blocks (tuff, limestone, etc.)	2.0-3.2	0.04-0.08	0.10-0.19	1200-1620	400-500	-
Squared stone block masonry	5.8-8.2	0.09-0.12	0.18-0.28	2400-3300	800-1100	22
Solid brick masonry with lime mortar	2.6-4.3	0.05-0.13	0.13-0.27	1200-1800	400-600	18
Semi-solid brick masonry with cement mortar (e.g., double UNI perforation $\leq 40\%$)	5.0-8.0	0.08-0.17	0.20-0.36	3500-5600	875-1400	15

2.2.3 Discontinuous and Unilateral Models

The weakest link in masonry constructions is typically the bond between the unit (block or brick) and mortar. For a thorough analysis of masonry, referred to as micro-modeling, it is necessary to illustrate the units, mortar, and the interface between the units and mortar (Fig.6 shows a simplified micro-modeling strategy, as demonstrate by the work of Lourenço [29]). In this robust type of modeling, the nonlinear response of masonry structures depends on the behavior of the interfaces due to unilateral contact and frictional effects. These effects are influenced by the high compressive strength and low deformability of the blocks in comparison to the low strength and stiffness of joints. The unit-mortar interface experiences two distinct types of failure: tensile failure (mode I) and shear failure (mode II). Typical failure modes of masonry at a two-block masonry assemblage scale are sketched in Fig.7.

The significant difference in behavior between joints and blocks is crucial to determining how masonry structures withstand external forces. Discontinuous behavior in masonry modeling often focuses on joint deformability, where appropriate stiffness represents the actual elastic stiffness of the masonry assembly in compression. The nonlinear response of the joints, also called "interface elements", becomes a pivotal aspect of masonry modeling [62].

Both blocks and mortar exhibit cohesive properties and softening mechanical behavior. This is due to the initiation and propagation of micro-cracks that eventually merge to form larger cracks. As masonry fails, the mortar joints experience incremental degradation primarily induced by tensile forces, resulting in an opening mechanism, and shear forces, involving a friction-sliding mechanism. The one-sided reaction of the mortar joints, driven by the cycles of micro-crack opening and closure, as well as the frictional sliding that occurs when the compressed joint is affected by shear stresses, significantly influence the overall response of the masonry element [57, 67].

The material's inelastic behavior can be described by integrating the $\sigma - \delta$ diagram in both tension and compression. The material properties include tensile fracture energy

(G_t) and compressive fracture energy (G_c). This energy-based approach allows for the description of both tensile and compressive degradation in the same context, as the underlying failure mechanisms are identical, namely continuous crack growth at the micro-level. Masonry can fail through mode II, which is the sliding of the unit-mortar interface under shear loading. Therefore, it is important to incorporate shear failure in a micro-modeling strategy. However, continuum models cannot directly incorporate this failure because they do not discretize the geometries of the unit and mortar. Failure is associated with tension and compression modes in a principal stress space. The following section will illustrate modeling strategies.

As stated in Subsection 2.2.2, the results are influenced by significant variability in both strength and stiffness. Additionally, test results from a single sample cannot be considered reliable for the entire structure due to the intrinsic heterogeneity of masonry. Therefore, the standard numerical contributions alone are insufficient to address this issue. Characterization tests for tensile strength are particularly unreliable, making it difficult to identify a reliable strength value using standard statistical methods. For this reason, the first graphs in Fig.5 should be interpreted as stress-strain ($\sigma - \epsilon$) laws of highly idealized masonry.

The unilateral behavior approximates the material's asymmetrical response to applied loads. Acknowledging and modeling unilateral behavior is important for analyzing and designing masonry constructions. Starting from an initial assessment of structure, it affects decisions about reinforcement, consolidation, and overall structural integrity. Engineers and architects can develop more accurate and effective strategies for preserving and maintaining masonry structures over time by considering the softening aspects of both mortar and blocks.

Starting from the phenomenological characterization of masonry's mechanical behavior, three simplified analytical models can be derived to idealize its complex behavior. In the 1960s, Heyman [4] formulated three hypotheses for historic masonry in a simplified but highly effective manner:

1. Tensile strength is negligible because of its low value;

2. Masonry has infinite compressive strength, and, in fact, it is almost impossible for the masonry to fail by crushing under service loads;

3. There is no possibility of sliding between the blocks.

The Normal-Rigid No-Tension model, introducted by Heyman, describes a material as indefinitely rigid in compression but unable to withstand tensile stresses. The second $\sigma - \epsilon$ plot of Fig.5 shows a comparison between the uniaxial behavior defined by the Normal Rigid No-Tension model and a typical stress-strain diagram for masonry. Although these assumptions provide a basis for an initial assessment of historic monuments, they need to be enriched when dealing with more complex problems, such as seismic events. The stiffness and strength are infinite in compression and zero in tension. This model is suitable for Limit Analysis applications as it does not require any parameters for mechanical characterization of the material.

To refine the Heyman model one defines an ideal uniaxial behavior using a single parameter, Young's modulus E regarding the compressive behavior:

1. Considering finite stiffness while assuming infinite strength, the Normal Elastic No-Tension model a), shown in the third graph of Fig.5;

2. Limiting the strength while assuming infinite stiffness, the Normal Elastic No-Tension model b), shown in the fourth graph of Fig.5.

The Normal Elastic No-Tension model has been thoroughly studied since the late 1970s by distinguished representatives of the Italian School of Structural Engineering [9, 12, 14, 17, 21]. In this elastic model with no-tension assumption, the deformation can be both positive and negative: positive deformation constitutes the fracture deformation, while negative deformation represents the elastic part. The material is globally elastic and is also hyperelastic.

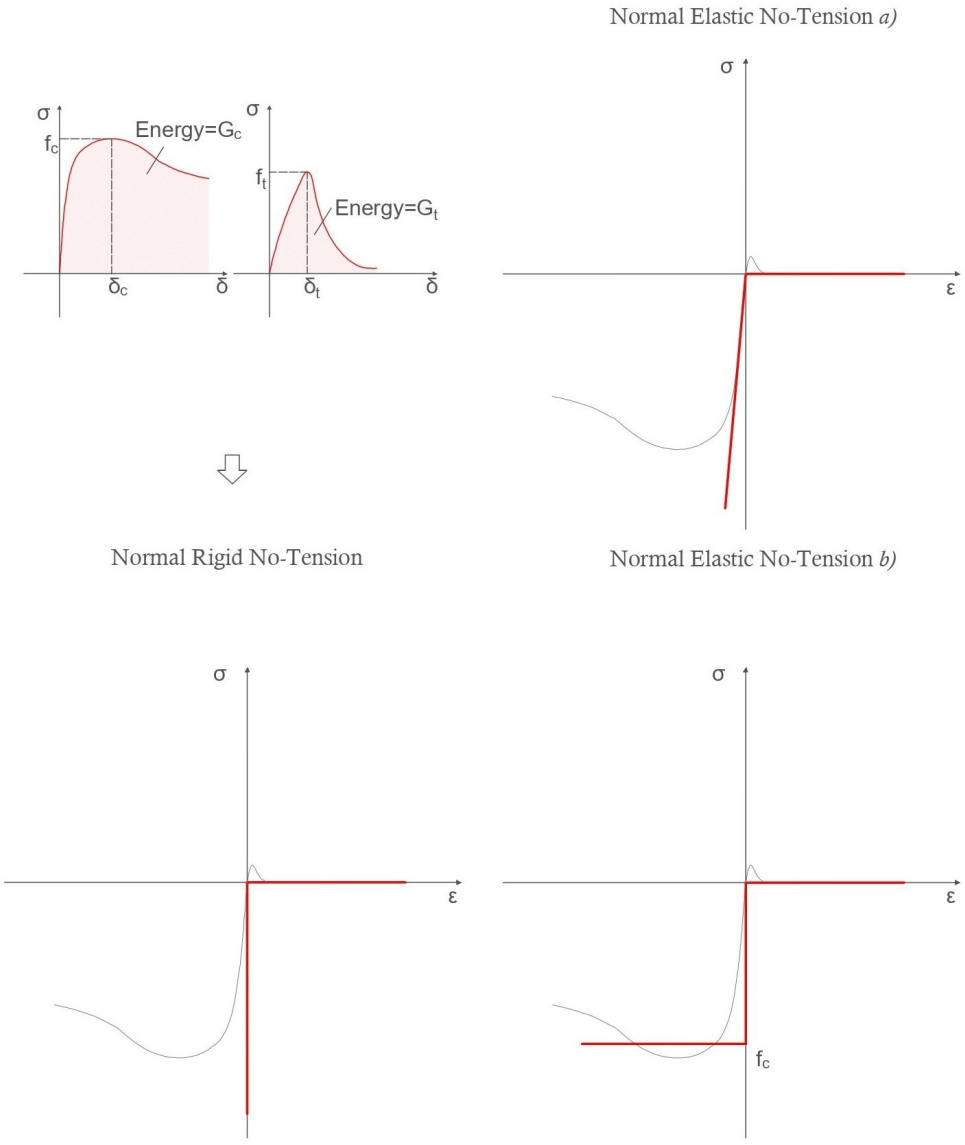

Figure 5: Left: Typical behavior of quasi-brittle materials under uniaxial loading and definition of fracture energy: tensile loading (f_t denotes the tensile strength) and compressive loading (f_c denotes the compressive strength). Uniaxial behaviour (red line) defining Normal Rigid No-Tension. Both stiffness and strength are assumed to be infinite. Since for $\epsilon > 0$ the stress is completely determined by the strain, the behaviour is elastic for any positive deformation, while the stress is non-constitutive for $\epsilon = 0$. Right: Two possible Uniaxial Normal Elastic No-Tension Models obtained by adding one material parameter: in (a) a finite stiffness is fixed while the strength is still assumed to be infinite, in (b) the strength has a finite value and the stiffness remains infinite.

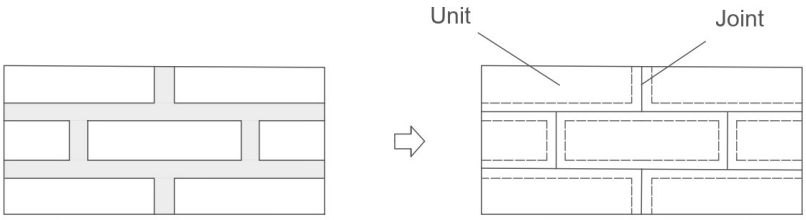

Figure 6: The importance of discontinuities in masonry model [29].

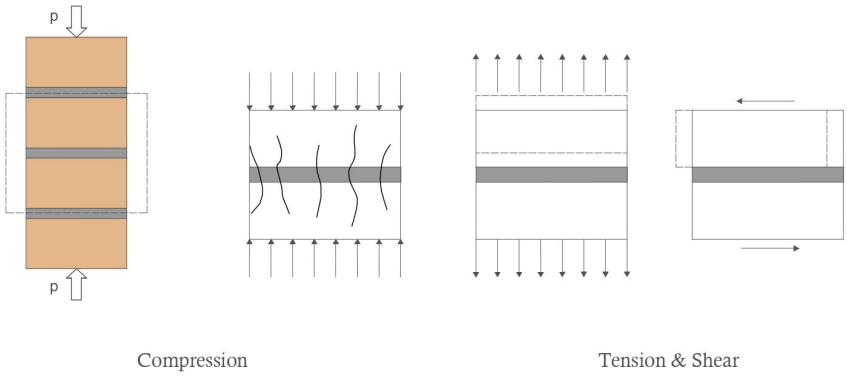

Figure 7: Typical masonry mechanics: Compression (masonry crushing), Tension and Shear (joint tensile cracking and joint slipping) [33].

3 State of Art: Mechanical Models including Nonlinearity

During a seismic event, a masonry building's ductile behavior can vary depending on the damage mechanisms that are activated. Box-like buildings typically sustain widespread damage, which ensures ductile behavior and often allows the construction to withstand significant seismic events. The concept of achieving box-like behavior and significant overall ductility in new building design has long been referenced in national building codes. Therefore, when studying the seismic behavior of masonry structures, it is crucial to globally model the structural system.

Simplified models that analyze individual walls or structural components in isolation can provide useful strength indications. However, they typically do not allow for a straightforward assessment of the ductile behavior of the entire structural system during seismic events. When studying historical buildings, it is crucial to account for the heterogeneous and nonlinear behavior of masonry, particularly its low tensile strength.

Several modeling methods have been formulated in recent decades to estimate the seismic resistance of masonry structures. These methods differ in complexity, basic assumptions, level of detail, and computational requirements. The importance of accurately estimating the seismic resistance of masonry structures cannot be overstated. Traditional modeling methods often failed to consider seismic forces, as they focused primarily on gravitational loads.

The research is based on existing literature on analysis and modeling approaches for masonry. A comprehensive review of the existing modeling strategies structures is presented in [76].

The complexity of the material and the great number of involved nonlinear phenomena result in a vast amount of literature. Especially in historic structures with complex geometries, masonry poses a challenge to structural analysis. There are different approaches, each with its own advantages and disadvantages. It is important to

note that, due to the heterogeneous and nonlinear nature of the material, there is no definitive method that fits all situations.

Approximating the exact geometry is crucial in modeling masonry structures, particularly those with complex geometry. Masonry arches can have non-constant curvature and varying cross sections, and may interact with different materials, including strengthening materials. Different authors use NURBS based approximation field to overcome these difficulties [69, 91].

Structural methods have progressed from early 2D models to more complex 3D models capable of accommodating three-dimensional curved geometries. 3D models allow the study of structures such as vaults and domes, which are common in historic masonry buildings.

This section describes recently proposed and discussed models. It is evident that various analysis approaches typical of structural engineering have been used, indicating that there is no generally accepted preferred solution method. Different classifications can be identified based on the computational burden of the modeling and the type of analysis required. These classifications apply to both analysis and modeling.

Computational strategies for masonry structures are typically classified as micro-modelling or macro-modelling. These approaches are connected through homogenization and upscaling procedures. Macro-modelling describes the mechanical nonlinearity of masonry through a macroscopic continuum, using formulations such as phenomenological plasticity, damage mechanics, and nonlocal damage plasticity.

When analyzing masonry structures, it is crucial to consider the inelastic response over discontinuity surfaces at the brick-mortar bonds. This is because the behavior of masonry is affected by these bonds. Although micro-models with interface elements require more computational resources, they can more accurately capture the complex patterns of discontinuities that characterize the damage evolution in masonry. Interface elements are widely used in the numerical analysis of masonry structures because they can replicate the main features of their response, such as the relative sliding of units.

3.1 Analysis Approaches

Currently, the examination of masonry behavior, especially near or at the point of collapse, can be approached using two distinct methods: incremental-iterative nonlinear analyses and limit analysis-based solutions.

During incremental-iterative analysis, the equilibrium conditions of a structure can be investigated under specific loads. This analyis is done step by step, with loading and structural response divided into intervals or increments. Iterations are then used to achieve equilibrium within each step, addressing mechanical nonlinearity effectively. Accurately assessing the collapse and near-collapse behavior of masonry structures is crucial. Geometrical nonlinearity is also considered due to its potential significant role, particularly in scenarios with substantial rotations and displacements.

These incremental-iterative analyses can be broadly categorized as either nonlinear static or nonlinear dynamic (time history) analyses. In nonlinear static analyses, the structure undergoes incremental loading until it reaches its peak load, extending into the post-peak regime. The pseudo-time that represents the evolution of the structural response lacks specific physical characteristics. Simulations can be conducted in load control, displacement control, or through event-by-event damage control methods. Solving nonlinear differential equations is imperative given the assumed mechanical nonlinearity of the material. These equations are transformed into nonlinear algebraic equations and navigated within a numerical framework. These equations are typically linearized and solved iteratively using methods such as Newton-Raphson iteration and Riks methods [18].

These analyses are commonly used to emulate quasi-static experimental tests on masonry structures [60]. Pushover analysis is a widely adopted and standardized procedure that is instrumental in evaluating the seismic behavior of masonry structures [77]. It subjects the structure to a progressively increasing displacement while maintaining a constant load pattern of horizontal forces.

In nonlinear dynamic analysis, the structure undergoes time-dependent actions and

its response evolves in real-time, accounting for inertial and damping effects. Time integration methods are used to approximate the equations of motion during each time step. These methods are classified as either explicit or implicit, each with its unique characteristics. Explicit methods calculate new response values solely based on quantities obtained in the previous step, while implicit methods incorporate values from the same step into the calculation. This requires assuming and refining trial values through successive iterations.

Nonlinear time history analyses simulate dynamic actions, such as earthquakes, impacts, and explosions, on masonry structures [71]. The ability to factor in time-dependent loads allows for the emulation of the structure's response to real accelerograms, providing a comprehensive understanding of its behavior. Dynamic analysis methods can effectively analyze shaking table experimental tests on masonry structures [55]. Additionally, dynamic analysis may be utilized to simulate quasi-static tests and processes by applying loads in a deliberately slow manner.

Heyman originally applied limit plasticity theorems to analyze masonry structures in relation to limit analysis-based solutions, as introduced in Subsection 2.2.3. These assumptions, coupled with the neglect of elastic strains, facilitated the development of both the static theorem (lower-bound limit analysis [78]) and the kinematic theorem (upper-bound limit analysis [69]) for masonry structures.

The Heyman rigid no-tension model is widely used and has been proven effective in the stability analysis of masonry systems. Initially, these assumptions allowed for straightforward graphic statics solutions to analyze the stability of masonry vaults and kinematic analyses of typical seismic failure modes in masonry buildings. Heyman's hypotheses provided a strong foundation for the development of modern computational methods based on limit analysis.

The problem can be expressed as an optimization problem using various techniques such as genetic algorithms [69], nonlinear differential equations, linear or sequential linear programming [72].

A significant drawback of limit analysis-based solutions is their limited output, focusing solely on the collapse multiplier and the collapse mechanism. They lack information on ultimate displacement and post-peak response, crucial aspects in widely adopted displacement-based seismic assessment procedures for masonry structures.

3.2 Modeling Strategies: Discontinuum vs Continuum

Exploring the collapse behavior of structures is crucial in reducing casualties during seismic events. From a computational perspective, structures undergo both small and large displacements before collapsing. In the realm of small displacements, structural geometry variations under loading can be disregarded. However, the buckling of columns, a predominant cause of structural failure, necessitates the application of large displacement theory for accurate detection.

Traditionally, the Finite Element Method (FEM) [5] serves as the primary tool for investigating structural buckling behavior. Through FEM, one can track the buckling mode, load, and subsequent post-buckling behavior. Although useful, FEM assumes material continuity and requires special methodologies to account for the separation of structural elements. Additionally, it encounters challenges when handling arbitrary and unknown fracture planes before analysis. Models that use joint elements to represent separation are reliable only when the crack location is predictable. This predicament is shared by numerical methods that treat the structure as a continuum.

In this context, Nonlinear-FEM (NFEM) formulations are typically derived through finite deformation and elastic-plastic incremental theory. The finite deformation theory precisely delineates the reference configuration of a deformed body. Several nonlinear finite element formulations have been proposed based on the choice of the reference configuration, including the total Lagrangian formulation (TL), updated Lagrangian formulation (UL), and co-rotational formulation [37, 56].

Within these formulations, the tangent stiffness matrix of the elements or structure is typically composed of two or three separate matrices. For instance, in the TL formu-

lation, the tangent stiffness matrix is the sum of an elastic stiffness matrix, an initial stress stiffness matrix, and an initial displacement stiffness matrix [56]. The recalibration of the element tangent stiffness matrices for nonlinear analysis demands significant numerical integration and computation time.

Following this, Kawai [7] introduced advanced rigid block spring model (RBSM), simplifying the representation of media discontinuities and investigating contact with the presence of both normal and tangential stiffness at the interface. This model adopt static approaches, solving problems through manipulation of stiffness matrices. The method has found success in various domains of structural analysis. It has been effectively utilized in tasks ranging from the study of crack initiation and propagation to seismic response analysis of structures. Ongoing research continues to explore and apply the rigid body-spring discrete element method, captivating the interest of numerous researchers.

Another notable contribution is from Cundall [6], who developed a distinct element method specifically tailored for analyzing densely jointed rocks. The distinct element method emulates jointed rocks through blocks using a dynamic relaxation procedure. Its noteworthy capability lies in simulating substantial displacements and the collapse of these blocks on a large scale.

A subsequent approach addressing structural failure analysis is the Modified or Extended Distinct Element Method (MDEM or EDEM), as introduced by Meguro and Hakuno in [13]. This method adeptly captures highly nonlinear geometric transformations within a structure during the failure process. Another method, Discontinuous Deformation Analysis (DDA) [20], has demonstrated effectiveness in handling large deformations of rock blocks. However, its scope is limited to scenarios where elements are separated from the onset of the analysis, and its validity is not confirmed for cases involving small deformations.

An evolution of the previous methos is the Applied Element Method (AEM) [44], that is based on division of the structural members into virtual elements connected

through springs. Each spring entirely represents the stresses, strains, deformations, and failure of a certain portion of the structure.

All the methods described above involve an explicit representation of discontinuities governed by joint constitutive models. In this context, masonry is modeled block by block, allowing for the incorporation of the actual masonry texture. The behavior of the blocks can be considered either rigid or deformable, while their interaction can be mechanically represented through various suitable formulations. Several models fall into this prominent category; for example, the following works specifically for masonry are reported: FEM models with joint elements [8, 33], DEM models characterized by rigid or deformable blocks [54], models emerging from the combination of DEM and FEM [50], RBSM models [71].

Conversely, the masonry material is depicted as a continuously deformable body, eliminating the distinction between individual blocks and mortar layers. The material's constitutive law can be defined through either direct approaches, such as constitutive laws calibrated based on experimental tests, or homogenization procedures and multi-scale approaches. The constitutive law of the material, considered homogeneous in the structural-scale model, is derived from a homogenization process linking the structural-scale model to a material-scale model. The material-scale model represents the primary masonry heterogeneities within a representative volume element (RVE) of the structure. In such cases, the resolution of structural-scale problems could be formulated within a multi-scale framework.

In general, discontinuous methods differ from continuum formulations because they implement discrete bodies with contacts or interfaces between them. They allow for modeling displacement discontinuities, block deformability, and large displacements and rotations.

In this dissertation, starting from this subsection, the micro-models are deepened because, using this type of approach, it is possible to consider the interface elements, even with zero thickness for dry joints, as potential crack, slip, or crush regions. The

bond between the unit and mortar is often the weakest link in masonry assemblages, and the nonlinear response of the joints, which is primarily controlled by the unit-mortar interface, stands out as one of the most crucial aspects of masonry behavior. The advantage of this modeling strategy is that it allows for the study of all conceivable failure mechanisms.

3.3 Rigid Block Models

Rigid block models have versatile applications in engineering disciplines, streamlining the analysis of intricate structures.

In structural dynamics, oscillatory motion of tall and slender structures, such as towers, skyscrapers, and support structures, is commonly studied. Rigid block models are essential in multibody systems, particularly in automotive simulations, aiding dynamic analyses for vehicles and mechanical components in mechanical engineering. Their ability to model complex interactions between rigid parts makes them valuable tools for optimizing performance and designing stable, safe systems. In structural engineering, rigid block models are used to analyze the statics and dynamics of masonry, providing insights into the behavior of walls and complex architectures. Their ability to model large displacements is crucial for understanding how structures respond to dynamic forces.

These models are fundamental tools for structural and dynamic analyses, providing a robust foundation for comprehending the behavior of complex systems across diverse engineering contexts.

In the realm of dynamics, the study of rocking rigid blocks spans over six decades, consistently revealing new and intricate phenomena within this seemingly straightforward system [59]. This model has widespread applications in different structures, including tall buildings, free-standing power transformers, cell towers, silos, and containers. The rocking block represents slender structures that are poorly connected or entirely disconnected from the ground. Lateral movements of the foundation can cause

rocking motion, which may lead to overturning or structural damage under specific sets of excitation parameters.

There are typically two primary types of excitations to consider. The first involves earthquakes that impact structures on the ground. Earthquakes are characterized by a relatively high and broad-frequency spectrum, albeit of short duration. Consequently, structures are often subjected to rapid and intense forcing, which can result in damage or overturning. In contrast, the second type of excitation involves sea waves acting on container ships. During extreme events, the excitation of sea waves can have properties similar to or worse than those of earthquakes. In such cases, it is important to study the situation by assuming the forcing as a complex signal [82]. Sea waves have lower frequencies, endure for extended periods, and change gradually. Therefore, stable oscillatory motion can be observed in addition to the potential for damage or overturning.

During the Chilean earthquakes of May 1960, certain tall and slender structures demonstrated unexpected resilience to ground shaking, while seemingly more stable structures suffered severe damage. In 1963, Housner presented groundbreaking analysis in [3], focusing on the rocking motion of inverted pendulum-type structures. The analysis showed that tall and slender structures are more stable against overturning during earthquakes than conventional expectations had predicted, which explains their survival. Housner's study analyzed the rocking motion of rigid blocks placed on a rigid, horizontal base and subjected to external excitation. The results showed distinct vibrational characteristics compared to linearly elastic structures. Housner pioneered the derivation of analytical expressions for the minimum base acceleration required to initiate overturning of the rigid block from a state of rest, considering various types of horizontal ground motions.

Rigid block models have computational advantages over other discontinuous modeling approaches, such as the distinct/discrete element method. This is mainly due to the formulation and solution of the variational framework that governs the response at

the contact interfaces between blocks. When dealing with frictional interfaces without tension, inequalities and complementarity conditions can succinctly express the unilateral behavior of contact joints, which is common in historic masonry structures where tensile and cohesive strength may be uncertain and negligible. Assuming associative behavior for displacement rates at contact interfaces allows for the decoupling of governing equations into dual optimization problems, aligning with classic limit analysis approaches. This typically corresponds to force-based and displacement-based optimization problems. Solving optimization problems, such as the force-based problem, and obtaining the solution of the dual problem from associated Lagrange multipliers streamlines the process, providing both static and kinematic variables in a single run. This approach is particularly efficient in terms of implementation in structural analysis software due to its efficient solution procedures for mathematical programming [81].

Currently, most rigid block models in literature rely on classical limit analysis formulations, enabling estimation of the structure's force capacity [42]. However, these models have a limitation: they compute the load multiplier based on the initial structural configuration, linked to the activation of the failure mechanism but not its evolution. As a result, they are not suitable for displacement-based methods outlined in the current Italian building code.

Recently, rigid block models incorporating sequential limit analysis and incremental solution techniques have emerged to account for large displacements [81]. Nevertheless, these models have primarily been applied to analyze settlement-induced failure mechanisms. Moreover, they typically do not encompass elastic response and are primarily utilized for the nonlinear kinematic analysis of mechanisms, particularly for evaluating post-peak rocking behavior [68]. Different authors work to overcome these limitations using models for the pushover analysis that comprise both the elastic and the rigid body behaviors required by the standard [70, 85].

To simplify common computational processes, discrete models that use infinitely rigid elements can provide a more straightforward approach to modeling, especially

when examining ancient masonry characterized by robust blocks and fragile mortar or dry joints.

It is important to note that masonry samples often have a regular arrangement of robust elements with distinct square or rectangular shapes. In addition, the displacements caused by different loads are usually smaller than those found in soil and rock systems. The contact topology remains consistent throughout the analysis due to the limited displacements in relation to the overall specimen dimensions. Therefore, a simplified model without contact detection algorithms helps to reduce computational demands in the analysis.

Cecchi and Sab presented a simple and effective discrete model that uses rigid elements and elastic interfaces to simulate both in-plane and out-of-plane loaded regular masonry [49]. This model was later extended to accommodate random masonry configurations, and recently, it has been expanded for the in-plane modal analysis of regular masonry through the incorporation of a matrix solution approach.

Specifically, the rigid Discrete Element Method (DEM) has been recently applied to nonlinear analyses of in-plane loaded masonry panels by adopting a Mohr-Coulomb yield criterion to govern joint actions. A similar model employing these assumptions in both linear and nonlinear domains was investigated by Trovalusci and Masiani [48].

Additionally, it's noteworthy that the assumptions of rigid blocks and dry joints adhering to a Mohr-Coulomb yield criterion are frequently employed in the realm of limit analysis for masonry [26, 34, 41].

3.4 Interface Models

This dissertation is based on the Cohesive Zone Model (CZM) introduced by Dugdale [1] and Barenblatt [2]. Originally designed to analyze the area before a crack tip, this model has become a versatile tool with various applications, all linked by the fundamental concept of a mechanical interface.

CZMs have become essential components in computational frameworks, especially

in the nonlinear finite/discrete element method. CZMs are widely used due to their adaptability in addressing various fracture events and their ease of numerical implementation. This facilitates the integration of interface elements into both research and commercial codes.

In this context, several interface model formulations have been presented in literature; in particular, some of them have been developed to reproduce the failure mechanisms in quasibrittle materials (like clay brick, mortar, ceramics, rock or concrete), that typically involve the initiation, growth, and merging of microcracks [15]. These microcracks lead to localized strain within a narrow region, forming a cohesive, and possibly frictional, internal surface. As the cohesive forces diminish, a stress-free discontinuity or fracture surface emerges. In classical fracture mechanics problems, determining the geometric shape and location of the fracture is inherently part of the nonlinear problem. Nevertheless, there are situations where the potential decohesion surface can be predefined.

In such cases, introducing mechanical interfaces within the continuum becomes highly advantageous, aiming to guide the potential development of fractures.

In the context of finite geometry changes in CZMs, the pivotal exploration commenced with Needleman's investigation [16]. This study delved into the progressive decohesion of an elastic block from a rigid substrate, employing a cohesive interface.

A seminal contribution to this field was made by Ortiz and Pandolfi [37], who introduced the concept of an extended crack-tip or cohesive zone by combining finite elements and interface elements. The authors emphasized the significance of representing the traction-opening displacement cohesive law through tools linked to irreversible constitutive laws. Furthermore, they introduced the novel concept of mean deformation mapping, which simplifies the definition of a unique deformed configuration.

Specifically, a reference middle surface of the cohesive element in the current configuration is utilized to define a convenient (deformed) surface for calculating the normal and tangential directions to the interface. The use of this separation surface allows

the evaluation of a tangent stiffness matrix that exhibits asymmetry attributed to a geometric term.

Another notable advancement, presented in [36], involved the development of an interface for large displacements. Here, thin beam layers separated by interfaces were employed to model delamination coupled with geometric instabilities arising from the buckling of thin laminates. In this formulation as well, the recovered stiffness matrix displayed asymmetry.

Qiu et al. [40] proposed a large displacement formulation within the co-rotational reference system coincident with one of the two deformed sides of the interface and developed a 2D linear four-node element. While the formulation proved intricate, extending it to higher-order elements appeared less straightforward.

Addressing delamination in finite displacement problems, Wells et al. [46] incorporated a discontinuity displacement field within finite elements. This concept marked the first linearization of geometric effects on the interface, resulting in an unsymmetric stiffness matrix.

Reinoso and Paggi [64] contributed to the field with a consistent derivation of an interface element for large displacement analysis, implementing a clear 2D four-node cohesive element. Their deliberate omission of certain terms in the stiffness matrix formulation during linearization led to an unsymmetric tangent stiffness.

In the work by Borino and Parrinello [86], a 2D cohesive interface formulation was developed under finite displacement conditions. This approach naturally yielded a symmetric tangent stiffness matrix, provided all involved terms, including second-order partial derivatives, were retained in the development without neglecting any aspects of the exact linearization procedure.

Interface models have found broad application in the numerical analysis of masonry structures due to their ability to capture the complex patterns of discontinuities that characterize the damage evolution in masonry with a higher degree of accuracy.

In particular, micro-models can reproduce the main features of interface elements

response, such as the relative sliding of units [58, 75].

Interface elements are specifically designed to model the behavior of masonry mortar joints. Lofti and Shing [27] proposed a dilatant interface constitutive model to simulate the initiation and propagation of interface fracture under combined normal and shear stress in both tension-shear and compression-shear regions.

Gambarotta and Lagomarsino [31] proposed a constitutive equation for the interface model that includes two internal variables representing frictional sliding and damage caused by cyclic loading in the mortar joint.

Giambanco and Di Gati [32] developed a cohesive interface model that uses a yield surface expressed by the classical bilinear Coulomb condition with a tension cut-off and a non-associated flow law.

Lourenço and Rots [33] developed a constitutive interface model based on an incremental formulation of plasticity theory. This model is capable of simulating the cyclic behavior of the cohesive zone by reproducing the nonlinear response during unloading.

Alfano and Sacco [51, 52] proposed a new cohesive-zone model that combines interface damage and friction based on micromechanical formulation. The model was shown to effectively predict failure mechanisms and overall response of masonry structures. Specifically, they reproduced the experimental behavior of a masonry wall subjected to compression and shear loads in the context of seismic analysis of masonry buildings.

Sacco and Toti [58] proposed a modified formulation of the interface model initially developed in [51, 52]. The interface model developed was able to simulate the progressive damage and failure of the mortar layers, as well as the possible initiation and propagation of fractures within the bricks.

4 2D-Rigid Block Model with Interfaces

This dissertation presents a 2D rigid block model with interfaces for structural analysis, specifically for nonlinear problems. Nonlinear structural problems can be classified into three primary types: material nonlinearity, geometrical nonlinearity, and contact nonlinearity.

This section discusses the formulation of a rigid block model with geometrical nonlinearity. In applications involving masonry structures that experience significant displacements, the complexity is related to the inability to approximate the deformed configuration by the underformed one during simulation due to the occurrence of large displacements. To address this challenge, a co-rotational reference system is introduced. This system is aligned with the middle-line between the two deformed sides of the interface shared by two rigid blocks. In Lagrangian formulations, the co-rotational case is considered a variant of the Total Lagrangian formulation [18].

Large displacements are investigated by implementing both finite rotations and moderate rotations. The distinction between these rotations lies in the magnitude of the angular displacements, with finite rotations representing larger angular displacements and moderate rotations referring to smaller angular displacements. Treating both types of rotations allows for a more comprehensive analysis of the structural behavior under large displacements [11, 25, 84].

At the end of the section, the model is also implemented under the simplified scenario of small displacements, allowing the application of the first-order theory, formulating equilibrium equations in the undeformed configuration.

4.1 Large Displacements

The evolution of mechanisms in masonry structures involves finite rotations and therefore large displacements. Within the framework of the rigid block model, this scenario represents the most comprehensive case of geometrical nonlinearity and is the main

focus of the current section.

In particular, the governing equations of the proposed model are elucidated, starting with the kinematics of a single rigid block. Subsequently, the kinematics of the interface is presented as the analysis is extended to the scenario of two rigid blocks sharing an interface. This progression leads to the formulation of the equilibrium equations within the discrete framework of the problem. Finally, the material and geometrical contributions to the element stiffness matrix are uniquely determined.

4.1.1 Rigid Block Kinematics

The in-plane kinematics of each j-th element is governed by three degrees of freedom associated with the rigid body motion. The Lagrangian parameters are the translational displacements $U^{(j)}$,$V^{(j)}$ and the rotation $\Phi^{(j)}$ of the center of mass of the j-th block $G^{(j)}$, as shown for a single block in Fig.8.

Let $x_G^{(j)}$, $y_G^{(j)}$ denote the coordinates of the centroid of the j-th block, and let $U^{(j)}$ and $V^{(j)}$ be collected in the vector $\mathbf{U}_G^{(j)}$. The displacement components $u^{(j)}$, $v^{(j)}$ at the typical point (x, y) of the j-th rigid block can be obtained by these parameters, in two dimensions, as:

$$\mathbf{u}^{(j)} = \mathbf{U}_G^{(j)} + (\mathbf{R}^{(j)} - \mathbf{I})(\mathbf{x} - \mathbf{x}_G^{(j)}) \tag{4.1}$$

where $\mathbf{u}^{(j)} = [u^{(j)}, v^{(j)}]^T$, $\mathbf{U}_G^{(j)} = [U^{(j)}, V^{(j)}]^T$, $\mathbf{x} = [x, y]^T$, and $\mathbf{x}_G^{(j)} = [x_G^{(j)}, y_G^{(j)}]^T$.

The rotation matrix $\mathbf{R}^{(j)}$ is obtained by the Euler-Rodrigues formula, which expresses finite rotations as follows:

$$\mathbf{R}^{(j)} = \mathbf{I} + \sin\Phi^{(j)}\mathbf{W} + (1 - \cos\Phi^{(j)})\mathbf{W}^2$$

with

$$\mathbf{I} = \begin{bmatrix} 1 & 0 \\ 0 & 1 \end{bmatrix} \quad \mathbf{W} = \begin{bmatrix} 0 & -1 \\ 1 & 0 \end{bmatrix}$$

where $\mathbf{I}$ is the identity matrix and $\mathbf{W}$ is a skew-symmetric tensor, such that:

$$\mathbf{R}^{(j)} = \begin{bmatrix} \cos\Phi^{(j)} & -\sin\Phi^{(j)} \\ \sin\Phi^{(j)} & \cos\Phi^{(j)} \end{bmatrix} \tag{4.2}$$

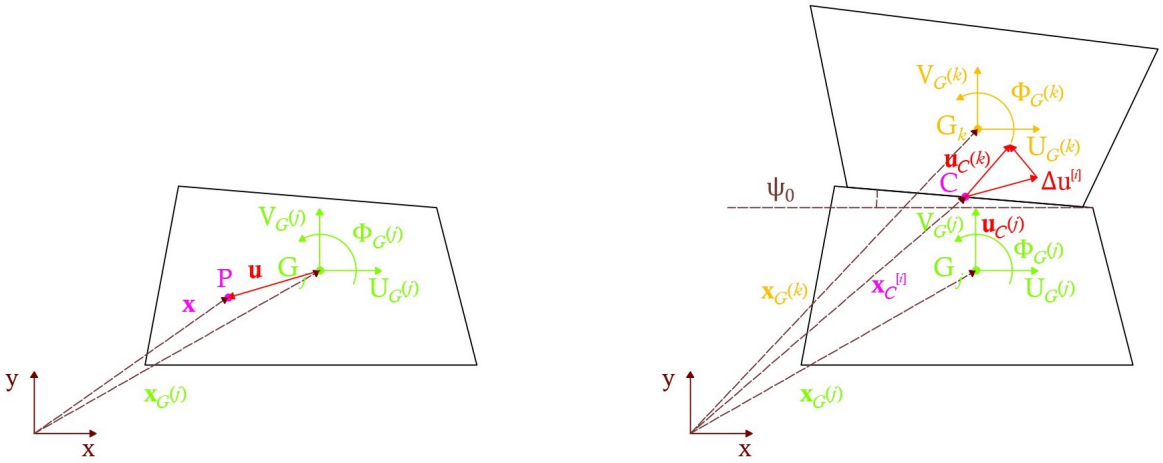

Figure 8: Kinematic definition of rigid blocks: the case of a single block and the other one of two rigid blocks sharing a common interface.

4.1.2 Interface Kinematics

Let us consider two adjacent elements j and k sharing the i-th interface with zero thickness, where the k-th rigid block is located at the top of the interface while the j-th rigid block is located at its bottom, as shown in Fig.8.

The relative displacement at the interface at the midpoint $\mathbf{x}_C^{[i]} = [x_C^{[i]}, y_C^{[i]}]^T$, considering Eq.(4.1), can be expressed as:

$$\mathbf{\Delta u}^{[i]} = \mathbf{u}_C^{(k)} - \mathbf{u}_C^{(j)} \tag{4.3}$$

where it is:

$$\mathbf{u}_C^{(j)} = \mathbf{U}_G^{(j)} + (\mathbf{R}^{(j)} - \mathbf{I})(\mathbf{x}_C^{[i]} - \mathbf{x}_G^{(j)})$$

$$\mathbf{u}_C^{(k)} = \mathbf{U}_G^{(k)} + (\mathbf{R}^{(k)} - \mathbf{I})(\mathbf{x}_C^{[i]} - \mathbf{x}_G^{(k)})$$

and the relative rotation between two blocks as:

$$\psi^{[i]} = \Phi^{(k)} - \Phi^{(j)} \tag{4.4}$$

Then let us collect the components of the relative displacements and rotation in the vector of the kinematic interface parameters, denoted as $\mathbf{s}^{[i]} = [\Delta u_x^{[i]}, \Delta u_y^{[i]}, \psi^{[i]}]^T$, in the following manner:

$$\mathbf{s}^{[i]} = \left\{ \begin{array}{c} \Delta u_x^{[i]} \\ \Delta u_y^{[i]} \\ \psi^{[i]} \end{array} \right\} = \left\{ \begin{array}{c} U^{(k)} + (\cos\Phi^{(k)} - 1)(x_C^{[i]} - {x_G}^{(k)}) - \sin\Phi^{(k)}(y_C^{[i]} - {y_G}^{(k)}) + ... \\ -[U^{(j)} + (\cos\Phi^{(j)} - 1)(x_C^{[i]} - {x_G}^{(j)}) - \sin\Phi^{(j)}(y_C^{[i]} - {y_G}^{(j)})] \\ V^{(k)} + (\cos\Phi^{(k)} - 1)(y_C^{[i]} - {y_G}^{(k)}) + \sin\Phi^{(k)}(x_C^{[i]} - {x_G}^{(k)}) + ... \\ -[V^{(j)} + (\cos\Phi^{(j)} - 1)(y_C^{[i]} - {y_G}^{(j)}) + \sin\Phi^{(j)}(x_C^{[i]} - {x_G}^{(j)})] \\ \Phi^{(k)} - \Phi^{(j)} \end{array} \right\}$$

A co-rotational reference system is introduced, aligned with the middle-line between

the two deformed sides of the interface shared by two rigid blocks (blue line in Fig.9). In 2D, the tangential and normal vectors $\mathbf{t}$ and $\mathbf{n}$ to the middle-line of the i-th interface are used to define the local frame:

$$\mathbf{t} = \left\{ \begin{array}{c} \cos\theta^{[i]} \\ \sin\theta^{[i]} \end{array} \right\} \quad \mathbf{n} = \left\{ \begin{array}{c} -\sin\theta^{[i]} \\ \cos\theta^{[i]} \end{array} \right\} \tag{4.5}$$

where the actual interface angle, $\theta^{[i]}$, is defined taking into account the average of the rotations of the two rigid blocks, $\Phi^{(j)}$ and $\Phi^{(k)}$, as follows:

$$\theta^{[i]} = \psi_0 + \frac{1}{2}\left(\Phi^{(j)} + \Phi^{(k)}\right) \tag{4.6}$$

where ψ_0 is the initial angle of the interface, positive counterclockwise (i.e. in the figure 8 this angle is negative).

The relative displacement in this local system $\hat{\mathbf{s}}^{[i]} = [\Delta\hat{u}_t^{[i]}, \Delta\hat{u}_n^{[i]}, \psi^{[i]}]^T$ can be expressed as:

$$\hat{\mathbf{s}}^{[i]} = \hat{\mathbf{R}}^{[i]}\mathbf{s}^{[i]} \tag{4.7}$$

where the local rotation matrix $\hat{\mathbf{R}}^{[i]}$ is given by:

$$\hat{\mathbf{R}}^{[i]} = \begin{bmatrix} \cos\theta^{[i]} & \sin\theta^{[i]} & 0 \\ -\sin\theta^{[i]} & \cos\theta^{[i]} & 0 \\ 0 & 0 & 1 \end{bmatrix} \tag{4.8}$$

It is worth noting that for large displacements the operator $\hat{\mathbf{R}}^{[i]}$ is a function of the displacement field.

In a co-rotational model, the displacement of the typical point along the interface is denoted as $\boldsymbol{\Delta}\tilde{\mathbf{u}}^{[i]} = [\Delta\tilde{u}_t^{[i]}, \Delta\tilde{u}_n^{[i]}]^T$, i.e. in the local frame, all points along the middle-line undergo a translation along $\mathbf{t}$, $\Delta\hat{u}_t^{[i]}$, and a translation along $\mathbf{n}$, $\Delta\hat{u}_n^{[i]}$. It follows that the relative displacement along the interface in the current configuration is equal to:

$$\boldsymbol{\Delta}\tilde{\mathbf{u}}^{[i]} = \boldsymbol{\Delta}\hat{\mathbf{u}}^{[i]} + (\mathbf{R}^{(k)} - \mathbf{I})(\hat{\mathbf{x}} - \hat{\mathbf{x}}_C) - \left(\mathbf{R}^{(j)} - \mathbf{I}\right)(\hat{\mathbf{x}} - \hat{\mathbf{x}}_C) \tag{4.9}$$

where $\boldsymbol{\Delta}\hat{\mathbf{u}}^{[i]} = [\Delta\hat{u}_t^{[i]}, \Delta\hat{u}_n^{[i]}]^T$, $\hat{\mathbf{x}}$ is the position vector of a typical interface point, and $\hat{\mathbf{x}}_C$ is the position vector of the interface center point.

The rotation matrices have the following form:

$$\mathbf{R}^{(k)} = \begin{bmatrix} \cos\dfrac{\psi^{[i]}}{2} & -\sin\dfrac{\psi^{[i]}}{2} \\ \sin\dfrac{\psi^{[i]}}{2} & \cos\dfrac{\psi^{[i]}}{2} \end{bmatrix}$$

$$\mathbf{R}^{(j)} = \begin{bmatrix} \cos -\left(\dfrac{\psi^{[i]}}{2}\right) & -\sin\left(-\dfrac{\psi^{[i]}}{2}\right) \\ \sin\left(-\dfrac{\psi^{[i]}}{2}\right) & \cos\left(-\dfrac{\psi^{[i]}}{2}\right) \end{bmatrix}$$

By introducing a local abscissa along the current interface, centered on the middle-line, and considering L as the length of the interface with $-\dfrac{L}{2} \leq \xi \leq \dfrac{L}{2}$, the Eq.(4.9) allows for the following expression:

$$\boldsymbol{\Delta}\hat{\mathbf{u}}^{[i]} = \begin{Bmatrix} \Delta\hat{u}_t^{[i]} \\ \Delta\hat{u}_n^{[i]} + 2\xi\sin\dfrac{\psi^{[i]}}{2} \end{Bmatrix} \tag{4.10}$$

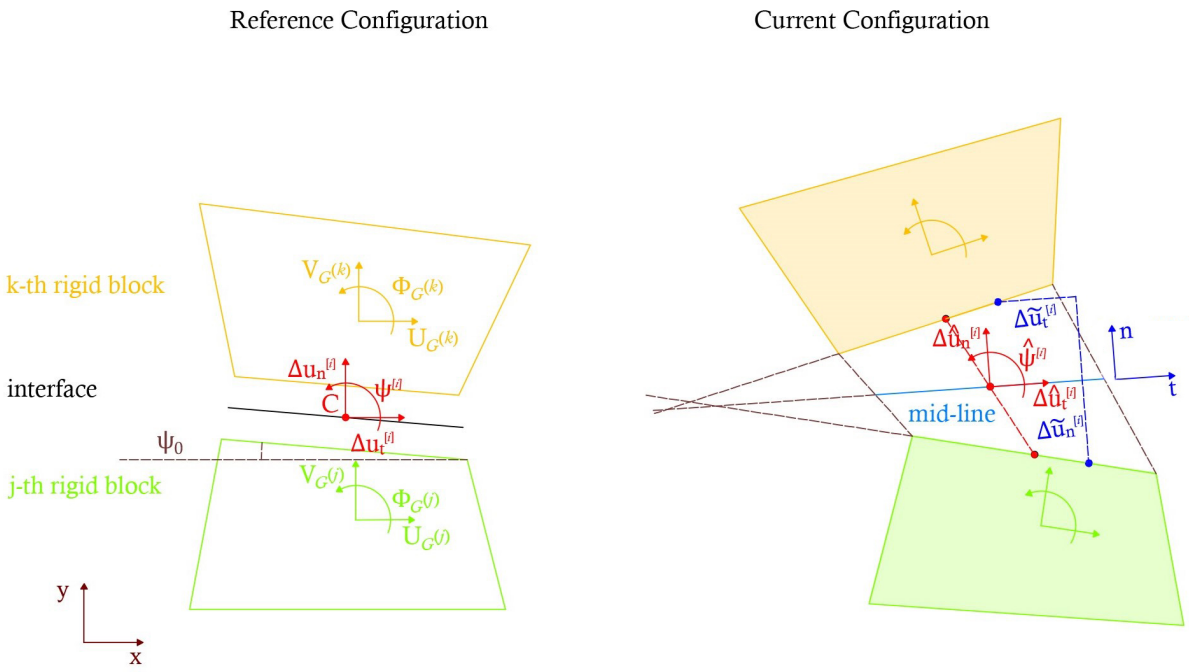

Figure 9: Kinematic definition of the interface along the nonlinear displacement process.

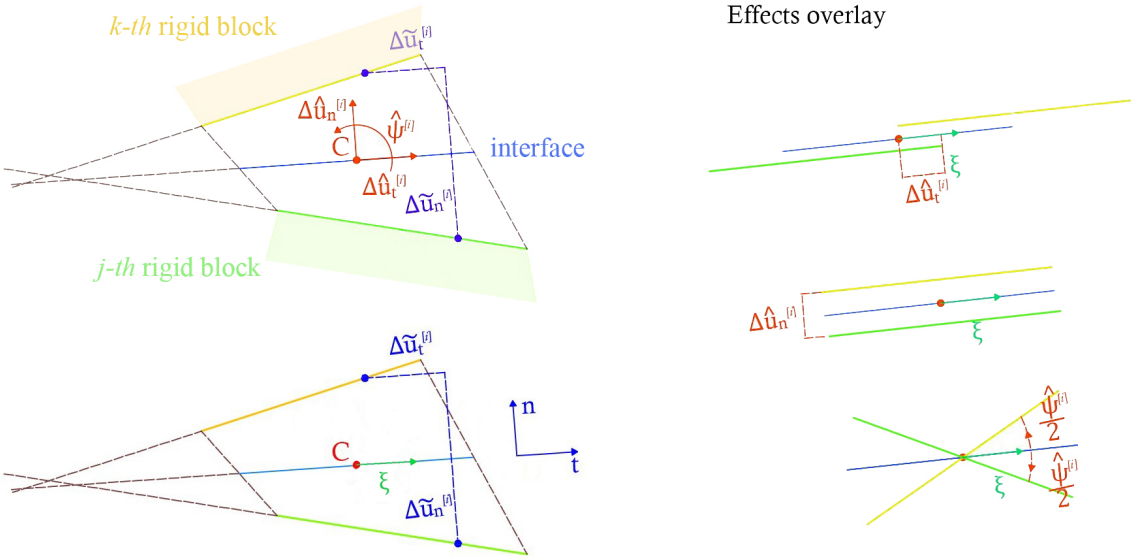

Figure 10: Interface kinematics definition in a co-rotational model along the middle-line.

4.1.3 Equilibrium Equations

A consistent formulation of the interface model must take into account the nonlinear dependence on the displacement field of both the equations of rigid body motion, considering finite rotations, and the rotation of the interface in the subsequent linearization of the discrete version of the Principle of Virtual Work.

First, let us collect all the Lagrangian parameters of two rigid blocks in the following vector $\mathbf{d} = [U^{(j)}, V^{(j)}, \Phi^{(j)}, U^{(k)}, V^{(k)}, \Phi^{(k)}]^T$, and the interface stress components in the following vector $\hat{\mathbf{S}}^{[i]} = [T^{[i]}, N^{[i]}, M^{[i]}]^T$. Focusing our attention on the analysis of the interface between the blocks, the contribution of the local stress at the interface, acting on the actual interface, to the Principle of Virtual Work, can be expressed as the internal virtual work:

$$L_{vi} = \left(\frac{\partial \hat{\mathbf{s}}^{[i]}}{\partial \mathbf{d}} \delta \mathbf{d} \right)^T \hat{\mathbf{S}}^{[i]} \tag{4.11}$$

where $\delta \hat{\mathbf{s}}^{[i]} = \dfrac{\partial \hat{\mathbf{s}}^{[i]}}{\partial \mathbf{d}} \delta \mathbf{d}$ is the virtual relative displacement. By replacing Eq.(4.7) in Eq.(4.11), the internal work becomes:

$$L_{vi} = \left(\frac{\partial (\hat{\mathbf{R}}^{[i]} \mathbf{s}^{[i]})}{\partial \mathbf{d}} \delta \mathbf{d} \right)^T \hat{\mathbf{S}}^{[i]} \tag{4.12}$$

where

$$\frac{\partial (\hat{\mathbf{R}}^{[i]} \mathbf{s}^{[i]})}{\partial \mathbf{d}} \delta \mathbf{d} = \left(\frac{\partial \hat{\mathbf{R}}^{[i]}}{\partial \mathbf{d}} \mathbf{s}^{[i]} + \hat{\mathbf{R}}^{[i]} \frac{\partial \mathbf{s}^{[i]}}{\partial \mathbf{d}} \right) \delta \mathbf{d} \tag{4.13}$$

For clarity, let us rewrite the partial derivative of the relative interface displacement vector $\hat{\mathbf{s}}^{[i]}$ with respect to the Lagrangian parameters vector $\mathbf{d}$:

$$\frac{\partial \hat{\mathbf{s}}^{[i]}}{\partial \mathbf{d}} = \frac{\partial \hat{\mathbf{R}}^{[i]}}{\partial \mathbf{d}} \mathbf{s}^{[i]} + \hat{\mathbf{R}}^{[i]} \frac{\partial \mathbf{s}^{[i]}}{\partial \mathbf{d}} \tag{4.14}$$

and in components:

$$\frac{\partial \hat{s}_i^{[i]}}{\partial d_k} = \frac{\partial \hat{R}_{ij}^{[i]}}{\partial d_k} s_j{}^{[i]} + \hat{R}_{ij}^{[i]} \frac{\partial s_j{}^{[i]}}{\partial d_k} \tag{4.15}$$

Here the index notation uses the subscripts i, j, and k.

The two partial derivatives of the rotation matrix $\hat{\mathbf{R}}^{[i]}$ and the relative displacement in the global frame $\mathbf{s}$ with respect to the Lagrangian parameters vector $\mathbf{d}$ are denoted as $\hat{\mathbf{W}}$ and $\tilde{\mathbf{W}}$, respectively, and can be expressed in the following equation:

$$\frac{\partial \hat{\mathbf{s}}^{[i]}}{\partial \mathbf{d}} = \hat{\mathbf{W}} \mathbf{s}^{[i]} + \hat{\mathbf{R}}^{[i]} \tilde{\mathbf{W}} \tag{4.16}$$

and in components:

$$\frac{\partial \hat{s}_i^{[i]}}{\partial d_k} = \hat{W}_{ijk} s_j{}^{[i]} + \hat{R}_{ij}^{[i]} \tilde{W}_{jk} \tag{4.17}$$

Then, for simplicity, let us define the matrices $\hat{\mathbf{B}} := \hat{\mathbf{W}} \mathbf{s}^{[i]}$ and $\tilde{\mathbf{B}} := \hat{\mathbf{R}}^{[i]} \tilde{\mathbf{W}}$ in the

following equation:

$$\frac{\partial \hat{\mathbf{s}}^{[i]}}{\partial \mathbf{d}} = \hat{\mathbf{B}} + \tilde{\mathbf{B}} \tag{4.18}$$

and in components:

$$\frac{\partial \hat{s}_i^{[i]}}{\partial d_k} = \hat{B}_{ik} + \tilde{B}_{ik} \tag{4.19}$$

By substituting the Eq.(4.13) into the Eq.(4.12), and considering the matrices defined in the Eq.(4.18), the internal virtual work can be expressed as follows:

$$L_{vi} = \delta \mathbf{d}^T \left(\hat{\mathbf{B}} + \tilde{\mathbf{B}} \right)^T \hat{\mathbf{S}}^{[i]} \tag{4.20}$$

In particular:

$$\hat{\mathbf{B}} = \begin{bmatrix} 0 & 0 & \alpha_1 & 0 & 0 & \alpha_1 \\ 0 & 0 & \alpha_2 & 0 & 0 & \alpha_2 \\ 0 & 0 & 0 & 0 & 0 & 0 \end{bmatrix} \tag{4.21}$$

where

$$\alpha_1 = \frac{\sin\theta^{[i]}\,\alpha_4}{2} - \frac{\cos\theta^{[i]}\,\alpha_3}{2}$$

$$\alpha_2 = \frac{\cos\theta^{[i]}\,\alpha_4}{2} + \frac{\sin\theta^{[i]}\,\alpha_3}{2}$$

with

$$\begin{aligned}\alpha_3 &= V^{(j)} + (\cos\Phi^{(j)} - 1)(y_C^{[i]} - {y_G}^{(j)}) + \sin\Phi^{(j)}(x_C^{[i]} - {x_G}^{(j)}) + ... \\ &-[V^{(k)} + (\cos\Phi^{(k)} - 1)(y_C^{[i]} - {y_G}^{(k)}) + \sin\Phi^{(k)}(x_C^{[i]} - {x_G}^{(k)})]\end{aligned} \tag{4.22}$$

$$\begin{aligned}\alpha_4 &= U^{(j)} + (\cos\Phi^{(j)} - 1)(x_C^{[i]} - {x_G}^{(j)}) - \sin\Phi^{(j)}(y_C^{[i]} - {y_G}^{(j)}) + ... \\ &-[U^{(k)} + (\cos\Phi^{(k)} - 1)(x_C^{[i]} - {x_G}^{(k)}) - \sin\Phi^{(k)}(y_C^{[i]} - {y_G}^{(k)})]\end{aligned}$$

and

$$\tilde{\mathbf{B}} = \begin{bmatrix} -\beta_2 & -\beta_1 & \beta_2\,\beta_6 - \beta_1\,\beta_5 & \beta_2 & \beta_1 & \beta_1\,\beta_3 - \beta_2\,\beta_4 \\ \beta_1 & -\beta_2 & -\beta_2\,\beta_5 - \beta_1\,\beta_6 & -\beta_1 & \beta_2 & \beta_2\,\beta_3 + \beta_1\,\beta_4 \\ 0 & 0 & -1 & 0 & 0 & 1 \end{bmatrix} \tag{4.23}$$

where

$$\begin{aligned}
\beta_1 &= \sin\theta^{[i]} \\
\beta_2 &= \cos\theta^{[i]} \\
\beta_3 &= \cos\Phi^{(k)}\left(x_C^{[i]} - {x_G}^{(k)}\right) - \sin\Phi^{(k)}\left(y_C^{[i]} - {y_G}^{(k)}\right) \\
\beta_4 &= \cos\Phi^{(k)}\left(y_C^{[i]} - {y_G}^{(k)}\right) + \sin\Phi^{(k)}\left(x_C^{[i]} - {x_G}^{(k)}\right) \\
\beta_5 &= \cos\Phi^{(j)}\left(x_C^{[i]} - {x_G}^{(j)}\right) - \sin\Phi^{(j)}\left(y_C^{[i]} - {y_G}^{(j)}\right) \\
\beta_6 &= \cos\Phi^{(j)}\left(y_C^{[i]} - {y_G}^{(j)}\right) + \sin\Phi^{(j)}\left(x_C^{[i]} - {x_G}^{(j)}\right)
\end{aligned} \tag{4.24}$$

Let us collect the external loads applied at the centers of mass of the two rigid blocks in the following vector $\mathbf{F}_e = [F_x^{(j)}, F_y^{(j)}, C^{(j)}, F_x^{(k)}, F_y^{(k)}, C^{(k)}]^T$, expressed in the global reference system. The equilibrium relation of two rigid blocks is given by:

$$\mathbf{\Gamma} = \mathbf{F}_i - \mathbf{F}_e = \mathbf{0} \tag{4.25}$$

where, considering Eq.(4.20), the internal forces are given by:

$$\mathbf{F}_i = \left(\hat{\mathbf{B}} + \tilde{\mathbf{B}}\right)^T \hat{\mathbf{S}}^{[i]} \tag{4.26}$$

and $\mathbf{\Gamma}$ represents the residual force.

The internal forces vector $\mathbf{F}_i$ is a nonlinear function of the unknown $\mathbf{d}$ and assumes the role of the residual vector in the Newton-Raphson iterative scheme that will be detailed in the following. The tangent stiffness matrix of the i-th interface between two rigid blocks is obtained by linearizing the residual at each iteration k:

$$\mathbf{K}^{[i]} = \frac{\partial \mathbf{\Gamma}}{\partial \mathbf{d}} = \frac{\partial \mathbf{F}_i}{\partial \mathbf{d}} \tag{4.27}$$

Substituting the Eq.(4.26) into the Eq.(4.27) yields the following expression:

$$\mathbf{K}^{[i]} = \frac{\partial(\hat{\mathbf{B}} + \tilde{\mathbf{B}})^T}{\partial \mathbf{d}} \hat{\mathbf{S}}^{[i]} + (\hat{\mathbf{B}} + \tilde{\mathbf{B}})^T \frac{\partial \hat{\mathbf{S}}^{[i]}}{\partial \hat{\mathbf{s}}^{[i]}} (\hat{\mathbf{B}} + \tilde{\mathbf{B}}) \tag{4.28}$$

where $\dfrac{\partial \hat{\mathbf{S}}^{[i]}}{\partial \hat{\mathbf{s}}^{[i]}}$ represents the tangent interface constitutive matrix whose expression will be detailed in the next section.

To summarize, the tangent stiffness matrix that accounts for both the geometrical contribution, ${\mathbf{K}_g}^{[i]}$, and the material contribution, ${\mathbf{K}_m}^{[i]}$, reads as follows:

$$\mathbf{K}^{[i]} = {\mathbf{K}_g}^{[i]} + {\mathbf{K}_m}^{[i]} \tag{4.29}$$

About the geometrical stiffness contribution, the two partial derivatives of the matrix $\hat{\mathbf{B}}$ and the matrix $\tilde{\mathbf{B}}$ with respect to the Lagrangian parameters vector $\mathbf{d}$ are denoted as $\hat{\mathbf{A}}$ and $\tilde{\mathbf{A}}$:

$${\mathbf{K}_g}^{[i]} = \frac{\partial(\hat{\mathbf{B}} + \tilde{\mathbf{B}})^T}{\partial \mathbf{d}} \hat{\mathbf{S}}^{[i]} \tag{4.30}$$

$${\mathbf{K}_g}^{[i]} = \frac{\partial \hat{\mathbf{B}}^T}{\partial \mathbf{d}} \hat{\mathbf{S}}^{[i]} + \frac{\partial \tilde{\mathbf{B}}^T}{\partial \mathbf{d}} \hat{\mathbf{S}}^{[i]} \tag{4.31}$$

$${\mathbf{K}_g}^{[i]} = \hat{\mathbf{A}} \hat{\mathbf{S}}^{[i]} + \tilde{\mathbf{A}} \hat{\mathbf{S}}^{[i]} \tag{4.32}$$

and so in components:

$$K_{g,ij}^{[i]} = \frac{\partial(\hat{B}_{ik} + \tilde{B}_{ik})}{\partial d_j} \hat{S}_k^{[i]} \tag{4.33}$$

$$K_{g,ij}^{[i]} = \hat{A}_{ikj} \hat{S}_k^{[i]} + \tilde{A}_{ikj} \hat{S}_k^{[i]} \tag{4.34}$$

As a deduction from the previous steps, the geometrical stiffness matrix consists of the

following two matrices, denoted as $\hat{\mathbf{K}}_g$ and $\tilde{\mathbf{K}}_g$:

$$\mathbf{K}_g{}^{[i]} = \hat{\mathbf{K}}_g + \tilde{\mathbf{K}}_g \tag{4.35}$$

In particular:

$$\hat{\mathbf{K}}_g = \begin{bmatrix} 0 & 0 & 0 & 0 & 0 & 0 \\ 0 & 0 & 0 & 0 & 0 & 0 \\ \gamma_6 & \gamma_5 & \gamma_2 & \gamma_3 & \gamma_4 & \gamma_1 \\ 0 & 0 & 0 & 0 & 0 & 0 \\ 0 & 0 & 0 & 0 & 0 & 0 \\ \gamma_6 & \gamma_5 & \gamma_2 & \gamma_3 & \gamma_4 & \gamma_1 \end{bmatrix} \tag{4.36}$$

where

$$\begin{aligned}
\gamma_1 &= N^{[i]} \left(\frac{\gamma_{14}\,\gamma_8}{2} - \frac{\gamma_{13}\,\gamma_7}{2} + \frac{\gamma_{14}\,\gamma_9}{4} - \frac{\gamma_{13}\,\gamma_{10}}{4} \right) + ... \\
&\quad T^{[i]} \left(\frac{\gamma_{14}\,\gamma_7}{2} + \frac{\gamma_{13}\,\gamma_8}{2} + \frac{\gamma_{14}\,\gamma_{10}}{4} + \frac{\gamma_{13}\,\gamma_9}{4} \right) \\
\gamma_2 &= N^{[i]} \left(-\frac{\gamma_{14}\,\gamma_{12}}{2} + \frac{\gamma_{13}\,\gamma_{11}}{2} + \frac{\gamma_{14}\,\gamma_9}{4} - \frac{\gamma_{13}\,\gamma_{10}}{4} \right) + ... \\
&\quad + T^{[i]} \left(-\frac{\gamma_{14}\,\gamma_{11}}{2} - \frac{\gamma_{13}\,\gamma_{12}}{2} + \frac{\gamma_{14}\,\gamma_{10}}{4} + \frac{\gamma_{13}\,\gamma_9}{4} \right) \\
\gamma_3 &= -\frac{N^{[i]}\,\gamma_{14}}{2} - \frac{T^{[i]}\,\gamma_{13}}{2} \\
\gamma_4 &= \frac{T^{[i]}\,\gamma_{14}}{2} - \frac{N^{[i]}\,\gamma_{13}}{2} \\
\gamma_5 &= \frac{N^{[i]}\,\gamma_{13}}{2} - \frac{T^{[i]}\,\gamma_{14}}{2} \\
\gamma_6 &= \frac{N^{[i]}\,\gamma_{14}}{2} + \frac{T^{[i]}\,\gamma_{13}}{2}
\end{aligned} \tag{4.37}$$

with

$$\gamma_7 = \cos\Phi^{(k)}\,(x_C^{[i]} - x_G{}^{(k)}) - \sin\Phi^{(k)}\,(y_C^{[i]} - y_G{}^{(k)})$$

$$\gamma_8 = \cos\Phi^{(k)}\,(y_C^{[i]} - y_G{}^{(k)}) + \sin\Phi^{(k)}\,(x_C^{[i]} - x_G{}^{(k)})$$

$$\gamma_9 = V^{(j)} - V^{(k)} + \left(\cos\Phi^{(j)} - 1\right)(y_C^{[i]} - y_G{}^{(j)}) - \left(\cos\Phi^{(k)} - 1\right)(y_C^{[i]} - y_G{}^{(k)}) + ...$$

$$+ \sin\Phi^{(j)}\,(x_C^{[i]} - x_G{}^{(j)}) - \sin\Phi^{(k)}\,(x_C^{[i]} - x_G{}^{(k)})$$

$$\gamma_{10} = U^{(j)} - U^{(k)} + \left(\cos\Phi^{(j)} - 1\right)(x_C^{[i]} - x_G{}^{(j)}) - \left(\cos\Phi^{(k)} - 1\right)(x_C^{[i]} - x_G{}^{(k)}) + ...$$

$$- \sin\Phi^{(j)}\,(y_C^{[i]} - y_G{}^{(j)}) + \sin\Phi^{(k)}\,(y_C^{[i]} - y_G{}^{(k)})$$

$$\gamma_{11} = \cos\Phi^{(j)}\,(x_C^{[i]} - x_G{}^{(j)}) - \sin\Phi^{(j)}\,(y_C^{[i]} - y_G{}^{(j)})$$

$$\gamma_{12} = \cos\Phi^{(j)}\,(y_C^{[i]} - y_G{}^{(j)}) + \sin\Phi^{(j)}\,(x_C^{[i]} - x_G{}^{(j)})$$

$$\gamma_{13} = \sin\theta^{[i]}$$

$$\gamma_{14} = \cos\theta^{[i]} \tag{4.38}$$

and

$$\tilde{\mathbf{K}}_g = \begin{bmatrix} 0 & 0 & \delta_8 & 0 & 0 & \delta_8 \\ 0 & 0 & \delta_7 & 0 & 0 & \delta_7 \\ 0 & 0 & \delta_4 + \delta_2 & 0 & 0 & -\delta_4 - \delta_2 \\ 0 & 0 & \delta_5 & 0 & 0 & \delta_5 \\ 0 & 0 & \delta_6 & 0 & 0 & \delta_6 \\ 0 & 0 & \delta_3 + \delta_1 & 0 & 0 & -\delta_3 - \delta_1 \end{bmatrix} \tag{4.39}$$

where

$$
\begin{aligned}
\delta_1 &= T^{[i]} \left(\frac{\delta_{14}\,\delta_9}{2} + \frac{\delta_{13}\,\delta_{10}}{2} \right) \\
\delta_2 &= T^{[i]} \left(\frac{\delta_{14}\,\delta_{11}}{2} + \frac{\delta_{13}\,\delta_{12}}{2} \right) \\
\delta_3 &= N^{[i]} \left(\frac{\delta_{14}\,\delta_{10}}{2} - \frac{\delta_{13}\,\delta_9}{2} \right) \\
\delta_4 &= N^{[i]} \left(\frac{\delta_{14}\,\delta_{12}}{2} - \frac{\delta_{13}\,\delta_{11}}{2} \right) \\
\delta_5 &= -\frac{N^{[i]}\,\delta_{14}}{2} - \frac{T^{[i]}\,\delta_{13}}{2} \\
\delta_6 &= \frac{T^{[i]}\,\delta_{14}}{2} - \frac{N^{[i]}\,\delta_{13}}{2} \\
\delta_7 &= \frac{N^{[i]}\,\delta_{13}}{2} - \frac{T^{[i]}\,\delta_{14}}{2} \\
\delta_8 &= \frac{N^{[i]}\,\delta_{14}}{2} + \frac{T^{[i]}\,\delta_{13}}{2}
\end{aligned}
\tag{4.40}
$$

with

$$\begin{aligned}
\delta_9 &= \cos\Phi^{(k)}\left(x_C^{[i]} - {x_G}^{(k)}\right) - \sin\Phi^{(k)}\left(y_C^{[i]} - {y_G}^{(k)}\right) \\
\delta_{10} &= \cos\Phi^{(k)}\left(y_C^{[i]} - {y_G}^{(k)}\right) + \sin\Phi^{(k)}\left(x_C^{[i]} - {x_G}^{(k)}\right) \\
\delta_{11} &= \cos\Phi^{(j)}\left(x_C^{[i]} - {x_G}^{(j)}\right) - \sin\Phi^{(j)}\left(y_C^{[i]} - {y_G}^{(j)}\right) \\
\delta_{12} &= \cos\Phi^{(j)}\left(y_C^{[i]} - {y_G}^{(j)}\right) + \sin\Phi^{(j)}\left(x_C^{[i]} - {x_G}^{(j)}\right) \\
\delta_{13} &= \sin\theta^{[i]} \\
\delta_{14} &= \cos\theta^{[i]}
\end{aligned} \tag{4.41}$$

It can be observed that the geometrical stiffness matrix ${\mathbf{K}_g}^{[i]}$ is symmetric. By defining the matrix $\mathbf{B} := \hat{\mathbf{B}} + \tilde{\mathbf{B}}$, the contribution to material stiffness can be expressed as follows:

$${\mathbf{K}_m}^{[i]} = \mathbf{B}^T \frac{\partial \hat{\mathbf{S}}^{[i]}}{\partial \hat{\mathbf{s}}^{[i]}} \mathbf{B} \tag{4.42}$$

To further simplify the notation of Eq.(4.28), the interface stiffness matrix is written as:

$$\mathbf{K}^{[i]} = \frac{\partial \mathbf{B}^T}{\partial \mathbf{d}} \hat{\mathbf{S}}^{[i]} + \mathbf{B}^T \frac{\partial \hat{\mathbf{S}}^{[i]}}{\partial \hat{\mathbf{s}}^{[i]}} \mathbf{B} \tag{4.43}$$

4.2 Moderate Rotations

Significant block rotations can cause highly nonlinear problems, potentially leading to solution convergence issues and increased computational cost. This is due to the presence of sine and cosine functions in the rotation matrix of the rigid body equation of motion, as discussed in Subsection 4.1.1.

After reviewing the scientific literature on the Discrete Element Method (DEM), it was found that adopting a second-order approximation of the sine and cosine functions of rotations within the rotation matrix can mitigate errors [28, 30, 35]. However, these techniques have mainly been used to address the issue of false volume expansion, as demonstrated in the work by Jiang et al. [66]. Shi discussed how the use of deformable blocks in Discontinuous Deformation Analysis (DDA) can lead to issues [20]. This problem is particularly significant in various geotechnical engineering applications.

The proposed model applies the Moderate Rotation approximation [19, 22] to rigid blocks in dry masonry structures. This theory expands the series of sine and cosine functions of the rotation of the centroid of each block within the rotation matrix. This approach may reduce the computational burden of the problem while maintaining its nonlinearity.

4.2.1 Rigid Block Kinematics

By applying the series expansion of the sine and cosine functions of the rotation to the centroid of each block, Φ, as follows:

$$\sin(\Phi) = \Phi + o(\Phi) \approx \Phi$$

$$\cos(\Phi) = 1 - \frac{1}{2}\Phi^2 + o(\Phi^2) \approx 1 - \frac{1}{2}\Phi^2$$

Equation (4.2) becomes:

$$\mathbf{R} = \begin{bmatrix} 1 - \frac{1}{2}\Phi^2 & -\Phi \\ \Phi & 1 - \frac{1}{2}\Phi^2 \end{bmatrix} \tag{4.44}$$

In the following subsection, only the modifications made to the model of Subsection 4.1 are reported, now considering the approximation of moderate rotations instead of the implementation of finite rotations in the context of large displacements.

By replacing Eq.(4.44) in Eq.(4.1), the rigid displacement field of a single block is defined.

4.2.2 Interface Kinematics

The displacement fields of two rigid blocks sharing an interface are examined to study interface kinematics. The relative displacement vector at the midpoint of the interface is calculated, as defined in Subsection 4.1.2. The vector of kinematic interface parameters, denoted as $\mathbf{s}^{[i]} = [\Delta u_x^{[i]}, \Delta u_y^{[i]}, \psi^{[i]}]^T$, is defined in the global frame as follows:

$$\mathbf{s}^{[i]} = \begin{Bmatrix} \Delta u_x^{[i]} \\ \Delta u_y^{[i]} \\ \psi^{[i]} \end{Bmatrix} = \begin{Bmatrix} U^{(k)} - \Phi^{(k)}(y_C^{[i]} - {y_G}^{(k)}) - \frac{1}{2}{\Phi^{(k)}}^2(x_C^{[i]} - {x_G}^{(k)}) + ... \\ -[U^{(j)} - \Phi^{(j)}(y_C^{[i]} - {y_G}^{(j)}) - \frac{1}{2}{\Phi^{(j)}}^2(x_C^{[i]} - {x_G}^{(j)})] \\ V^{(k)} + \Phi^{(k)}(x_C^{[i]} - {x_G}^{(k)}) - \frac{1}{2}{\Phi^{(k)}}^2(y_C^{[i]} - {y_G}^{(k)}) + ... \\ -[V^{(j)} + \Phi^{(j)}(x_C^{[i]} - {x_G}^{(j)}) - \frac{1}{2}{\Phi^{(j)}}^2(y_C^{[i]} - {y_G}^{(j)})] \\ \Phi^{(k)} - \Phi^{(j)} \end{Bmatrix} \tag{4.45}$$

The actual interface angle, $\theta^{[i]}$, is defined in Eq.(4.6). Therefore it is possible to evaluate the relative displacement in the local frame, $\hat{\mathbf{s}}^{[i]} = [\Delta\hat{u}_t^{[i]}, \Delta\hat{u}_n^{[i]}, \psi^{[i]}]^T$, as described in Eq.(4.7), considering that the local rotation matrix $\hat{\mathbf{R}}^{[i]}$ is given by Eq.(4.8).

Considering the approximation of moderate rotations, the displacement of the typical point along the interface, denoted as $\boldsymbol{\Delta}\tilde{\mathbf{u}}^{[i]} = [\Delta\tilde{u}_t^{[i]}, \Delta\tilde{u}_n^{[i]}]^T$, is simplified as follows:

$$\boldsymbol{\Delta}\tilde{\mathbf{u}}^{[i]} = \left\{ \begin{array}{c} \Delta\hat{u}_t^{[i]} \\ \Delta\hat{u}_n^{[i]} + \xi\psi^{[i]} \end{array} \right\} \tag{4.46}$$

4.2.3 Equilibrium Equations

Furthermore, in the analysis of the static equilibrium equations outlined in Subsection 4.1.3, the derivation of the governing equations for the system is performed. Consequently, when evaluating the interface vector in Eq.(4.45), a noticeable variation in the components of the two matrices, $\hat{\mathbf{B}}$ and $\tilde{\mathbf{B}}$ is found.

In particular:

$$\hat{\mathbf{B}} = \begin{bmatrix} 0 & 0 & \alpha_1 & 0 & 0 & \alpha_1 \\ 0 & 0 & \alpha_2 & 0 & 0 & \alpha_2 \\ 0 & 0 & 0 & 0 & 0 & 0 \end{bmatrix} \tag{4.47}$$

where

$$\alpha_1 = \frac{\sin\theta^{[i]}\,\alpha_4}{2} - \frac{\cos\theta^{[i]}\,\alpha_3}{2}$$

$$\alpha_2 = \frac{\cos\theta^{[i]}\;\alpha_4}{2} + \frac{\sin\theta^{[i]}\,\alpha_3}{2}$$

with

$$\begin{aligned} \alpha_3 &= V^{(j)} + \Phi^{(j)}(x_C^{[i]} - {x_G}^{(j)}) - \frac{1}{2}{\Phi^{(j)}}^2(y_C^{[i]} - {y_G}^{(j)}) + ... \\ &-[V^{(k)} + \Phi^{(k)}(x_C^{[i]} - {x_G}^{(k)}) - \frac{1}{2}{\Phi^{(k)}}^2(y_C^{[i]} - {y_G}^{(k)})] \end{aligned} \tag{4.48}$$

$$\begin{aligned} \alpha_4 &= U^{(j)} - \Phi^{(j)}(y_C^{[i]} - {y_G}^{(j)}) - \frac{1}{2}{\Phi^{(j)}}^2(x_C^{[i]} - {x_G}^{(j)}) + ... \\ &-[U^{(k)} - \Phi^{(k)}(y_C^{[i]} - {y_G}^{(k)}) - \frac{1}{2}{\Phi^{(k)}}^2(x_C^{[i]} - {x_G}^{(k)})] \end{aligned}$$

and

$$\tilde{\mathbf{B}} = \begin{bmatrix} -\beta_2 & -\beta_1 & \beta_2\,\beta_6 + \beta_1\,\beta_5 & \beta_2 & \beta_1 & \beta_1\,\beta_3 - \beta_2\,\beta_4 \\ \beta_1 & -\beta_2 & \beta_2\,\beta_5 - \beta_1\,\beta_6 & -\beta_1 & \beta_2 & -\beta_2\,\beta_3 + \beta_1\,\beta_4 \\ 0 & 0 & -1 & 0 & 0 & 1 \end{bmatrix} \tag{4.49}$$

where

$$\begin{aligned} \beta_1 &= \sin\theta^{[i]} \\ \beta_2 &= \cos\theta^{[i]} \\ \beta_3 &= \left(x_G{}^{(k)} - x_C^{[i]}\right) + \Phi^{(k)}\left(y_C^{[i]} - y_G{}^{(k)}\right) \\ \beta_4 &= \left(y_C^{[i]} - y_G{}^{(k)}\right) + \Phi^{(k)}\left(x_C^{[i]} - x_G{}^{(k)}\right) \\ \beta_5 &= \left(x_G{}^{(j)} - x_C^{[i]}\right) + \Phi^{(j)}\left(y_C^{[i]} - y_G{}^{(j)}\right) \\ \beta_6 &= \left(y_C^{[i]} - y_G{}^{(j)}\right) + \Phi^{(j)}\left(x_C^{[i]} - x_G{}^{(j)}\right) \end{aligned} \tag{4.50}$$

By performing the derivative of the internal forces vector $\mathbf{F}_i$ with respect to the Lagrangian parameter vector of two rigid blocks $\mathbf{d}$, the resulting tangent stiffness matrix is expressed in Eq.(4.29), where the different contributions of geometrical and material aspects are clearly delineated.

Therefore, the implementation of moderate rotations leads to changes in the geometrical stiffness matrix, $\mathbf{K}_g{}^{[i]}$, as defined in Eq.(4.35). The components of the two matrices, $\hat{\mathbf{K}}_g$ and $\tilde{\mathbf{K}}_g$, undergo the following modifications:

$$\hat{\mathbf{K}}_g = \begin{bmatrix} 0 & 0 & 0 & 0 & 0 & 0 \\ 0 & 0 & 0 & 0 & 0 & 0 \\ \gamma_4 & \gamma_2 & \gamma_6 & \gamma_1 & \gamma_3 & \gamma_5 \\ 0 & 0 & 0 & 0 & 0 & 0 \\ 0 & 0 & 0 & 0 & 0 & 0 \\ \gamma_4 & \gamma_2 & \gamma_6 & \gamma_1 & \gamma_3 & \gamma_5 \end{bmatrix} \tag{4.51}$$

where

$$\begin{aligned}
\gamma_1 &= -\frac{N^{[i]}\,\gamma_{14}}{2} - \frac{T^{[i]}\,\gamma_{13}}{2} \\
\gamma_2 &= \frac{N^{[i]}\,\gamma_{13}}{2} - \frac{T^{[i]}\,\gamma_{14}}{2} \\
\gamma_3 &= \frac{T^{[i]}\,\gamma_{14}}{2} - \frac{N^{[i]}\,\gamma_{13}}{2} \\
\gamma_4 &= \frac{N^{[i]}\,\gamma_{14}}{2} + \frac{T^{[i]}\,\gamma_{13}}{2} \\
\gamma_5 &= N^{[i]}\left(\frac{\gamma_{14}\,\gamma_8}{2} + \frac{\gamma_{13}\,\gamma_7}{2} + \frac{\gamma_{14}\,\gamma_9}{4} - \frac{\gamma_{13}\,\gamma_{10}}{4}\right) + \ldots \\
&+T^{[i]}\left(\frac{\gamma_{13}\,\gamma_8}{2} - \frac{\gamma_{14}\,\gamma_7}{2} + \frac{\gamma_{14}\,\gamma_{10}}{4} + \frac{\gamma_{13}\,\gamma_9}{4}\right) \\
\gamma_6 &= T^{[i]}\left(\frac{\gamma_{14}\,\gamma_{11}}{2} - \frac{\gamma_{13}\,\gamma_{12}}{2} + \frac{\gamma_{14}\,\gamma_{10}}{4} + \frac{\gamma_{13}\,\gamma_9}{4}\right) + \ldots \\
&-N^{[i]}\left(\frac{\gamma_{14}\,\gamma_{12}}{2} + \frac{\gamma_{13}\,\gamma_{11}}{2} - \frac{\gamma_{14}\,\gamma_9}{4} + \frac{\gamma_{13}\,\gamma_{10}}{4}\right)
\end{aligned} \tag{4.52}$$

with

$$
\begin{aligned}
\gamma_7 &= \left(x_G{}^{(k)} - x_C^{[i]}\right) + \Phi^{(k)}\left(y_C^{[i]} - y_G{}^{(k)}\right) \\
\gamma_8 &= \left(y_C^{[i]} - y_G{}^{(k)}\right) + \Phi^{(k)}\left(x_C^{[i]} - x_G{}^{(k)}\right) \\
\gamma_9 &= V^{(j)} + \Phi^{(j)}(x_C^{[i]} - x_G{}^{(j)}) - \frac{1}{2}\Phi^{(j)^2}(y_C^{[i]} - y_G{}^{(j)}) + ... \\
&-[V^{(k)} + \Phi^{(k)}(x_C^{[i]} - x_G{}^{(k)}) - \frac{1}{2}\Phi^{(k)^2}(y_C^{[i]} - y_G{}^{(k)})] \\
\gamma_{10} &= U^{(j)} - \Phi^{(j)}(y_C^{[i]} - y_G{}^{(j)}) - \frac{1}{2}\Phi^{(j)^2}(x_C^{[i]} - x_G{}^{(j)}) + ... \\
&-[U^{(k)} - \Phi^{(k)}(y_C^{[i]} - y_G{}^{(k)}) - \frac{1}{2}\Phi^{(k)^2}(x_C^{[i]} - x_G{}^{(k)})] \\
\gamma_{11} &= \left(x_G{}^{(j)} - x_C^{[i]}\right) + \Phi^{(j)}\left(y_C^{[i]} - y_G{}^{(j)}\right) \\
\gamma_{12} &= \left(y_C^{[i]} - y_G{}^{(j)}\right) + \Phi^{(j)}\left(x_C^{[i]} - x_G{}^{(j)}\right) \\
\gamma_{13} &= \sin\theta^{[i]} \\
\gamma_{14} &= \cos\theta^{[i]}
\end{aligned}
\tag{4.53}
$$

and

$$
\tilde{\mathbf{K}}_g = \begin{bmatrix}
0 & 0 & \delta_1 & 0 & 0 & \delta_1 \\
0 & 0 & \delta_2 & 0 & 0 & \delta_2 \\
0 & 0 & \delta_3 & 0 & 0 & \delta_3 \\
0 & 0 & \delta_4 & 0 & 0 & \delta_4 \\
0 & 0 & \delta_5 & 0 & 0 & \delta_5 \\
0 & 0 & \delta_6 & 0 & 0 & \delta_6
\end{bmatrix}
\tag{4.54}
$$

where

$$
\begin{aligned}
\delta_1 &= \frac{N^{[i]}\,\delta_{14}}{2} + \frac{T^{[i]}\,\delta_{13}}{2} \\
\delta_2 &= \frac{N^{[i]}\,\delta_{13}}{2} - \frac{T^{[i]}\,\delta_{14}}{2} \\
\delta_3 &= T^{[i]}\left(\frac{\delta_{14}\,\delta_{11}}{2}\right) - \frac{\delta_{13}\,\delta_{12}}{2} + \delta_{14}\delta_{15} + \delta_{13}\delta_{16} + ... \\
&\quad -N^{[i]}\left(\frac{\delta_{14}\,\delta_{12}}{2}\right) + \frac{\delta_{13}\,\delta_{11}}{2} - \delta_{14}\delta_{16} + \delta_{13}\delta_{15} \\
\delta_4 &= T^{[i]}\left(\frac{\delta_{14}\,\delta_{11}}{2}\right) - \frac{\delta_{13}\,\delta_{12}}{2} - N^{[i]}\left(\frac{\delta_{14}\,\delta_{12}}{2}\right) + \frac{\delta_{13}\,\delta_{11}}{2} \\
\delta_5 &= -\frac{N^{[i]}\,\delta_{14}}{2} - \frac{T^{[i]}\,\delta_{13}}{2} \\
\delta_6 &= \frac{T^{[i]}\,\delta_{14}}{2} - \frac{N^{[i]}\,\delta_{13}}{2} \\
\delta_7 &= N^{[i]}\left(\frac{\delta_{14}\,\delta_{10}}{2}\right) + \frac{\delta_{13}\,\delta_{9}}{2} - T^{[i]}\left(\frac{\delta_{14}\,\delta_{9}}{2}\right) - \frac{\delta_{13}\,\delta_{10}}{2} \\
\delta_8 &= N^{[i]}\left(\frac{\delta_{14}\,\delta_{10}}{2}\right) + \frac{\delta_{13}\,\delta_{9}}{2} - \delta_{14}\delta_7 + \delta_{13}\delta_8 + ... \\
&\quad -T^{[i]}\left(\frac{\delta_{14}\,\delta_{9}}{2}\right) - \frac{\delta_{13}\,\delta_{10}}{2} + \delta_{14}\delta_8 + \delta_{13}\delta_7
\end{aligned}
\tag{4.55}
$$

with

$$
\begin{aligned}
\delta_7 &= \left(y_C^{[i]} - {y_G}^{(k)}\right) \\
\delta_8 &= \left(x_C^{[i]} - {x_G}^{(k)}\right) \\
\delta_9 &= \left({x_G}^{(k)} - x_C^{[i]}\right) + \Phi^{(k)}\left(y_C^{[i]} - {y_G}^{(k)}\right) \\
\delta_{10} &= \left(y_C^{[i]} - {y_G}^{(k)}\right) + \Phi^{(k)}\left(x_C^{[i]} - {x_G}^{(k)}\right) \\
\delta_{11} &= \left({x_G}^{(j)} - x_C^{[i]}\right) + \Phi^{(j)}\left(y_C^{[i]} - {y_G}^{(j)}\right) \\
\delta_{12} &= \left(y_C^{[i]} - {y_G}^{(j)}\right) + \Phi^{(j)}\left(x_C^{[i]} - {x_G}^{(j)}\right) \\
\delta_{13} &= \sin\theta^{[i]} \\
\delta_{14} &= \cos\theta^{[i]} \\
\delta_{15} &= \left(x_C^{[i]} - {x_G}^{(j)}\right) \\
\delta_{16} &= \left(y_C^{[i]} - {y_G}^{(j)}\right)
\end{aligned}
\tag{4.56}
$$

It can be observed that the geometrical stiffness matrix ${\mathbf{K}_g}^{[i]}$ is always symmetric.

4.3 Small Displacements

The hypothesis of small displacements is a kinematic assumption used to analyze problems with sufficiently small displacements. This model has a different formulation compared to the one used for large displacements [56]. Specifically, the displacements are so small that (i) they can be expressed as linear functions of the Lagrangian parameters, and (ii) equilibrium is established in the initial configuration [24, 47].

This subsection explains the linear model in the context of geometrical linearity, which simplifies the formulation significantly.

4.3.1 Rigid Block Kinematics

Linear theory assumes that:

$$\cos \Phi^{(j)} = 1$$

$$\sin \Phi^{(j)} = \Phi^{(j)}$$

resulting in the simplified rotation matrix:

$$\mathbf{R}^{(j)} = \begin{bmatrix} 1 & -\Phi^{(j)} \\ \Phi^{(j)} & 1 \end{bmatrix} \tag{4.57}$$

The kinematics of a rigid block involves using the linear rotation matrix $\mathbf{R}^{(j)}$, as introduced in Eq.(4.57), in Eq.(4.1).

4.3.2 Interface Kinematics

When analyzing the kinematics of two rigid blocks with small displacements, the problem becomes linear because the rotation matrices, $\mathbf{R}^{(j)}$ and $\mathbf{R}^{(k)}$, do not contain trigonometric functions. Additionally, a linear operator, so-called strain-displacement matrix

$\bar{\mathbf{B}}$, can be used to evaluate relative displacement in the global frame.

The relative displacement vector is defined as follows:

$$\mathbf{s}^{[i]} = \bar{\mathbf{B}}\mathbf{d} \tag{4.58}$$

$$\mathbf{s}^{[i]} = \begin{Bmatrix} \Delta u_x^{[i]} \\ \Delta u_y^{[i]} \\ \psi^{[i]} \end{Bmatrix} = \begin{bmatrix} -1 & 0 & (y_C^{[i]} - y_G^{(j)}) & 1 & 0 & -(y_C^{[i]} - y_G^{(k)}) \\ 0 & -1 & -(x_C^{[i]} - x_G^{(j)}) & 0 & 1 & (x_C^{[i]} - x_G^{(k)}) \\ 0 & 0 & -1 & 0 & 0 & 1 \end{bmatrix} \begin{Bmatrix} U^{(j)} \\ V^{(j)} \\ \Phi^{(j)} \\ U^{(k)} \\ V^{(k)} \\ \Phi^{(k)} \end{Bmatrix}$$

where $\bar{\mathbf{B}}$ is the linear operator, and $\mathbf{d} = [U^{(j)}, V^{(j)}, \Phi^{(j)}, U^{(k)}, V^{(k)}, \Phi^{(k)}]^T$ is the vector that collects all Lagrangian parameters of two rigid blocks.

The components of the relative displacement, $\mathbf{s}^{[i]}$, in the global frame are:

$$\mathbf{s}^{[i]} = \begin{Bmatrix} \Delta u_x^{[i]} \\ \Delta u_y^{[i]} \\ \psi^{[i]} \end{Bmatrix} = \begin{Bmatrix} U^{(k)} - \Phi^{(k)}(y_C^{[i]} - {y_G}^{(k)}) - [U^{(j)} - \Phi^{(j)}(y_C^{[i]} - {y_G}^{(j)})] \\ V^{(k)} + \Phi^{(k)}(x_C^{[i]} - {x_G}^{(k)}) - [V^{(j)} + \Phi^{(j)}(x_C^{[i]} - {x_G}^{(j)})] \\ \Phi^{(k)} - \Phi^{(j)} \end{Bmatrix}$$

The linear model assumes that the interface angle in the current configuration, $\theta^{[i]}$, is the same as in the initial configuration, ψ_0. Therefore, the formulation is modified as follows:

$$\theta^{[i]} = \psi_0 \tag{4.59}$$

By substituting the Eq.(4.59) into the Eq.(4.8), it is possible to evaluate the relative displacement in the local frame, $\hat{\mathbf{s}}^{[i]} = [\Delta\hat{u}_t^{[i]}, \Delta\hat{u}_n^{[i]}, \psi^{[i]}]^T$, as described in Eq.(4.7).

To define the relative displacement vector in the local frame, a linear operator can be used:

$$\hat{\mathbf{s}}^{[i]} = \hat{\mathbf{R}}^{[i]}\mathbf{s}^{[i]} = \hat{\mathbf{R}}^{[i]}\bar{\mathbf{B}}\mathbf{d} = \mathbf{B}\mathbf{d} \tag{4.60}$$

where $\mathbf{B}$ is the linear operator in the local frame. It is important to note that, for small displacements, the operator $\hat{\mathbf{R}}^{[i]}$ is independent of the displacement field.

In this case, the relative displacement along the interface becomes:

$$\boldsymbol{\Delta}\tilde{\mathbf{u}}^{[i]} = \left\{ \begin{array}{c} \Delta\hat{u}_t^{[i]} \\ \Delta\hat{u}_n^{[i]} + \xi\psi^{[i]} \end{array} \right\} \tag{4.61}$$

4.3.3 Equilibrium Equations

The definition of internal forces is as follows:

$$\mathbf{F}_i = \mathbf{B}^T\hat{\mathbf{S}}^{[i]} \tag{4.62}$$

where $\mathbf{B}$ represents the linear operator in the local frame, and the vector $\hat{\mathbf{S}}^{[i]} = [T^{[i]}, N^{[i]}, M^{[i]}]^T$ assembles the interface stress components.

In small displacements theory, the interface stiffness matrix is given by:

$$\mathbf{K}^{[i]} = \mathbf{B}^T\frac{\partial\hat{\mathbf{S}}^{[i]}}{\partial\hat{\mathbf{s}}^{[i]}}\mathbf{B} \tag{4.63}$$

In the scenario of small displacements, the interface stiffness matrix defined in Eq.(4.43) only consists of the second material contribution, i.e. $\mathbf{K}_g{}^{[i]} = \mathbf{0}$.

5 Interface Models

This section explores and integrates various interface models into the proposed rigid block models, with a focus on formulating material and contact nonlinearity.

Rigid block models are often effective in studying masonry structures, as they consider the impact of high compressive strength and low deformability of the block in relation to joint opening and sliding. Nonlinear behavior mainly occurs at these interfaces, leading to significant displacements, damage, unilateral contact, and frictional effects. The distinct element method (DEM) is commonly used to model the concentration of nonlinear behavior in masonry structures. The DEM is suitable for simulating large displacements, as discussed in the preceding section. In these approaches, contact is simulated through an interface spring system. For further information on contact, refer to Lemos' work [54].

The following section models elastic contact between blocks using normal and shear springs, as shown in Fig.11. Different constitutive laws are used for block contacts to analyze no-tension behavior, typical of masonry. Finally, a cohesive zone model, a reinterpretation of the model introduced by Alfano and Sacco, is presented that combines damage and friction [51, 58].

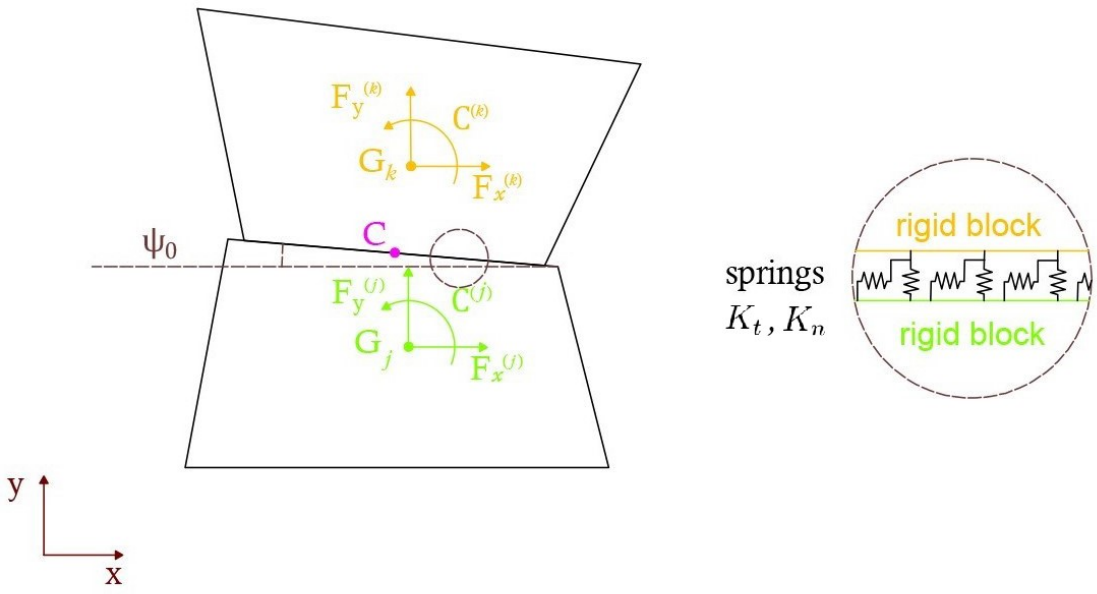

Figure 11: Interface model with normal and tangential springs.

5.1 No-tension Elastic Interfaces with No Slip

This subsection examines two different types of interface constitutive laws, both featuring no slip.

The interface kinematic parameters from Subsection 4.1.2 and the static parameters from Subsection 4.1.3 are considered.

Initially, a linear elastic constitutive law is adopted and formulated as follows:

$$\hat{\mathbf{S}}^{[i]} = \mathbf{D}\hat{\mathbf{s}}^{[i]} \tag{5.1}$$

where $\hat{\mathbf{S}}^{[i]} = [T^{[i]}, N^{[i]}, M^{[i]}]^T$, $\hat{\mathbf{s}}^{[i]} = [\Delta\hat{u}_t^{[i]}, \Delta\hat{u}_n^{[i]}, \psi^{[i]}]^T$, and the constitutive matrix $\mathbf{D}$

is:

$$\mathbf{D} = \begin{bmatrix} K_t & 0 & 0 \\ 0 & K_n & 0 \\ 0 & 0 & K_\phi \end{bmatrix} \tag{5.2}$$

The mechanical parameters K_t, K_n, and K_ϕ represent the tangential, normal, and rotational stiffness of the contact surfaces, respectively.

Using the 2D co-rotational reference system and the local abscissa ξ along the interface, the stress components of the interface can be calculated as follows:

$$\hat{\mathbf{S}}^{[i]} = \int_\xi \begin{Bmatrix} \tau \\ \sigma \\ \xi\sigma \end{Bmatrix} d\xi = \int_\xi \begin{Bmatrix} K_t \Delta\tilde{u}_t^{[i]} \\ K_n \Delta\tilde{u}_n^{[i]} \\ \xi K_n \Delta\tilde{u}_n^{[i]} \end{Bmatrix} d\xi \tag{5.3}$$

where τ and σ are the shear and normal material stresses, and K_t and K_n represent the interface mechanical parameters of normal and tangential stiffness.

By substituting the kinematic parameters along the interface from Eq.(4.10) into Eq.(5.3), let us obtain:

$$\hat{\mathbf{S}}^{[i]} = \int_\xi \begin{Bmatrix} K_t \Delta\hat{u}_t^{[i]} \\ K_n(\Delta\hat{u}_n^{[i]} + 2\xi \sin\dfrac{\psi^{[i]}}{2}) \\ \xi K_n(\Delta\hat{u}_n^{[i]} + 2\xi \sin\dfrac{\psi^{[i]}}{2}) \end{Bmatrix} d\xi \tag{5.4}$$

After performing the integral, the interface stress components for the linear elastic case are determined as follows:

$$\hat{\mathbf{S}}^{[i]} = \begin{Bmatrix} K_t L \Delta\hat{u}_t^{[i]} \\ K_n L \Delta\hat{u}_n^{[i]} \\ K_n \dfrac{L^3}{6} \sin\dfrac{\psi^{[i]}}{2} \end{Bmatrix} \tag{5.5}$$

where L is the length of the interface.

To analyze the no-tension interface behavior, which is typical of masonry structures, it is necessary to modify the integration limits of the integral in Eq.(5.4). In this second constitutive model, the interface stress components are evaluated only in the compressed part of the interface, within the limits ξ_1 and ξ_2. The procedure for calculating these limits will be detailed in the next section.

In the case of nonlinear contact, the interface stress vector is as follows:

$$\hat{\mathbf{S}}^{[i]} = \left\{ \begin{array}{c} K_t A^{[i]} \Delta \hat{u}_t^{[i]} \\ K_n (A^{[i]} \Delta \hat{u}_n^{[i]} + 2 S^{[i]} \sin \dfrac{\psi^{[i]}}{2}) \\ K_n (S^{[i]} \Delta \hat{u}_n^{[i]} + 2 J^{[i]} \sin \dfrac{\psi^{[i]}}{2}) \end{array} \right\} \tag{5.6}$$

where the area, $A^{[i]}$, the static moment, $S^{[i]}$, and the moment of inertia, $J^{[i]}$, of the interface in 2D are given by:

$$\begin{aligned} A^{[i]} &= \xi_2 - \xi_1 \\ S^{[i]} &= \frac{1}{2}({\xi_2}^2 - {\xi_1}^2) \\ J^{[i]} &= \frac{1}{3}({\xi_2}^3 - {\xi_1}^3) \end{aligned} \tag{5.7}$$

In a nonlinear problem, the constitutive matrix becomes a consistent tangent operator of the relationship between $\hat{\mathbf{S}}^{[i]}$ and $\hat{\mathbf{s}}^{[i]}$:

$$\mathbf{K}^t = \frac{\partial \hat{\mathbf{S}}^{[i]}}{\partial \hat{\mathbf{s}}^{[i]}} = \left[\begin{array}{ccc} K_t A^{[i]} & 0 & 0 \\ 0 & K_n A^{[i]} & K_n S^{[i]} \cos \dfrac{\psi}{2}^{[i]} \\ 0 & K_n S^{[i]} & K_n J^{[i]} \cos \dfrac{\psi}{2}^{[i]} \end{array} \right] \tag{5.8}$$

By substituting the expression of the constitutive relationship from Eq.(5.8) into Eq.(4.42), it is possible to evaluate the material stiffness matrix ${\mathbf{K}_m}^{[i]}$ for the nonlinear contact case.

5.2 Interface Cohesive Model combining Damage and Friction

To capture the behavior of interfaces between rigid blocks more realistically, especially under seismic loads, it is crucial to introduce a cohesive interface model that considers damage and friction in masonry structures. After introducing the no-tension behavior characteristic of some masonry, a decision was made to use a more complex constitutive model that accounts for damage, contact, and friction.

This subsection describes the implementation of the interface cohesive model, which combines damage and friction, to enrich the rigid block model in large displacements by exploring material nonlinearity issues [39]. The mechanical model proposed in [51, 52] serves as the basis for this implementation. In a micromechanical approach, the process of damaging a typical interface zone, characterized by area A, can be summarized in three states: (1) the undamaged interface zone, (2) partial decohesion, and (3) complete damage. According to this theory, the total area A at the interface can be divided into an undamaged part A_u and a completely damaged part A_d, such that $A = A_u + A_d$.

The damage parameter, represented as D, is defined as the ratio of the damaged portion to the total area:

$$D = \frac{A_d}{A} \tag{5.9}$$

The relative displacement vector at the typical point of the interface is denoted by $\boldsymbol{\Delta}\tilde{\mathbf{u}}^{[i]} = [\Delta\tilde{u}_t^{[i]}, \Delta\tilde{u}_n^{[i]}]^T$, as introduced in the Eq.(4.9). According to this combined damage-friction theory, the overall behavior of the interface can be obtained as a superposition of three schemes:

- In the first scenario, the relative displacement of the crack mouths is assumed experiencing an elastic relative displacement $\tilde{\mathbf{s}}^e = [\tilde{s}_t^e, \tilde{s}_n^e]^T$;
- In the second scenario, the occurrence of crack opening is considered, which leads to an inelastic relative displacement $\mathbf{c} = [0, c]^T$;
- In the third scenario, the interface at the crack mouths is subjected to an inelastic relative displacement for frictional sliding $\mathbf{p} = [p, 0]^T$.

Thus, the displacement at the interface can be determined:

$$\boldsymbol{\Delta}\tilde{\mathbf{u}}^{[i]} = \tilde{\mathbf{s}}^{e} + \mathbf{c} + \mathbf{p} \tag{5.10}$$

The stress vectors at the interface in the undamaged ($\boldsymbol{\tau}_u$) and damaged parts ($\boldsymbol{\tau}_d$) can be evaluated using the constitutive relationships as follows:

$$\boldsymbol{\tau}_u = \mathbf{K}\boldsymbol{\Delta}\tilde{\mathbf{u}}^{[i]} \tag{5.11}$$

$$\boldsymbol{\tau}_d = \mathbf{K}[\boldsymbol{\Delta}\tilde{\mathbf{u}}^{[i]} - (\mathbf{c} + \mathbf{p})] \tag{5.12}$$

where $\mathbf{K}$ is the constitutive matrix which collects the mechanical parameters K_t and K_n, introduced in the Eq.(5.2), as follows:

$$\mathbf{K} = \begin{bmatrix} K_t & 0 \\ 0 & K_n \end{bmatrix} \tag{5.13}$$

The overall interface stress vector can be evaluated as follows:

$$\boldsymbol{\tau} = \frac{A_u}{A}\boldsymbol{\tau}_u + \frac{A_d}{A}\boldsymbol{\tau}_d \tag{5.14}$$

By considering the Eqs.(5.9), (5.11), and (5.12), the previous equation can be rewritten as:

$$\begin{aligned} \boldsymbol{\tau} &= (1-D)\boldsymbol{\tau}_u + D\boldsymbol{\tau}_d \\ &= (1-D)\mathbf{K}\boldsymbol{\Delta}\tilde{\mathbf{u}}^{[i]} + D\mathbf{K}[\boldsymbol{\Delta}\tilde{\mathbf{u}}^{[i]} - (\mathbf{c} + \mathbf{p})] \\ &= \mathbf{K}[\boldsymbol{\Delta}\tilde{\mathbf{u}}^{[i]} - D(\mathbf{c} + \mathbf{p})] \end{aligned} \tag{5.15}$$

The stress vector $\boldsymbol{\tau}$ can be expressed in components based on the local coordinate system. This includes the stress vector acting on the undeformed area A_u, $\boldsymbol{\tau}_u$, and the

stress vector acting on the deformed area A_d, $\boldsymbol{\tau}_d$:

$$\boldsymbol{\tau}_u = \left\{ \begin{array}{c} \tau_u \\ \sigma_u \end{array} \right\}, \quad \boldsymbol{\tau}_d = \left\{ \begin{array}{c} \tau_d \\ \sigma_d \end{array} \right\}, \quad \boldsymbol{\tau} = \left\{ \begin{array}{c} \tau \\ \sigma \end{array} \right\} \tag{5.16}$$

where:

$$\tau_u = K_t \Delta \tilde{u}_t^{[i]} = K_t \Delta \hat{u}_t^{[i]} \tag{5.17}$$

$$\sigma_u = K_n \Delta \tilde{u}_n^{[i]} = K_n (\Delta \hat{u}_n^{[i]} + \xi\chi) \tag{5.18}$$

$$\tau_d = K_t (\Delta \tilde{u}_t^{[i]} - p) = K_t (\Delta \hat{u}_t^{[i]} - p) \tag{5.19}$$

$$\sigma_d = K_n (\Delta \tilde{u}_n^{[i]} - c) = K_n (\Delta \hat{u}_n^{[i]} + \xi\chi - c) \tag{5.20}$$

$$\tau = K_t (\Delta \tilde{u}_t^{[i]} - Dp) = K_t (\Delta \hat{u}_t^{[i]} - Dp) \tag{5.21}$$

$$\sigma = K_n (\Delta \tilde{u}_n^{[i]} - Dc) = K_n (\Delta \hat{u}_n^{[i]} + \xi\chi - Dc) \tag{5.22}$$

with $\chi = 2 \sin \dfrac{\psi^{[i]}}{2}$ to simplify the notation.

Taking into account the definitions of relative displacements, it is emphasized at this stage that p affects only the tangential component, while c affects only the normal one. In the following paragraphs, the definitions of these two terms will be discussed in detail.

5.2.1 Damage Evolution

The model tracks the development of the damage parameter D, taking into account the interaction between fracture modes I and II.

The parameters η_t and η_n represent the ratios between the initial cracking relative displacements ($\Delta \tilde{u}_t^0$ and $\Delta \tilde{u}_n^0$) and the complete damage relative displacements ($\Delta \tilde{u}_t^f$ and $\Delta \tilde{u}_n^f$):

$$\eta_t = \frac{\Delta \tilde{u}_t^0}{\Delta \tilde{u}_t^f}, \quad \eta_n = \frac{\Delta \tilde{u}_n^0}{\Delta \tilde{u}_n^f} \tag{5.23}$$

and so the mechanical parameter η is defined as it relates to the two modes of fracture:

$$\eta = \frac{1}{\|\boldsymbol{\Delta}\tilde{\mathbf{u}}\|^2}(\Delta\tilde{u}_t^{[i]^2}\eta_t + (<\Delta\tilde{u}_n^{[i]}>_+)^2\eta_n) \tag{5.24}$$

where $\boldsymbol{\Delta}\tilde{\mathbf{u}} = [\Delta\tilde{u}_t^{[i]}, <\Delta\tilde{u}_n^{[i]}>_+]^T$, where the Macaulay brackets $<.>_+$ define the positive part of a number.

The relative displacement ratios are introduced as:

$$Y_t = \frac{\Delta\tilde{u}_t^{[i]}}{\Delta\tilde{u}_t^0}, \quad Y_n = \frac{<\Delta\tilde{u}_n^{[i]}>_+}{\Delta\tilde{u}_n^0} \tag{5.25}$$

and so the equivalent relative displacement ratio is:

$$Y = \sqrt{Y_t^2 + Y_n^2} \tag{5.26}$$

Based on the mechanical parmeters in the Eqs.(5.24)-(5.26), the quantity $\tilde{D}$ can be introduced as follows:

$$\tilde{D} = \frac{Y-1}{Y(1-\eta)} \tag{5.27}$$

The damage parameter D is assumed to be a function of the history of relative displacement:

$$D = \max\{0, \min\{1, \max_{history} \tilde{D}\}\} \tag{5.28}$$

In the softening phase, the shear and normal stresses at the interface are linear functions of the relative displacement. Fig.12 illustrates the mode I and mode II of damage obtained.

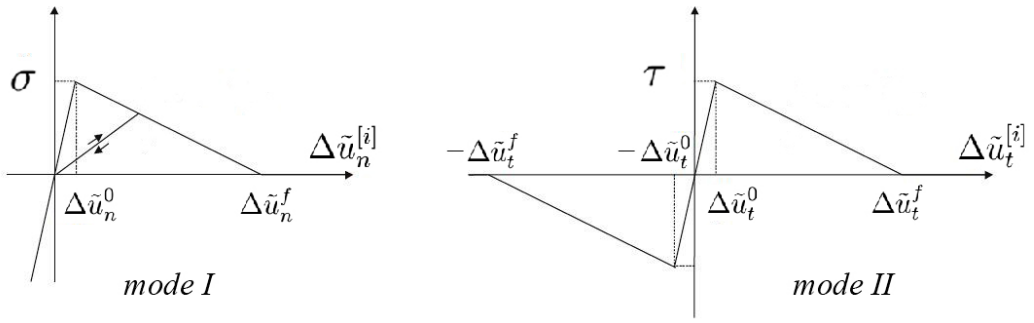

Figure 12: Tangential and normal stress - relative displacement at interface relationship.

5.2.2 Unilateral Contact

The unilateral contact vector $\mathbf{c} = [0, c]^T$ is defined as:

$$\mathbf{c} = \left\{ \begin{array}{c} 0 \\ < \Delta\tilde{u}_n^{[i]} >_+ \end{array} \right\} = \left\{ \begin{array}{c} 0 \\ < \Delta\hat{u}_n^{[i]} + \xi\chi >_+ \end{array} \right\} = \left\{ \begin{array}{c} 0 \\ (\Delta\hat{u}_n^{[i]} + \xi\chi)H \end{array} \right\} \tag{5.29}$$

where the symbol H denotes the Heavised function:

$$H = \max\{0, \mathrm{sign}(\Delta\tilde{u}_n^{[i]})\} \tag{5.30}$$

5.2.3 Friction

The interface is characterized by a unilateral contact response with a frictional effect.

According to the classical Coulomb friction criterion, which is characterized by zero dilatancy, the inelastic relative displacement only has the tangential nonzero component, i.e. the frictional inelastic vector takes the form of $\mathbf{p} = [p, 0]^T$.

Since $\Delta\tilde{u}_t^{[i]}$ remains constant on the interface, the frictional slip p is also assumed to be constant on the damaged part of the interface.

Frictional slip is present only on the damaged part at the characteristic point of the interface. The problem of friction must be expressed in terms of the resultant stresses

on the damaged area, A_d:

$$\begin{aligned} T_d^{[i]} &= \int_\xi D\,\tau_d\,d\xi = \int_\xi DK_t(\Delta\tilde{u}_t^{[i]} - p)\,d\xi \\ &= K_t(\Delta\hat{u}_t^{[i]} - p)D_D \end{aligned} \tag{5.31}$$

$$\begin{aligned} N_d^{[i]} &= \int_\xi D\,\sigma_d\,d\xi = \int_\xi DK_n(\Delta\tilde{u}_n^{[i]} - c)\,d\xi \\ &= \int_\xi DK_n((\Delta\hat{u}_n^{[i]} + \xi\chi) - (<\Delta\hat{u}_n^{[i]} + \xi\chi>_+))\,d\xi \\ &= K_n\left((D_D - D_H)\Delta\hat{u}_n^{[i]} + (D_\xi - D_{\xi H})\chi\right) \end{aligned} \tag{5.32}$$

where the integrals along the interface are defined as follows:

$$D_D = \int_\xi D\,d\xi \tag{5.33}$$

$$D_H = \int_\xi DH\,d\xi \tag{5.34}$$

$$D_\xi = \int_\xi D\xi\,d\xi \tag{5.35}$$

$$D_{\xi H} = \int_\xi D\xi H\,d\xi \tag{5.36}$$

Taking into account that the normal force is constrained to be non-positive, i.e. $N_d^{[i]} \leq 0$, the shear force has to satisfy the yield frictional condition:

$$\Phi = |T_d^{[i]}| + \mu\,N_d^{[i]} \leq 0 \tag{5.37}$$

so that the inelastic relative displacement is governed by the evolution law:

$$\dot{p} = \dot{\lambda}\frac{\partial\Phi}{\partial T_d^{[i]}} \tag{5.38}$$

which, because of equation (5.37), becomes:

$$\dot{p} = \dot{\lambda}\beta \tag{5.39}$$

where λ is the (so-called) plastic multiplier and $\beta = \text{sign}(T_d^{[i]})$. The inelastic evolution is completed by the Kuhn-Tucker (loading-unloading) conditions:

$$\Phi \leq 0 \qquad \dot{\lambda} \geq 0 \qquad \Phi\,\dot{\lambda} = 0 \tag{5.40}$$

6 Numerical procedure

In this section, the numerical procedures for the simulation of the mechanical response of the rigid block models with interfaces introduced in Sections 4 and 5, are illustrated.

This section illustrates the numerical procedures used to implement the problem of large displacements, moderate rotations, and small displacements. A brief description of the elastic interface model with no slip is given in a first paragraph. The numerical procedure for the cohesive interface model with combined damage and friction is then described in detail.

For the solution, the classical iterative Newton-Raphson scheme is adopted by linearizing the involved nonlinear terms with respect to the Lagrangian parameters. Since standard Newton-Raphson methods fail near the limit points, the convergence of the solution is controlled by implementing the arc-length method [18]. In the proposed numerical procedure, a cylindrical arc-length method is used that focuses on a specific displacement parameter and is described in detail at the end of the section.

6.1 Large Displacements

This subsection describes the numerical procedure for the model that includes finite rotations as geometrical nonlinearity. The algorithm for material/contact nonlinearity is outlined in the first paragraph, assuming interfaces are no-tension elastic with no slip.

The following paragraphs discuss the implementation of the cohesive interface model, which combines damage and friction. The derivatives used to calculate the tangent operator in the Newton-Raphson scheme are also reported.

6.1.1 No-tension Elastic Interfaces with No Slip

To determine which part of the interface is in tension and which is in compression, the position of the neutral axis ($\Delta\tilde{u}_n^{[i]} = 0$), denoted as ξ_n, is calculated using the following expression:

$$\xi_n = -\frac{\Delta\hat{u}_n^{[i]}}{2\sin\dfrac{\psi^{[i]}}{2}} \tag{6.1}$$

Next, Algorithm 1 outlines the determination of the two new integration limits, ξ_1 and ξ_2. By substituting the obtained values into Eqs.(5.6)-(5.7), the tangent operator $\mathbf{K}^t$ of Eq.(5.8) can be evaluated.

Algorithm 1: No-tension elastic interface with no slip.

Data: $\hat{\mathbf{s}}^{[i]}$ and L

Evaluate the neutral axis of Eq. (6.1);

Evaluate the normal displacement at the interface extremes, second term of Eq. (4.10):

$a_1 = \Delta\tilde{u}_n^{[i]}|_{-\frac{L}{2}}$

$a_2 = \Delta\tilde{u}_n^{[i]}|_{\frac{L}{2}}$

if $a_1 a_2 < 0$ **then**

  if $a_1 < 0$ **then**

    $\xi_1 = -\dfrac{L}{2}$

    $\xi_2 = \xi_n$

  else

    if $a_1 > 0$

    $\xi_1 = \xi_n$

    $\xi_2 = \dfrac{L}{2}$

  end

else

  if $a_1 < 0$ **then**

    $\xi_1 = -\dfrac{L}{2}$

    $\xi_2 = \dfrac{L}{2}$

  else

    if $a_1 > 0$

    $\xi_1 = 0$

    $\xi_2 = 0$

  end

end

6.1.2 Damage Evolution

This subsection describes the procedure for implementing the interface cohesive model in the theory of combining damage and friction.

The first step is to study the evolution of damage. The damage parameter is determined by the Eqs.(5.23)-(5.28). The partial derivatives of the parameter D are computed as:

$$\frac{\partial D}{\partial *} = \frac{\partial D}{\partial Y}\frac{\partial Y}{\partial *} + \frac{\partial D}{\partial \eta}\frac{\partial \eta}{\partial *} \tag{6.2}$$

$$\frac{\partial D}{\partial Y} = \frac{1}{Y^2(1-\eta)} \quad \frac{\partial D}{\partial \eta} = \frac{(Y-1)}{Y(1-\eta)^2} \tag{6.3}$$

Explicitly, the partial derivatives with respect to $\Delta\hat{u}_t^{[i]}$ are:

$$\frac{\partial Y}{\partial \Delta\hat{u}_t^{[i]}} = \frac{\partial Y}{\partial \Delta\tilde{u}_t^{[i]}}\frac{\partial \Delta\tilde{u}_t^{[i]}}{\partial \Delta\hat{u}_t^{[i]}} = \frac{\Delta\tilde{u}_t^{[i]}}{Y(\Delta\tilde{u}_t^0)^2} \tag{6.4}$$

$$\frac{\partial \eta}{\partial \Delta\hat{u}_t^{[i]}} = \frac{\partial \eta}{\partial \Delta\tilde{u}_t^{[i]}}\frac{\partial \Delta\tilde{u}_t^{[i]}}{\partial \Delta\hat{u}_t^{[i]}} = \frac{2\Delta\tilde{u}_t^{[i]}(<\Delta\tilde{u}_n^{[i]}>_+)^2(\eta_t-\eta_n)}{\|\boldsymbol{\Delta}\tilde{\mathbf{u}}\|^4} \tag{6.5}$$

where it is easy to notice that $\dfrac{\partial \Delta\tilde{u}_t^{[i]}}{\partial \Delta\hat{u}_t^{[i]}} = 1$.
From the definition of $<\Delta\tilde{u}_n^{[i]}>_+ = <\Delta\hat{u}_n^{[i]} + \xi\chi>_+$, it is possible to define the partial derivatives with respect to $\Delta\hat{u}_n^{[i]}$:

$$\frac{\partial Y}{\partial \Delta\hat{u}_n^{[i]}} = \frac{\partial Y}{\partial \Delta\tilde{u}_n^{[i]}}\frac{\partial \Delta\tilde{u}_n^{[i]}}{\partial \Delta\hat{u}_n^{[i]}} = \frac{\Delta\tilde{u}_n^{[i]}}{Y(\Delta\tilde{u}_n^0)^2} \tag{6.6}$$

$$\frac{\partial \eta}{\partial \Delta\hat{u}_n^{[i]}} = \frac{\partial \eta}{\partial \Delta\tilde{u}_n^{[i]}}\frac{\partial \Delta\tilde{u}_n^{[i]}}{\partial \Delta\hat{u}_n^{[i]}} = \frac{2<\Delta\tilde{u}_n^{[i]}>_+ \Delta\tilde{u}_t^{[i]^2}(\eta_n-\eta_t)}{\|\boldsymbol{\Delta}\tilde{\mathbf{u}}\|^4} \tag{6.7}$$

Finally, the partial derivatives with respect to χ that depends on $\psi^{[i]}$:

$$\frac{\partial Y}{\partial \chi} = \frac{\partial Y}{\partial \Delta\tilde{u}_n^{[i]}}\frac{\partial \Delta\tilde{u}_n^{[i]}}{\partial \chi} = \frac{<\Delta\tilde{u}_n^{[i]}>_+}{Y(\Delta\tilde{u}_n^0)^2} \tag{6.8}$$

$$\frac{\partial \eta}{\partial \chi} = \frac{\partial \eta}{\partial \Delta \tilde{u}_n^{[i]}} \frac{\partial \Delta \tilde{u}_n^{[i]}}{\partial \chi} = \frac{2 < \Delta \tilde{u}_n^{[i]} >_+ \Delta \tilde{u}_t^{[i]^2} (\eta_n - \eta_t)}{\|\boldsymbol{\Delta}\tilde{\mathbf{u}}\|^4} \tag{6.9}$$

6.1.3 Interface friction

Friction is activated only when the damage integral along the interface, D_D, is greater than 0:

$$D_D = \int_\xi D \, d\xi > 0 \tag{6.10}$$

This means that there is damage greater than 0 at least at one point. All integrals of the proposed procedure have to be computed numerically. To this end, the interface is divided into m subdomains and a Gauss-Legendre quadrature is performed in each subdomain.

The evolution of the inelastic relative displacement is solved adopting a backward-Euler time step procedure within the predictor-corrector algorithm to solve the nonlinear step evolution equation. Thus, the time is discretized in steps and the quantities at the previous time step, $t = t_n$, are denoted with the index $_n$, while the quantities at the actual time step have no subscript. The time step is given by:

$$\Delta t = t - t_n \tag{6.11}$$

where t is the actual time and t_n is the previous time.

Given $\Delta \tilde{u}_t^{[i]}$ and $\Delta \tilde{u}_n^{[i]}$ at the previous time step, the discretized form of the evolution equation (5.39) is:

$$\Delta p = p - p_n = \beta \Delta \lambda \tag{6.12}$$

The interface model is solved using a displacement-based formulation and a predictor-corrector algorithm at a typical Gauss point of the interface's subdomain. The time step solution involves two main steps: the predictor and the corrector. The predictor makes an initial estimate of the solution based on the current available information, while the corrector refines this estimate using additional information to obtain a more

accurate solution. These two steps are described below.

- **predictor**

$$p = p_n \quad (\Delta\lambda = 0) \tag{6.13}$$

$$T_d^{[tr]} = \int_\xi DK_t(\Delta\hat{u}_t^{[i]} - p_n)\, d\xi \tag{6.14}$$

$$\Phi^{[tr]} = \beta\, T_d^{[tr]} + \mu\, < N_d^{[i]} >_- \tag{6.15}$$

$$\beta = \text{sign}(T_d^{[tr]})$$

If $\Phi^{[tr]} < 0$ then $\Delta p = 0$, otherwise, let us proceed to the second step of the algorithm.

- **corrector**

During the loading phase, the plastic multiplier increment is computed enforcing that the actual value of the yield function is equal to zero:

$$\begin{aligned}
\Phi &= \beta \int_\xi DK_t(\Delta\hat{u}_t^{[i]} - p_n - \Delta p)\, d\xi + \mu \int_\xi DK_n(\Delta\tilde{u}_n^{[i]} - < \Delta\tilde{u}_n^{[i]} >_+)\, d\xi \\
&= \int_\xi D\left(\beta K_t(\Delta\hat{u}_t^{[i]} - p_n - \beta\Delta\lambda) + \mu K_n(\Delta\tilde{u}_n^{[i]} - < \Delta\tilde{u}_n^{[i]} >_+)\right) d\xi \\
&= \beta K_t(\Delta\hat{u}_t^{[i]} - p_n - \beta\Delta\lambda) \int_\xi D\, d\xi + \mu K_n \int_\xi D(\Delta\hat{u}_n^{[i]} + \xi\chi - < \Delta\hat{u}_n^{[i]} + \xi\chi >_+)\, d\xi \\
&= \beta K_t(\Delta\hat{u}_t^{[i]} - p_n - \beta\Delta\lambda) D_D + \mu K_n \left((D_D - D_H)\Delta\hat{u}_n^{[i]} + (D_\xi - D_{\xi H})\chi\right) \\
&= 0
\end{aligned} \tag{6.16}$$

By solving the Eq.(6.16), considering the Eqs.(6.12)-(6.14), it is possible to evaluate $\Delta\lambda$ and, hence, Δp and the actual value of the inelastic slip p. In particular:

$$\Delta\lambda = \frac{\beta K_t(\Delta\hat{u}_t^{[i]} - p_n) D_D + \mu K_n \left((D_D - D_H)\Delta\hat{u}_n^{[i]} + (D_\xi - D_{\xi H})\chi\right)}{K_t D_D} \geq 0 \tag{6.17}$$

Algorithm 2 outlines the numerical procedure for the time step solution predictor-corrector.

The partial derivatives of the frictional slip p with respect to the Lagrangian parameters at the middle-point of the interface and to the curvature are evaluated.

If $\Delta\hat{u}_n^{[i]} + \xi\chi > 0$,

$$\Delta\lambda = \beta\Delta\hat{u}_t^{[i]} \tag{6.18}$$

$$\Delta p = \beta\Delta\lambda = \beta^2\Delta\hat{u}_t^{[i]} = \Delta\hat{u}_t^{[i]} \tag{6.19}$$

and the partial derivatives are equal to:

$$\frac{\partial p}{\partial\Delta\hat{u}_t^{[i]}} = \frac{\partial\Delta p}{\partial\Delta\hat{u}_t^{[i]}} = \beta\frac{\partial\Delta\lambda}{\partial\Delta\hat{u}_t^{[i]}} = 1 \tag{6.20}$$

$$\frac{\partial p}{\partial\Delta\hat{u}_n^{[i]}} = \frac{\partial\Delta p}{\partial\Delta\hat{u}_n^{[i]}} = \beta\frac{\partial\Delta\lambda}{\partial\Delta\hat{u}_n^{[i]}} = 0 \tag{6.21}$$

$$\frac{\partial p}{\partial\chi} = \frac{\partial\Delta p}{\partial\chi} = \beta\frac{\partial\Delta\lambda}{\partial\chi} = 0 \tag{6.22}$$

Otherwise if $\Delta\hat{u}_n^{[i]} + \xi\chi \leq 0$, the partial derivatives become:

$$\begin{aligned}
&\frac{\partial p}{\partial\Delta\hat{u}_t^{[i]}} = \frac{\partial\Delta p}{\partial\Delta\hat{u}_t^{[i]}} = \beta\frac{\partial\Delta\lambda}{\partial\Delta\hat{u}_t^{[i]}} = 1 \\
&\frac{\partial p}{\partial\Delta\hat{u}_n^{[i]}} = \frac{\partial\Delta p}{\partial\Delta\hat{u}_n^{[i]}} = \beta\frac{\partial\Delta\lambda}{\partial\Delta\hat{u}_n^{[i]}} = \frac{\beta(K_n\mu(D_D - D_H))}{K_t D_D} \\
&\frac{\partial p}{\partial\chi} = \frac{\partial\Delta p}{\partial\chi} = \beta\frac{\partial\Delta\lambda}{\partial\chi} = \frac{\beta(K_n\mu(D_\xi - D_{\xi H}))}{K_t D_D}
\end{aligned} \tag{6.23}$$

Algorithm 2: Time step solution predictor-corrector.

Data: $\Delta\tilde{u}_t^{[i]}$, $\Delta\tilde{u}_n^{[i]}$, Δt, Δp

predictor

Evaluate the predictor frictional slip of Eq. (6.13);

Evaluate the trial shear force of Eq. (6.14) and the trial activation function of Eq. (6.15)

if $\Phi^{[tr]} < 0$ **then**

  $\Delta\lambda = 0$

  $p = p_n$

else

  corrector

  $\Phi = 0$ Eq. (6.16)

  Evaluate $\Delta\lambda$ of Eq.(6.17)

  Evaluate Δp of Eq.(6.12)

end

6.1.4 Interface Cohesive Model combining Damage and Friction

The integration algorithm requires the evaluation of the consistent tangent operator of the relationship between $\hat{\mathbf{S}}^{[i]}$ and $\hat{\mathbf{s}}^{[i]}$, obtained as follows:

$$\mathbf{K}^t = \frac{\partial \hat{\mathbf{S}}^{[i]}}{\partial \hat{\mathbf{s}}^{[i]}} = \begin{bmatrix} \dfrac{\partial T^{[i]}}{\partial \Delta \hat{u}_t^{[i]}} & \dfrac{\partial T^{[i]}}{\partial \Delta \hat{u}_n^{[i]}} & \dfrac{\partial T^{[i]}}{\partial \psi^{[i]}} \\ \dfrac{\partial N^{[i]}}{\partial \Delta \hat{u}_t^{[i]}} & \dfrac{\partial N^{[i]}}{\partial \Delta \hat{u}_n^{[i]}} & \dfrac{\partial N^{[i]}}{\partial \psi^{[i]}} \\ \dfrac{\partial M^{[i]}}{\partial \Delta \hat{u}_t^{[i]}} & \dfrac{\partial M^{[i]}}{\partial \Delta \hat{u}_n^{[i]}} & \dfrac{\partial M^{[i]}}{\partial \psi^{[i]}} \end{bmatrix} \tag{6.24}$$

where $T^{[i]}$, $N^{[i]}$ and $M^{[i]}$ represent the local stress components on the total area of interface, $A^{[i]}$, as follows:

$$\hat{\mathbf{S}}^{[i]} = \begin{Bmatrix} T^{[i]} \\ N^{[i]} \\ M^{[i]} \end{Bmatrix} = \int_\xi \begin{Bmatrix} \tau \\ \sigma \\ \xi\sigma \end{Bmatrix} d\xi \tag{6.25}$$

By substituting Eqs.(5.21)-(5.22) into Eq.(6.25), let us obtain in components:

$$\begin{aligned} T^{[i]} &= \int_\xi K_t(\Delta \hat{u}_t^{[i]} - Dp)\, d\xi = K_t \left(A^{[i]} \Delta \hat{u}_t^{[i]} - p \int_\xi D\, d\xi \right) \\ &= K_t \left(A^{[i]} \Delta \hat{u}_t^{[i]} - p D_D \right) \end{aligned} \tag{6.26}$$

$$\begin{aligned} N^{[i]} &= \int_{\xi} K_n(\Delta\hat{u}_n^{[i]} + \xi\chi - D < \Delta\hat{u}_n^{[i]} + \xi\chi >_+) \, d\xi \\ &= K_n \left(A^{[i]}\Delta\hat{u}_n^{[i]} - \int_{\xi} D < \Delta\hat{u}_n^{[i]} + \xi\chi >_+ \, d\xi \right) \\ &= K_n \left(A^{[i]}\Delta\hat{u}_n^{[i]} - D_H\Delta\hat{u}_n^{[i]} - D_{\xi H}\chi \right) \end{aligned} \tag{6.27}$$

$$\begin{aligned} M^{[i]} &= \int_{\xi} \xi K_n(\Delta\hat{u}_n^{[i]} + \xi\chi - D < \Delta\hat{u}_n^{[i]} + \xi\chi >_+) \, d\xi \\ &= K_n \left(J^{[i]}\chi - \int_{\xi} \xi D < \Delta\hat{u}_n^{[i]} + \xi\chi >_+ \, d\xi \right) \\ &= K_n \left(J^{[i]}\chi - D_{\xi H}\Delta\hat{u}_n^{[i]} - D_{\xi 2H}\chi \right) \end{aligned} \tag{6.28}$$

where the integrals along the interface are defined in Eqs.(5.28)-(5.36). A new integral along the interface is also defined as follows:

$$D_{\xi 2H} = \int_{\xi} D\xi^2 H \, d\xi \tag{6.29}$$

Then, differentiating with respect to the Lagrangian parameters at the midpoint of the interface, one obtains:

$$\frac{\partial *}{\partial \psi^{[i]}} = \frac{\partial *}{\partial \chi}\frac{\partial \chi}{\partial \psi^{[i]}} = \frac{\partial *}{\partial \chi}\cos\frac{\psi^{[i]}}{2}$$

$$\begin{aligned}\frac{\partial T^{[i]}}{\partial \Delta \hat{u}_t^{[i]}} &= K_t \left(A^{[i]} - \frac{\partial}{\partial \Delta \hat{u}_t^{[i]}} p \int_\xi D \, d\xi \right) \\ &= K_t \left(A^{[i]} - \frac{\partial p}{\partial \Delta \hat{u}_t^{[i]}} \int_\xi D \, d\xi - p \int_\xi \frac{\partial D}{\partial \Delta \hat{u}_t^{[i]}} \, d\xi \right) \\ &= K_t \left(A^{[i]} - \frac{\partial p}{\partial \Delta \hat{u}_t^{[i]}} D_D - p \frac{\partial D_D}{\partial \Delta \hat{u}_t^{[i]}} \right) \end{aligned} \tag{6.30}$$

$$\begin{aligned}\frac{\partial T^{[i]}}{\partial \Delta \hat{u}_n^{[i]}} &= K_t \left(-\frac{\partial}{\partial \Delta \hat{u}_n^{[i]}} p \int_\xi D \, d\xi \right) \\ &= K_t \left(-\frac{\partial p}{\partial \Delta \hat{u}_n^{[i]}} \int_\xi D \, d\xi - p \int_\xi \frac{\partial D}{\partial \Delta \hat{u}_n^{[i]}} \, d\xi \right) \\ &= K_t \left(-\frac{\partial p}{\partial \Delta \hat{u}_n^{[i]}} D_D - p \frac{\partial D_D}{\partial \Delta \hat{u}_n^{[i]}} \right) \end{aligned} \tag{6.31}$$

$$\begin{aligned}\frac{\partial T^{[i]}}{\partial \psi^{[i]}} &= K_t \left(-\frac{\partial}{\partial \chi} p \int_\xi D \, d\xi \right) \cos \frac{\psi^{[i]}}{2} \\ &= K_t \left(-\frac{\partial p}{\partial \chi} \int_\xi D \, d\xi - p \int_\xi \frac{\partial D}{\partial \chi} \, d\xi \right) \cos \frac{\psi^{[i]}}{2} \\ &= K_t \left(-\frac{\partial p}{\partial \chi} D_D - p \frac{\partial D_D}{\partial \chi} \right) \cos \frac{\psi^{[i]}}{2} \end{aligned} \tag{6.32}$$

$$\begin{aligned}\frac{\partial N^{[i]}}{\partial \Delta \hat{u}_t^{[i]}} &= K_n \left(-\frac{\partial}{\partial \Delta \hat{u}_t^{[i]}} \int_\xi D < \Delta \hat{u}_n^{[i]} + \xi \chi >_+ \, d\xi \right) \\ &= K_n \left(-\int_\xi \frac{\partial D}{\partial \Delta \hat{u}_t^{[i]}} < \Delta \hat{u}_n^{[i]} + \xi \chi >_+ \, d\xi - \int_\xi D \frac{\partial (< \Delta \hat{u}_n^{[i]} + \xi \chi >_+)}{\partial \Delta \hat{u}_t^{[i]}} \, d\xi \right) \\ &= K_n \left(-\Delta \hat{u}_n^{[i]} \frac{\partial D_H}{\partial \Delta \hat{u}_t^{[i]}} - \chi \frac{\partial D_{\xi H}}{\partial \Delta \hat{u}_t^{[i]}} \right) \end{aligned} \tag{6.33}$$

$$\begin{aligned}
\frac{\partial N^{[i]}}{\partial \Delta \hat{u}_n^{[i]}} &= K_n \left(A^{[i]} - \frac{\partial}{\partial \Delta \hat{u}_n^{[i]}} \int_\xi D < \Delta \hat{u}_n^{[i]} + \xi \chi >_+ \, d\xi \right) \\
&= K_n \left(A^{[i]} - \int_\xi \frac{\partial D}{\partial \Delta \hat{u}_n^{[i]}} < \Delta \hat{u}_n^{[i]} + \xi \chi >_+ \, d\xi - \int_\xi D \frac{\partial (< \Delta \hat{u}_n^{[i]} + \xi \chi >_+)}{\partial \Delta \hat{u}_n^{[i]}} \, d\xi \right) \\
&= K_n \left(A^{[i]} - \Delta \hat{u}_n^{[i]} \frac{\partial D_H}{\partial \Delta \hat{u}_n^{[i]}} - \chi \frac{\partial D_{\xi H}}{\partial \Delta \hat{u}_n^{[i]}} - D_H \right) \qquad (6.34)
\end{aligned}$$

$$\begin{aligned}
\frac{\partial N^{[i]}}{\partial \psi^{[i]}} &= K_n \left(-\frac{\partial}{\partial \chi} \int_\xi D < \Delta \hat{u}_n^{[i]} + \xi \chi >_+ \, d\xi \right) \cos \frac{\psi^{[i]}}{2} \\
&= K_n \left(- \int_\xi \frac{\partial D}{\partial \chi} < \Delta \hat{u}_n^{[i]} + \xi \chi >_+ \, d\xi - \int_\xi D \frac{\partial (< \Delta \hat{u}_n^{[i]} + \xi \chi >_+)}{\partial \chi} \, d\xi \right) \cos \frac{\psi^{[i]}}{2} \\
&= K_n \left(-\Delta \hat{u}_n^{[i]} \frac{\partial D_H}{\partial \chi} - \chi \frac{\partial D_{\xi H}}{\partial \chi} - D_{\xi H} \right) \cos \frac{\psi^{[i]}}{2} \qquad (6.35)
\end{aligned}$$

$$\begin{aligned}
\frac{\partial M^{[i]}}{\partial \Delta \hat{u}_t^{[i]}} &= K_n \left(-\frac{\partial}{\partial \Delta \hat{u}_t^{[i]}} \int_\xi \xi D < \Delta \hat{u}_n^{[i]} + \xi \chi >_+ \, d\xi \right) \\
&= K_n \left(- \int_\xi \xi \frac{\partial D}{\partial \Delta \hat{u}_t^{[i]}} < \Delta \hat{u}_n^{[i]} + \xi \chi >_+ \, d\xi - \int_\xi \xi D \frac{\partial (< \Delta \hat{u}_n^{[i]} + \xi \chi >_+)}{\partial \Delta \hat{u}_t^{[i]}} \, d\xi \right) \\
&= K_n \left(-\Delta \hat{u}_n^{[i]} \frac{\partial D_{\xi H}}{\partial \Delta \hat{u}_t^{[i]}} - \chi \frac{\partial D_{\xi 2H}}{\partial \Delta \hat{u}_t^{[i]}} \right) \qquad (6.36)
\end{aligned}$$

$$\begin{aligned}
\frac{\partial M^{[i]}}{\partial \Delta \hat{u}_n^{[i]}} &= K_n \left(-\frac{\partial}{\partial \Delta \hat{u}_n^{[i]}} \int_\xi \xi D < \Delta \hat{u}_n^{[i]} + \xi \chi >_+ \, d\xi \right) \\
&= K_n \left(- \int_\xi \xi \frac{\partial D}{\partial \Delta \hat{u}_n^{[i]}} < \Delta \hat{u}_n^{[i]} + \xi \chi >_+ \, d\xi - \int_\xi \xi D \frac{\partial (< \Delta \hat{u}_n^{[i]} + \xi \chi >_+)}{\partial \Delta \hat{u}_n^{[i]}} \, d\xi \right) \\
&= K_n \left(-\Delta \hat{u}_n^{[i]} \frac{\partial D_{\xi H}}{\partial \Delta \hat{u}_n^{[i]}} - \chi \frac{\partial D_{\xi 2H}}{\partial \Delta \hat{u}_n^{[i]}} - D_{\xi H} \right) \qquad (6.37)
\end{aligned}$$

$$\begin{aligned}
\frac{\partial M^{[i]}}{\partial \psi^{[i]}} &= K_n \left(J^{[i]} \frac{\partial \chi}{\partial \chi} - \frac{\partial}{\partial \chi} \int_{\xi} \xi D < \Delta \hat{u}_n^{[i]} + \xi \chi >_+ \, d\xi \right) \cos \frac{\psi^{[i]}}{2} \\
&= K_n \left(J^{[i]} - \int_{\xi} \xi \frac{\partial D}{\partial \chi} < \Delta \hat{u}_n^{[i]} + \xi \chi >_+ \, d\xi - \int_{\xi} \xi D \frac{\partial (< \Delta \hat{u}_n^{[i]} + \xi \chi >_+)}{\partial \chi} \, d\xi \right) \cos \frac{\psi^{[i]}}{2} \\
&= K_n \left(J^{[i]} - \Delta \hat{u}_n^{[i]} \frac{\partial D_{\xi H}}{\partial \chi} - \chi \frac{\partial D_{\xi 2H}}{\partial \chi} - D_{\xi 2H} \right) \cos \frac{\psi^{[i]}}{2} \qquad (6.38)
\end{aligned}$$

where the partial derivatives of D and p with respect to Lagrangian parameters are defined respectively in the Eqs.(6.2)-(6.9) and (6.20)-(6.23).

The numerical procedure for reproducing the mechanical response of rigid blocks with the interface model introduced earlier is presented globally in Algorithm 3. By substituting the constitutive tangent matrix $\mathbf{K}^t$ in Eq.(4.42), it is possible to evaluate the material stiffness ${\mathbf{K}_m}^{[i]}$.

Algorithm 3: Numerical procedure for rigid blocks with interface cohesive model combining damage and friction.

- Divide the length of the interface into m subdomains
- Execute the loop over the subdomains
  Define the Gauss points within the subdomain
  - Perform the loop over the Gauss points
    Evaluate $\Delta\tilde{u}_t^{[i]}$ and $\Delta\tilde{u}_n^{[i]}$ of Eq.(4.10)
    - Evaluate the damage parameter D by the Eqs.(5.23)-(5.28)
    - Evaluate the Heaviside function H of the Eq.(5.30)
    - Evaluate $\dfrac{\partial D}{\partial \Delta\hat{u}_t^{[i]}}$, $\dfrac{\partial D}{\partial \Delta\hat{u}_n^{[i]}}$, $\dfrac{\partial D}{\partial \chi}$ considering the Eqs.(6.2)-(6.9)
    - Evaluate the integral along the interface D_D of the Eq.(5.33)
    - Evaluate the integrals along the interface of the Eqs.(5.34)-(5.36)-(6.29)

    End the loop over the Gauss points

  End the loop over the subdomains
- If $D_D > 0$, perform the friction problem (see Algorithm 2)
  Evaluate the frictional inelastic vector $\mathbf{p}$
  Evaluate $\dfrac{\partial p}{\partial \Delta\hat{u}_t^{[i]}}, \dfrac{\partial p}{\partial \Delta\hat{u}_n^{[i]}}, \dfrac{\partial p}{\partial \chi}$ considering the Eqs.(6.20)-(6.23)
- Evaluate the internal forces $\hat{\mathbf{S}}^{[i]}$
- Evaluate the constitutive tangent matrix $\mathbf{K}^t$ of Eq.(6.24)
- Evaluate the material stiffness matrix ${\mathbf{K}_m}^{[i]}$ of Eq.(4.42)

6.2 Moderate Rotations

This section describes the numerical procedure for the cohesive interface model, which combines damage and friction in the context of moderate rotation theory.

The partial derivatives of the parameter D are computed according to the scheme given by Eq.(6.2). Specifically, the partial derivatives with respect to $\Delta\hat{u}_t^{[i]}$ and $\Delta\hat{u}_n^{[i]}$ remain unchanged, while the derivatives with respect to $\psi^{[i]}$ are expressed as follows:

$$\frac{\partial Y}{\partial \psi^{[i]}} = \frac{< \Delta\tilde{u}_n^{[i]} >_+}{Y(\Delta\tilde{u}_n^0)^2}\xi\left(1 - \frac{{\psi^{[i]}}^2}{2}\right) \tag{6.39}$$

$$\frac{\partial \eta}{\partial \psi^{[i]}} = \frac{2 < \Delta\tilde{u}_n^{[i]} >_+ {\Delta\tilde{u}_t^{[i]}}^2(\eta_n - \eta_t)}{\|\boldsymbol{\Delta}\tilde{\mathbf{u}}\|^4}\xi\left(1 - \frac{{\psi^{[i]}}^2}{2}\right) \tag{6.40}$$

The formulation of the friction problem has to be expressed in terms of resultant stresses on the damaged area, A_d. While $T_d^{[i]}$ is evaluate as in the Eq.(5.31), $N_d^{[i]}$ becomes:

$$N_d^{[i]} = K_n\left((D_D - D_H)\Delta\hat{u}_n^{[i]} + (D_\xi - D_{\xi H})\psi^{[i]}\right) \tag{6.41}$$

where the integrals along the interface are defined in the Eqs. (5.34)-(5.36).

The local stress components acting on the total area of interface, $\hat{\mathbf{S}}^{[i]} = [T^{[i]}, N^{[i]}, M^{[i]}]^T$, become:

$$T^{[i]} = K_t\left(A^{[i]}\Delta\hat{u}_t^{[i]} - pD_D\right) \tag{6.42}$$

$$N^{[i]} = K_n\left(A^{[i]}\Delta\hat{u}_n^{[i]} - D_H\Delta\hat{u}_n^{[i]} - D_{\xi H}\psi^{[i]}\right) \tag{6.43}$$

$$M^{[i]} = K_n \left(J^{[i]} \psi^{[i]} - D_{\xi H} \Delta \hat{u}_n^{[i]} - D_{\xi 2H} \psi^{[i]} \right) \tag{6.44}$$

The constitutive tangent matrix components are obtained by differentiating with respect to the Lagrangian parameters at the midpoint of the interface, as follows:

$$\frac{\partial T^{[i]}}{\partial \Delta \hat{u}_t^{[i]}} = K_t \left(A^{[i]} - \frac{\partial p}{\partial \Delta \hat{u}_t^{[i]}} D_D - p \frac{\partial D_D}{\partial \Delta \hat{u}_t^{[i]}} \right) \tag{6.45}$$

$$\frac{\partial T^{[i]}}{\partial \Delta \hat{u}_n^{[i]}} = K_t \left(- \frac{\partial p}{\partial \Delta \hat{u}_n^{[i]}} D_D - p \frac{\partial D_D}{\partial \Delta \hat{u}_n^{[i]}} \right) \tag{6.46}$$

$$\frac{\partial T^{[i]}}{\partial \psi^{[i]}} = K_t \left(- \frac{\partial p}{\partial \psi^{[i]}} D_D - p \frac{\partial D_D}{\partial \psi^{[i]}} \right) \tag{6.47}$$

$$\frac{\partial N^{[i]}}{\partial \Delta \hat{u}_t^{[i]}} = K_n \left(- \Delta \hat{u}_n^{[i]} \frac{\partial D_H}{\partial \Delta \hat{u}_t^{[i]}} - \psi^{[i]} \frac{\partial D_{\xi H}}{\partial \Delta \hat{u}_t^{[i]}} \right) \tag{6.48}$$

$$\frac{\partial N^{[i]}}{\partial \Delta \hat{u}_n^{[i]}} = K_n \left(A^{[i]} - \Delta \hat{u}_n^{[i]} \frac{\partial D_H}{\partial \Delta \hat{u}_n^{[i]}} - \psi^{[i]} \frac{\partial D_{\xi H}}{\partial \Delta \hat{u}_n^{[i]}} - D_H \right) \tag{6.49}$$

$$\frac{\partial N^{[i]}}{\partial \psi^{[i]}} = K_n \left(- \Delta \hat{u}_n^{[i]} \frac{\partial D_H}{\partial \psi^{[i]}} - \psi^{[i]} \frac{\partial D_{\xi H}}{\partial \psi^{[i]}} - D_{\xi H} \right) \tag{6.50}$$

$$\frac{\partial M^{[i]}}{\partial \Delta \hat{u}_t^{[i]}} = K_n \left(-\Delta \hat{u}_n^{[i]} \frac{\partial D_{\xi H}}{\partial \Delta \hat{u}_t^{[i]}} - \psi^{[i]} \frac{\partial D_{\xi 2H}}{\partial \Delta \hat{u}_t^{[i]}} \right) \tag{6.51}$$

$$\frac{\partial M^{[i]}}{\partial \Delta \hat{u}_n^{[i]}} = K_n \left(-\Delta \hat{u}_n^{[i]} \frac{\partial D_{\xi H}}{\partial \Delta \hat{u}_n^{[i]}} - \psi^{[i]} \frac{\partial D_{\xi 2H}}{\partial \Delta \hat{u}_n^{[i]}} - D_{\xi H} \right) \tag{6.52}$$

$$\frac{\partial M^{[i]}}{\partial \psi^{[i]}} = K_n \left(J^{[i]} - \Delta \hat{u}_n^{[i]} \frac{\partial D_{\xi H}}{\partial \psi^{[i]}} - \psi^{[i]} \frac{\partial D_{\xi 2H}}{\partial \psi^{[i]}} - D_{\xi 2H} \right) \tag{6.53}$$

By substituting the constitutive tangent matrix $\mathbf{K}_t$ of Eq.(6.24) into Eq.(4.42), it is possible to evaluate the material stiffness ${\mathbf{K}_m}^{[i]}$ (see Algorithm 3).

6.3 Small Displacements

This section describes the numerical procedure for the cohesive interface model, which combines damage and friction in the context of small displacements.

The partial derivatives of the parameter D are computed using the scheme given by Equation (6.2). Specifically, the partial derivatives with respect to $\Delta\hat{u}_t^{[i]}$ and $\Delta\hat{u}_n^{[i]}$ remain unchanged, while the derivatives with respect to $\psi^{[i]}$ are expressed as follows:

$$\frac{\partial Y}{\partial \psi^{[i]}} = \frac{< \Delta\tilde{u}_n^{[i]} >_+}{Y(\Delta\tilde{u}_n^0)^2}\xi \tag{6.54}$$

$$\frac{\partial \eta}{\partial \psi^{[i]}} = \frac{2 < \Delta\tilde{u}_n^{[i]} >_+ {\Delta\tilde{u}_t^{[i]}}^2(\eta_n - \eta_t)}{\|\boldsymbol{\Delta}\tilde{\mathbf{u}}\|^4}\xi \tag{6.55}$$

The formulation of the friction problem has to be expressed in terms of resultant stresses on the damaged area, A_d. While $T_d^{[i]}$ is evaluate as in the Eq. (5.31), $N_d^{[i]}$ becomes:

$$N_d^{[i]} = K_n\left((D_D - D_H)\Delta\hat{u}_n^{[i]} + (D_\xi - D_{\xi H})\psi^{[i]}\right) \tag{6.56}$$

where the integrals along the interface are defined in the Eqs. (5.34)-(5.36).

In the linear theory, the local stress acting on the total area of interface, $\hat{\mathbf{S}}^{[i]} = [T^{[i]}, N^{[i]}, M^{[i]}]^T$, become:

$$T^{[i]} = K_t\left(A^{[i]}\Delta\hat{u}_t^{[i]} - pD_D\right) \tag{6.57}$$

$$N^{[i]} = K_n\left(A^{[i]}\Delta\hat{u}_n^{[i]} - D_H\Delta\hat{u}_n^{[i]} - D_{\xi H}\psi^{[i]}\right) \tag{6.58}$$

$$M^{[i]} = K_n \left(J^{[i]} \psi^{[i]} - D_{\xi H} \Delta \hat{u}_n^{[i]} - D_{\xi 2H} \psi^{[i]} \right) \tag{6.59}$$

Then, differentiating with respect to the Lagrangian parameters at the midpoint of the interface, one obtains:

$$\frac{\partial T^{[i]}}{\partial \Delta \hat{u}_t^{[i]}} = K_t \left(A^{[i]} - \frac{\partial p}{\partial \Delta \hat{u}_t^{[i]}} D_D - p \frac{\partial D_D}{\partial \Delta \hat{u}_t^{[i]}} \right) \tag{6.60}$$

$$\frac{\partial T^{[i]}}{\partial \Delta \hat{u}_n^{[i]}} = K_t \left(- \frac{\partial p}{\partial \Delta \hat{u}_n^{[i]}} D_D - p \frac{\partial D_D}{\partial \Delta \hat{u}_n^{[i]}} \right) \tag{6.61}$$

$$\frac{\partial T^{[i]}}{\partial \psi^{[i]}} = K_t \left(- \frac{\partial p}{\partial \psi^{[i]}} D_D - p \frac{\partial D_D}{\partial \psi^{[i]}} \right) \tag{6.62}$$

$$\frac{\partial N^{[i]}}{\partial \Delta \hat{u}_t^{[i]}} = K_n \left(- \Delta \hat{u}_n^{[i]} \frac{\partial D_H}{\partial \Delta \hat{u}_t^{[i]}} - \psi^{[i]} \frac{\partial D_{\xi H}}{\partial \Delta \hat{u}_t^{[i]}} \right) \tag{6.63}$$

$$\frac{\partial N^{[i]}}{\partial \Delta \hat{u}_n^{[i]}} = K_n \left(A^{[i]} - \Delta \hat{u}_n^{[i]} \frac{\partial D_H}{\partial \Delta \hat{u}_n^{[i]}} - \psi^{[i]} \frac{\partial D_{\xi H}}{\partial \Delta \hat{u}_n^{[i]}} - D_H \right) \tag{6.64}$$

$$\frac{\partial N^{[i]}}{\partial \psi^{[i]}} = K_n \left(- \Delta \hat{u}_n^{[i]} \frac{\partial D_H}{\partial \psi^{[i]}} - \psi^{[i]} \frac{\partial D_{\xi H}}{\partial \psi^{[i]}} - D_{\xi H} \right) \tag{6.65}$$

$$\frac{\partial M^{[i]}}{\partial \Delta \hat{u}_t^{[i]}} = K_n \left(-\Delta \hat{u}_n^{[i]} \frac{\partial D_{\xi H}}{\partial \Delta \hat{u}_t^{[i]}} - \psi^{[i]} \frac{\partial D_{\xi 2H}}{\partial \Delta \hat{u}_t^{[i]}} \right) \tag{6.66}$$

$$\frac{\partial M^{[i]}}{\partial \Delta \hat{u}_n^{[i]}} = K_n \left(-\Delta \hat{u}_n^{[i]} \frac{\partial D_{\xi H}}{\partial \Delta \hat{u}_n^{[i]}} - \psi^{[i]} \frac{\partial D_{\xi 2H}}{\partial \Delta \hat{u}_n^{[i]}} - D_{\xi H} \right) \tag{6.67}$$

$$\frac{\partial M^{[i]}}{\partial \psi^{[i]}} = K_n \left(J^{[i]} - \Delta \hat{u}_n^{[i]} \frac{\partial D_{\xi H}}{\partial \psi^{[i]}} - \psi^{[i]} \frac{\partial D_{\xi 2H}}{\partial \psi^{[i]}} - D_{\xi 2H} \right) \tag{6.68}$$

The components of $\frac{\partial \hat{\mathbf{S}}^{[i]}}{\partial \hat{\mathbf{s}}^{[i]}}$ are defined in Eqs.(6.57)-(6.68). By substituting $\frac{\partial \hat{\mathbf{S}}^{[i]}}{\partial \hat{\mathbf{s}}^{[i]}}$ into Equation (4.63), it is possible to evaluate the material stiffness ${\mathbf{K}_m}^{[i]}$ (see Algorithm 3).

6.4 Arc-length Method

In nonlinear problems, the equilibrium relation can be rewritten considering the residual vector $\mathbf{\Gamma}$, as follows:

$$\mathbf{\Gamma} = \mathbf{F}_i - \mathbf{F}_e = \mathbf{0} \tag{6.69}$$

To compute the tangent stiffness matrix and consequently solve the nonlinear problem, the classical Newton-Raphson iterative scheme is employed. The procedure can be summarized in the following steps:

$$\mathbf{\Gamma}_{(k+1)} = \mathbf{\Gamma}_{(k)} + \frac{\partial \mathbf{\Gamma}}{\partial \mathbf{d}}(\mathbf{d}_{(k+1)} - \mathbf{d}_{(k)}) = \mathbf{0} \tag{6.70}$$

where the residual vector $\mathbf{\Gamma}$ and the corrector $\delta\mathbf{d}$ at each iteration k are equal to:

$$\mathbf{\Gamma}_{(k)} = \mathbf{F}_{i(k)} - \mathbf{F}_e + \mathbf{K}_{(k)}\delta\mathbf{d} \tag{6.71}$$

$$\delta\mathbf{d} = -{\mathbf{K}_{(k)}}^{-1}(\mathbf{F}_{i(k)} - \mathbf{F}_e) \tag{6.72}$$

and so the solution will be:

$$\mathbf{d}_{(k+1)} = \mathbf{d}_{(k)} + \delta\mathbf{d} \tag{6.73}$$

where the subscript $_{(k)}$ denotes the old iteration and $_{(k+1)}$ the new iteration.

The Standard Newton-Raphson methods lead to instability near the limit points in case of snap-through and snap-back points, failing to predict the complete load-displacement response. At these points, the global stiffness matrix governing the equilibrium behavior becomes singular, therefore strategies such as arc-length techniques have been designed to overcome that numerical problem by increasing the equilibrium equation by means of an efficient constraint equation.

In this context, the arc-length methods are intended to enable solution algorithms to pass limit points, i.e. Fig.13 shows a possible load/displacement curve involving limit

points (A, B and C in the Fig. 13) with "snap-backs" [18]. These types of curves must impose a control on external forces to control displacements.

The equilibrium equation can be expressed according to Eq.6.69 as follows:

$$\mathbf{\Gamma}(\mathbf{U}, \lambda) = \mathbf{F}_i(\mathbf{U}) - \lambda \mathbf{F}_e = \mathbf{0} \tag{6.74}$$

where $\mathbf{F}_i$ are the internal forces which are functions of the displacement vector, $\mathbf{U}$, in which are collected all Lagrangian parameters of all rigid blocks, the vector $\mathbf{F}_e$ is the known external loading vector and the scalar λ is a "load-level parameter" that multiplies $\mathbf{F}_e$.

The most significant restriction of load control is that, near a limit point, there might be no intersection between the equilibrium configuration, Eq.(6.74), and the line λ=constant which represents the next "load level". Hence, to determine the intersection of Eq.(6.74), one introduces the arc length, denoted as s, defined by:

$$s = \int ds \tag{6.75}$$

where

$$ds = \sqrt{(d\mathbf{U}^T d\mathbf{U} + d\lambda^2 \psi^2 \mathbf{F}_e^T \mathbf{F}_e)} \tag{6.76}$$

where ψ is a possible scaling parameter.

Introducing the parameter s, Eq.(6.74) can be reformulated as follows:

$$\mathbf{\Gamma}(s) = \mathbf{F}_i(\mathbf{U}(s)) - \lambda(s) \mathbf{F}_e = \mathbf{0} \tag{6.77}$$

For the arc-length method in the Newton-Raphson iterative scheme, the differential form of Eq.(6.76) is replaced by the following incremental constraint:

$$a = (\Delta \mathbf{U}^T \Delta \mathbf{U} + \Delta\lambda^2 \psi^2 \mathbf{F}_e^T \mathbf{F}_e) - \Delta l^2 = 0 \tag{6.78}$$

where Δl is the assigned radius of the desired intersection, that is an approximation to the incremental arc-length. The vector $\Delta\mathbf{U}$ and scalar $\Delta\lambda$ are incremental, while for the iterative quantities, the symbol "δ" is utilized, referencing the last convergent equilibrium state. The most significant aspect of the arc-length method is that the load parameter, λ, becomes an additional variable in the problem, resulting in an increase in the number of problem variables from n to $n+1$.

By substituting Eqs.(6.74)-(6.78) into the Newton-Raphson iterative scheme of Eq.(6.70), considering all rigid blocks of the system with the displacement vector $\mathbf{U}$, the following expression is obtained:

$$\mathbf{\Gamma}_{(k+1)} = \mathbf{\Gamma}_{(k)} + \frac{\partial \mathbf{\Gamma}}{\partial \mathbf{U}}\delta\mathbf{U} + \frac{\partial \mathbf{\Gamma}}{\partial \lambda}\delta\lambda = \mathbf{\Gamma}_{(k)} + \mathbf{K}_{(k)}\delta\mathbf{U} - \mathbf{F}_e\delta\lambda = \mathbf{0} \tag{6.79a}$$

$$a_{(k+1)} = a_{(k)} + 2\Delta\mathbf{U}^T\delta\mathbf{U} + 2\Delta\lambda\delta\lambda\psi^2\mathbf{F}_e^T\mathbf{F}_e = 0 \tag{6.79b}$$

Setting $\mathbf{\Gamma}_{(k+1)}$ and $a_{(k+1)}$ to zero and solving for $\delta\mathbf{U}$ and $\delta\lambda$, the following results are obtained:

$$\left\{ \begin{array}{c} \delta\mathbf{U} \\ \delta\lambda \end{array} \right\} = \left[\begin{array}{cc} \mathbf{K}_{(k)} & -\mathbf{F}_e \\ 2\Delta\mathbf{U}^T & 2\Delta\lambda\psi^2\mathbf{F}_e^T\mathbf{F}_e \end{array} \right]^{-1} \left\{ \begin{array}{c} \mathbf{\Gamma}_{(k)} \\ a_{(k)} \end{array} \right\} \tag{6.80}$$

Eq. (6.80) can be used directly to find the value of $\delta\mathbf{U}$ and $\delta\lambda$ at each k iteration.

An alternative way of proceeding may be to split $\delta\mathbf{U}$ into two parts. Therefore, the iterative displacement $\delta\mathbf{U}$ at the new unknown load level, $\lambda_{(k+1)} = \lambda_{(k)} + \delta\lambda$, will be:

$$\begin{aligned} \delta\mathbf{U} &= -{\mathbf{K}_{(k)}}^{-1}\mathbf{\Gamma}(\mathbf{U}_{(k)}, \lambda) \\ &= -{\mathbf{K}_{(k)}}^{-1}(\mathbf{F}_i(\mathbf{U}_{(k)}) - \lambda_{(k+1)}\mathbf{F}_e) \\ &= -{\mathbf{K}_{(k)}}^{-1}(\mathbf{\Gamma}(\mathbf{U}_{(k)}, \lambda_{(k)}) - \delta\lambda\mathbf{F}_e) \end{aligned} \tag{6.81}$$

Then, the final form of $\delta\mathbf{U}$ can be expressed as:

$$\begin{aligned}\delta\mathbf{U} &= -\mathbf{K}_{(k)}{}^{-1}\mathbf{\Gamma}_{(k)} + \delta\lambda\mathbf{K}_{(k)}{}^{-1}\mathbf{F}_e \\ &= \delta\bar{\mathbf{U}} + \delta\lambda\delta\hat{\mathbf{U}}\end{aligned} \tag{6.82}$$

The first term $\delta\bar{\mathbf{U}}$ represents the iterative displacement associated with a fixed load level, $\lambda_{(k)}$. The second term $\delta\hat{\mathbf{U}}$ corresponds to the external load vector, $\mathbf{F}_e$.

After deriving $\delta\mathbf{U}$ from Eq.(6.82), the updated incremental displacements are given by:

$$\begin{aligned}\Delta\mathbf{U}_{(k+1)} &= \Delta\mathbf{U}_{(k)} + \delta\mathbf{U} \\ &= \Delta\mathbf{U}_{(k)} + \delta\bar{\mathbf{U}} + \delta\lambda\delta\hat{\mathbf{U}}\end{aligned} \tag{6.83}$$

where $\delta\lambda$ is the only unknown term, which can be found from Eq. (6.78), as follows:

$$\Delta\mathbf{U}_{(k)}{}^T\Delta\mathbf{U}_{(k)} + \Delta\lambda_{(k)}{}^2\psi^2\mathbf{F}_e^T\mathbf{F}_e = \Delta\mathbf{U}_{(k+1)}{}^T\Delta\mathbf{U}_{(k+1)} + \Delta\lambda_{(k+1)}{}^2\psi^2\mathbf{F}_e^T\mathbf{F}_e = \Delta l^2 \tag{6.84}$$

By substituting Eq.(6.83) into Eq.(6.84), the resulting expression is a quadratic equation in scalar form:

$$a_1\delta\lambda^2 + a_2\delta\lambda + a_3 = 0 \tag{6.85}$$

where

$$\begin{aligned}a_1 &= \delta\hat{\mathbf{U}}^T\delta\hat{\mathbf{U}} + \psi^2\mathbf{F}_e^T\mathbf{F}_e \\ a_2 &= 2\delta\hat{\mathbf{U}}^T(\Delta\mathbf{U}_{(k)} + \delta\bar{\mathbf{U}}) + 2\Delta\lambda_{(k)}\psi^2\mathbf{F}_e^T\mathbf{F}_e \\ a_3 &= (\Delta\mathbf{U}_{(k)} + \delta\bar{\mathbf{U}})^T(\Delta\mathbf{U}_{(k)} + \delta\bar{\mathbf{U}}) - \Delta l^2 + \Delta\lambda_{(k)}{}^2\psi^2\mathbf{F}_e^T\mathbf{F}_e\end{aligned} \tag{6.86}$$

which can be solved for $\delta\lambda$. The aim is to compute both solutions, $\delta\lambda_1$ and $\delta\lambda_2$, by finding the roots of the quadratic equation (6.85), and so to have both

$$\Delta\mathbf{U}_{(k+1),1} = \Delta\mathbf{U}_{(k)} + \delta\bar{\mathbf{U}} + \delta\lambda_1\delta\hat{\mathbf{U}} \tag{6.87}$$

and

$$\Delta\mathbf{U}_{(k+1),2} = \Delta\mathbf{U}_{(k)} + \delta\bar{\mathbf{U}} + \delta\lambda_2\delta\hat{\mathbf{U}} \tag{6.88}$$

For practical problems involving a realistic number of variables, the "loading terms" (linked to ψ) had no rilevant effect and this observation allows to set the scaling parameter to zero. This method is called "cylindrical method".

Setting $\psi = 0$ in Eq.(6.85) reveals the essence of the arc-length method. To implement the procedure, consider the solution with the minimum angle and maximum cosine between $\Delta\mathbf{U}_{(k)}$ and $\Delta\mathbf{U}_{(k+1)}$:

$$\cos\theta = \frac{(\Delta\mathbf{U}_{(k)})^T\Delta\mathbf{U}_{(k+1)}}{\Delta l^2} = \frac{(\Delta\mathbf{U}_{(k)})^T(\Delta\mathbf{U}_{(k)} + \delta\bar{\mathbf{U}})}{\Delta l^2} + \delta\lambda\frac{(\Delta\mathbf{U}_{(k)})^T\delta\hat{\mathbf{U}}}{\Delta l^2} = \frac{a_4 + a_5\delta\lambda}{\Delta l^2} \tag{6.89}$$

where, for $\psi = 0$

$$\begin{aligned} a_1 &= \delta\hat{\mathbf{U}}^T\delta\hat{\mathbf{U}} \\ a_2 &= 2\delta\hat{\mathbf{U}}^T(\Delta\mathbf{U}^{(k)} + \delta\hat{\mathbf{U}}) \\ a_3 &= (\Delta\mathbf{U}_{(k)} + \delta\bar{\mathbf{U}})^T(\Delta\mathbf{U}_{(k)} + \delta\bar{\mathbf{U}}) - \Delta l^2 \\ a_4 &= (\Delta\mathbf{U}_{(k)})^T\delta\bar{\mathbf{U}} + (\Delta\mathbf{U}_{(k)})^T\Delta\mathbf{U}_{(k)} \\ a_5 &= (\Delta\mathbf{U}_{(k)})^T\delta\hat{\mathbf{U}} \end{aligned} \tag{6.90}$$

6.4.1 Generalised Displacement Control at a Specific Parameter

The numerical procedure for the proposed models employs a single-parameter displacement control method. This alternative approach involves isolating a single parameter from the displacement vectors, which corresponds to the degree of freedom of the individual block being controlled.

To extract a single parameter from a vector $\mathbf{U}$ using a selection vector $\mathbf{M}$, multiply $\mathbf{M}$ and $\mathbf{U}$. The selection vector $\mathbf{M}$ enables the extraction of the desired parameter from the starting vector.

Let $\mathbf{U}$ be a column vector of size N, denoted as $\mathbf{U} = [U_1, U_2, U_3, \ldots, U_N]$.

Let $\mathbf{M}$ be a vector of dimensions $1 \times N$, where all entries are zero, except for a single entry set to one at the position that corresponds to the parameter to be extracted.

The selection vector $\mathbf{M}$ can be expressed formally as: $\mathbf{M} = [0, 0, \ldots, 1, \ldots, 0]$.

For instance, if $\mathbf{U} = [U_1, U_2, U_3, U_4, U_5, U_6]$ and the goal is to isolate the k-th parameter, $\mathbf{M}$ is defined as $[0, 0, \ldots, 1, \ldots, 0]$, with the entry at position k set to one. Consequently, the extraction process can be represented as:

$$\mathbf{U}(k) = U_k = \mathbf{MU} \tag{6.91}$$

and in components

$$U_k = \left\{ \begin{array}{ccccccc} 0 & 0 & \ldots & 1 & \ldots & 0 \end{array} \right\} \left\{ \begin{array}{c} U_1 \\ U_2 \\ U_3 \\ U_4 \\ U_5 \\ U_6 \end{array} \right\} \tag{6.92}$$

Performing the multiplication yields a scalar value that represents the isolated parameter. For instance, if the target parameter is the fourth one, it can be expressed as

follows:

$$U_4 = \left\{ \begin{array}{cccccc} 0 & 0 & 0 & 1 & 0 & 0 \end{array} \right\} \left\{ \begin{array}{c} U_1 \\ U_2 \\ U_3 \\ U_4 \\ U_5 \\ U_6 \end{array} \right\}$$

As mentioned earlier, Arc-Length methods, including the cylindrical one with $\psi = 0$, can be seen as forms of generalized displacement control. In these methods, the incremental displacement's Euclidean norm is constrained to a predetermined value, as shown in Eq.(6.84). Alternatively, some studies in the scientific literature suggest restricting the displacement increment in a specific variable to a particular quantity, resulting in a formulation different from Eq.(6.84).

Specifically:

$$\Delta \mathbf{U}_{(k+1)}(k) = \Delta \mathbf{U}_{(k)}(k) + \delta \mathbf{U}(k) = \Delta l \tag{6.93}$$

where $\Delta \mathbf{U}_{(k)}(k)$ is the k-th scalar component obtained from the vector $\Delta \mathbf{U}_{(k)}$ with the extraction process in Eq.(6.91). Using the Eq.(6.82), the iterative displacement $\delta \mathbf{U}$, which is divided into two components, $\delta \bar{\mathbf{U}}$ and $\delta \hat{\mathbf{U}}$, is then calculated to satisfy the constraint imposed by Eq.(6.93). It is possible to evaluate the following value:

$$\delta\lambda = \frac{\Delta l - \Delta \mathbf{U}_{(k)}(k) - \delta \bar{\mathbf{U}}_{(k)}(k)}{\delta \hat{\mathbf{U}}_{(k)}(k)} \tag{6.94}$$

where $\delta \bar{\mathbf{U}}_{(k)}(k)$ is the k-th scalar component obtained from the vector $\delta \bar{\mathbf{U}}_{(k)}$ with the extraction process in equation (6.91), similarly for $\delta \hat{\mathbf{U}}_{(k)}(k)$.

At the end of the procedure, the total displacement $\mathbf{U}_{(k+1)}$ is obtained by the sum of the iterative displacement and the incremental displacement of the actual iteration $k+1$.

The complete implementation procedure of a specific parameter control method is

outlined in Algorithm 4.

Algorithm 4: Cylindrical Arc-Length Method at a specific paramater.

Input : $\mathbf{F}_{i(k)}$, $\mathbf{F}_e$, $\mathbf{K}_{(k)}$, Δl, $\Delta\mathbf{U}_{(k)}$, $\mathbf{U}_{(k)}$ and k

Output: $\lambda_{(k+1)}$, $\delta\mathbf{U}$, $\Delta\mathbf{U}_{(k+1)}$ and $\mathbf{U}_{(k+1)}$

Comupute the actual residual $\boldsymbol{\Gamma}$ of Eq. (6.74);

Perform the extraction process (Eq. (6.91)) for the new constraint (6.93) to evaluate the k-th scalar components $\Delta\mathbf{U}_{(k)}(k)$, $\delta\bar{\mathbf{U}}_{(k)}(k)$ and $\delta\hat{\mathbf{U}}_{(k)}(k)$;

Comupute the iterative parameter $\delta\lambda$ of Eq. (6.94);

Solve the problem computing the actual load level: $\lambda_{(k+1)} = \lambda_{(k)} + \delta\lambda$;

Comupute the iterative displacement $\delta\mathbf{U}$ split into $\delta\bar{\mathbf{U}}$ and $\delta\hat{\mathbf{U}}$ of Eq. (6.82);

Compute the new incremental displacement $\Delta\mathbf{U}_{(k+1)}$ of Eq. (6.83);

Find the total displacement: $\mathbf{U}_{(k+1)} = \mathbf{U}_{(k)} + \Delta\mathbf{U}_{(k+1)}$.

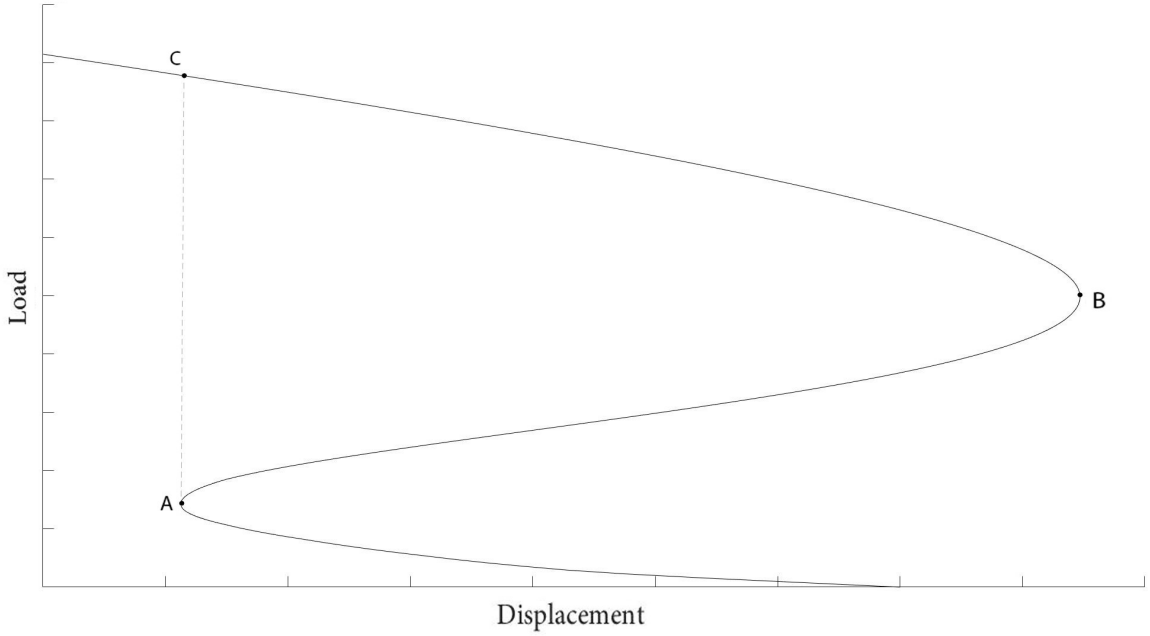

Figure 13: Displacement/Load curve: example of snap-back.

7 Numerical Applications

The rigid block model with interfaces, accounting for both geometrical and material nonlinearity, and the numerical procedure presented in the previous sections are utilized to develop some numerical applications. Nonlinear static analyses are conducted using a specific Matlab code. The numerical results are presented and compared to those obtained through small displacements and limit analysis using an Upper-Bound Limit Analysis algorithm. In this limit analysis scenario, no-tension and frictional joints are considered, ignoring cohesion in both normal and tangential directions [89].

In particular, this section describes three types of applications, which are organized into the following subsections:

- In subsection 7.1, preliminary tests on a single block are analyzed to assess the performance of the proposed model in reproducing the behavior of cohesive interfaces under large displacements. This benchmark problem is designed to investigate the interaction between geometrical and material nonlinearity, a factor that has not been thoroughly quantified in the existing literature. To validate the interface model's accuracy, an investigation of the variation of the interface angle (hereafter referred to as the "tilt angle") is also performed;

- In subsection 7.2, three analyses of a multi-block structure are conducted to evaluate the capabilities of the proposed model. Specifically, the study focuses on the resonance of the trilithon structure, a simple yet impactful configuration, in the context of large displacement studies, as discussed in the dynamic behavior of m-block structures by Lourenço et al. [55]. The analysis includes sensitivity assessments of both geometric parameters, such as the base-to-height ratio, and material parameters, such as friction coefficient;

- In subsection 7.3, the discrete element analyses of a masonry arch is performed. The numerical results obtained in terms of force-displacement curves in large displacements are put in comparison with a numerical example of Como [61] and

Brandonisio [72] in terms of failure mechanism. Two different discretizations are considered, each with a different number of blocks represented by the parameter n_b. The computations are performed using different values for the geometric parameters, such as thickness, and material parameters, such as friction coefficient.

7.1 Application 1: Analysis of a Single Structural Element

This section presents theoretical examples of the mechanical response of the interface model. These simple examples serve as valuable tests to aid in understanding the model's function when large displacements occur. The simulations presented here are purely theoretical and aim to help understand the algorithm's functioning before moving on to more engineering-oriented applications.

A rectangular block loaded in compression and shear is studied. This simple structure adheres to a rigid base, as schematically illustrated in Fig.14. The block is characterized by the following geometric properties: $b = 4$ and $h = 2$, while the interface mechanical parameters adopted for the computations are reported in Tab.4.

The contact interface is modeled using 5 Gauss points into 10 subdomains.

The initial compression is achieved by applying a vertical force at the centroid of the block to obtain a total vertical load equal to $F_2 = -10$. The vertical force remains constant throughout the analysis, while the horizontal force at the centroid of the block changes until the horizontal displacement reaches the value of $U_1 = 0.2$. To fully capture the mechanical response of the block, numerical analysis is conducted using the arc-length technique, described in Sub. 6.4, with local control of the horizontal displacement at the centroid, U_1, where the variable load is applied.

Three analyses are performed to test the unilateral nature of the contact and the friction effect in large displacements. To capture both overturning and sliding mechanisms, the material properties are characterized by three values of the friction coefficients.

Table 4: Interface mechanical properties adopted for the analysis of simple and multi-block structures.

	K_n	K_t	$\Delta\tilde{u}_n^0$	$\Delta\tilde{u}_n^f$	$\Delta\tilde{u}_t^0$	$\Delta\tilde{u}_t^f$	μ
1	10000	10000	0.005×10^{-2}	0.05×10^{-2}	0.02×10^{-1}	0.20×10^{-1}	0
2	10000	10000	0.005×10^{-2}	0.05×10^{-2}	0.02×10^{-1}	0.20×10^{-1}	0.5
3	10000	10000	0.005×10^{-2}	0.05×10^{-2}	0.02×10^{-1}	0.20×10^{-1}	5

The following graphs show the mechanical response of the block for the considered interface material properties:

- In Figure 15, the horizontal force F_1 is plotted as a function of the horizontal displacement U_1 of the centroid, assuming material 1 (blue line), material 2 (green line), and material 3 (red line) for the interface. The figure also shows the failure mechanisms while varying the friction coefficient.

- In Figure 16, the horizontal force F_1 is plotted as a function of the horizontal displacement U_1 of the centroid for the case of frictionless, $\mu = 0$. The graph shows the algorithm's progression towards convergence. Each blue point on the curve corresponds to the accompanying configuration.

- In Figure 17, the horizontal force F_1 is plotted as a function of the horizontal displacement U_1 of the centroid, assuming material 1 (blue line), material 2 (green line), and material 3 (red line) for the interface with a tilt angle equal to 10 degrees.

Figure 15 illustrates also the equilibrium configuration of the block for several interface materials characterized by two different friction coefficients, each corresponding to an assigned horizontal displacement of 0.2. Specifically, with a friction coefficient of $\mu = 5$, an overturning failure mechanism is observed. In contrast, when the friction coefficient is $\mu = 0.5$, a sliding failure mechanism occurs. The algorithm operates effectively even in the case of frictionless, with $\mu = 0$.

Figure 16 illustrates a specific focus on the case $\mu = 0$ to investigate the evolution of the response curve. In a scenario of frictionless, a perfectly bilateral response would be expected. Upon entering the algorithm's operation, it is observed that instead of immediately transitioning to the expected solution of sliding, the algorithm initially yields a result of overturning (because of the tangential cohesion). This is followed by a mixed mechanism involving both overturning and sliding before, finally, stabilizing into pure sliding.

The above description highlights the complexity of the model, even in a simple case like a single block. The algorithm must converge through a succession of mechanisms before stabilizing due to the significant nonlinearity of the involved phenomena. The gradual transition is also influenced by the number of iterations set for each load step.

To verify the interface model's accuracy, an investigation of the variation of the tilt angle is also performed. In this simulation, the rigid block is considered trapezoidal and has a tilt angle of 10 degrees. Figure 17 shows that the algorithm can handle interfaces with non-zero tilt angle, capturing both overturing and sliding mechanism.

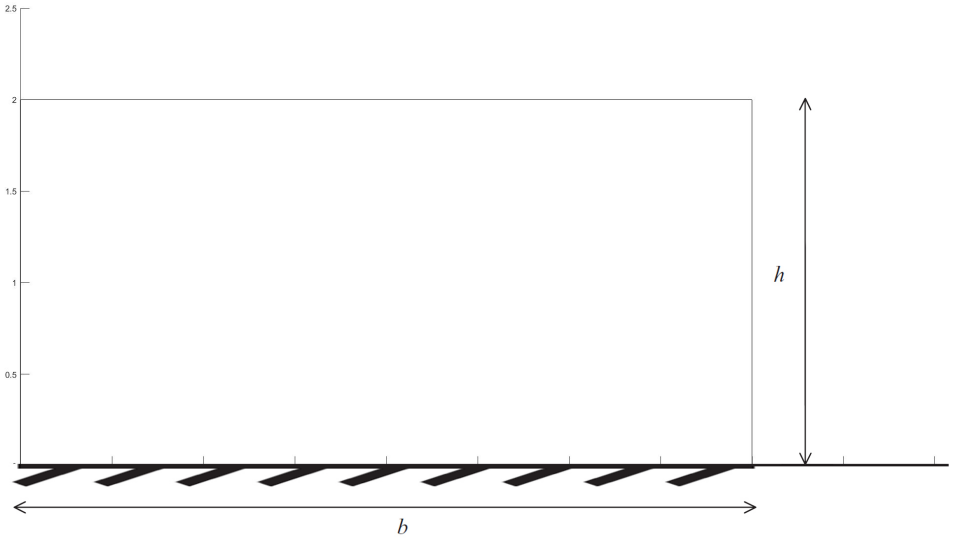

Figure 14: Rectangular block joined with a rigid base.

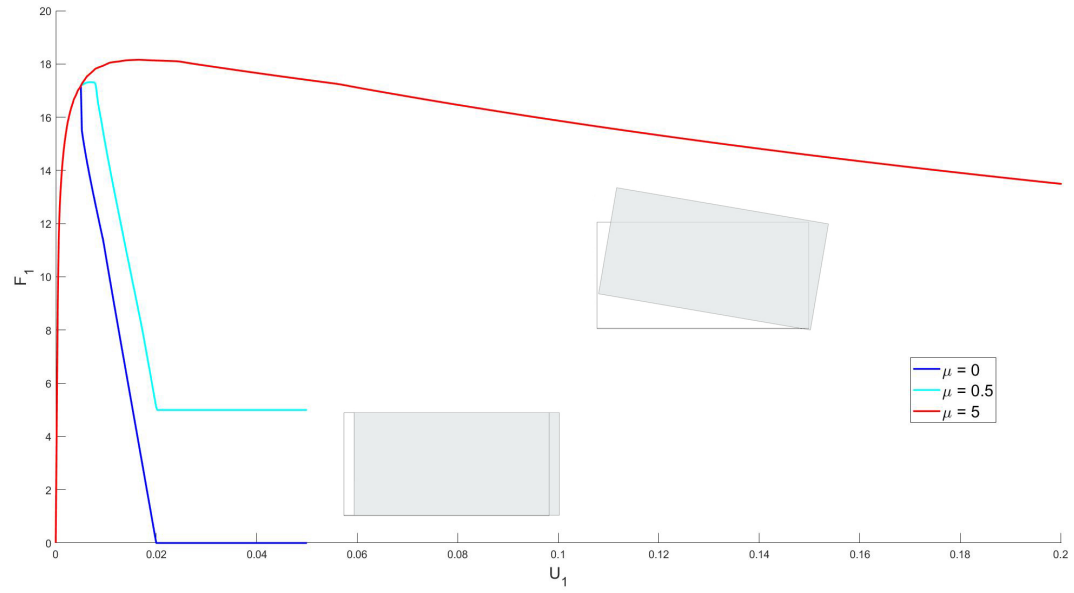

Figure 15: Horizontal reaction force F_1 as a function of the horizontal displacement U_1, varying the friction coefficient.

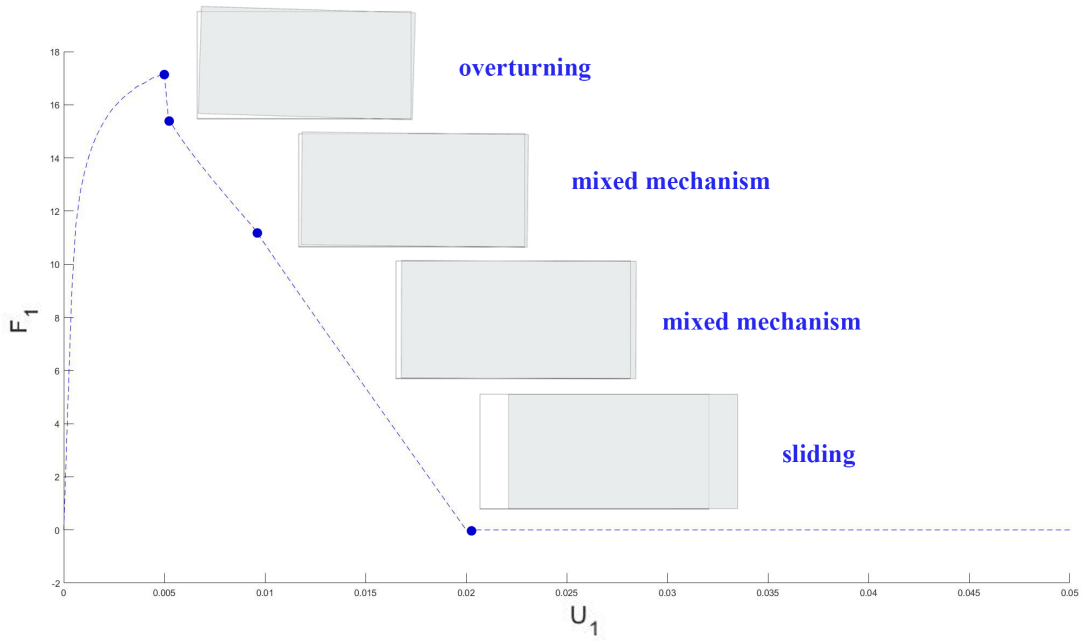

Figure 16: Horizontal reaction force F_1 as a function of the horizontal displacement U_1 for $\mu = 0$. Evolution of response from overturning-sliding mechanism to sliding failure mechanism.

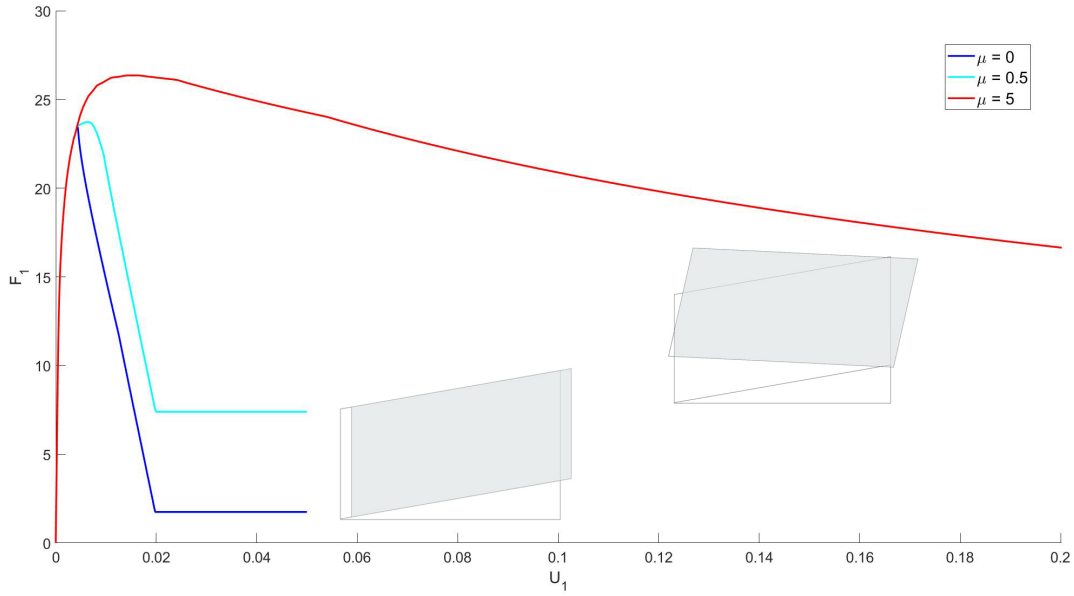

Figure 17: Horizontal reaction force F_1 as a function of the horizontal displacement U_1 of a single block with $\psi_0 = 10°$, varying the friction coefficient.

Tests using moderate rotations and varying friction coefficient are then conducted. The investigation aims to identify potential differences between solutions obtained with large displacements using finite rotations versus moderate rotations. The horizontal displacement at the centroid, U_1, is controlled until it reaches a value of 0.5, exceeding the previously used value of 0.2.

The graphs described below compare the mechanical response of a single block under large displacements, considering both finite rotations and moderate rotations. The responses in small displacements and the ultimate load through limit analysis are also evaluated.

In particular:

- In Figure 18, the horizontal force F_1 is plotted as a function of the horizontal displacement U_1 of the centroid, adopting material 3 of Tab.4 for the interface. The numerical results for large displacements are obtained by considering both finite rotations (blue line) and moderate rotations (green line). The response curve

in linear theory (red line) and the ultimate load (dashed line) are also included. The figures present the obtained mechanisms (Fig.19) and the results of the limit analysis approach (Fig.20).

- In Figure 21, the horizontal force F_1 is plotted against the horizontal displacement U_1 of the centroid. For the interface, material 2 of Tab.4 is used and the same studies are considered as in the case of material 3 (Figs.22-23).

The graphs in Figure 18 indicate that the response of the block under large displacements shows a softening behavior compared to the same block under small displacements. In addition, the same figure reports the value of the failure load obtained, $F_{1lim} = 20$, by applying the kinematic theorem of limit analysis, as indicated by the optimal solution of load multiplier shown in Figure 20. It is important to note that:

- The numerical models in large displacements differ from the model in small displacements as the horizontal displacement at the centroid increases, exhibiting (1) two different peak loads and (2) a softening behavior in nonlinear theory while asymptotically approaching the collapse load in linear theory.

- When displacements are significant, the difference between the curve for finite rotations and the curve for moderate rotations also becomes significant.

- The collapse load deduced by the limit analysis with no cohesion represents the upper bound of the ultimate strength of the block.

In the last conducted analysis, the interface parameters associated for material 2 of Tab.4 are applied. By using a lower friction coefficient compared to material 3, sliding mechanism is captured (as shown in Fig.22 by applying a scale factor of 10) when the limit load equals 5, which is evaluated by the limit analysis algorithm (Fig.23).

In this case, the response curves in large displacements and small displacements overlap. The solution obtained from linear theory is equivalent to that of nonlinear

theory because the displacement obtained is very small compared to the dimensions of the structure. The damage evolves until the complete decohesion of the interface, i.e. $D = 1$ for all points of the interface.

The numerical results demonstrate that the proposed model effectively reproduces the behavior of the cohesive interface during large displacements, capturing the main features of combined damage and friction effects in large displacements.

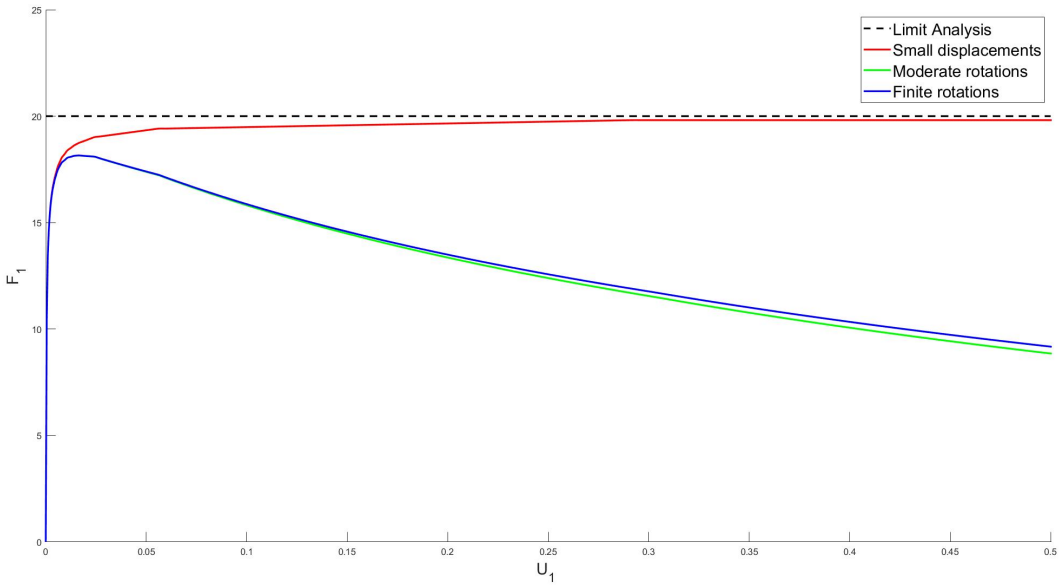

Figure 18: Testing a single block with the material 3 of Tab. 4 for the interface: Limit load (dashed line) and numerical results obtained considerng the Linear Theory (red line), Moderate Rotations (green line) and Finite Rotations (blue line).

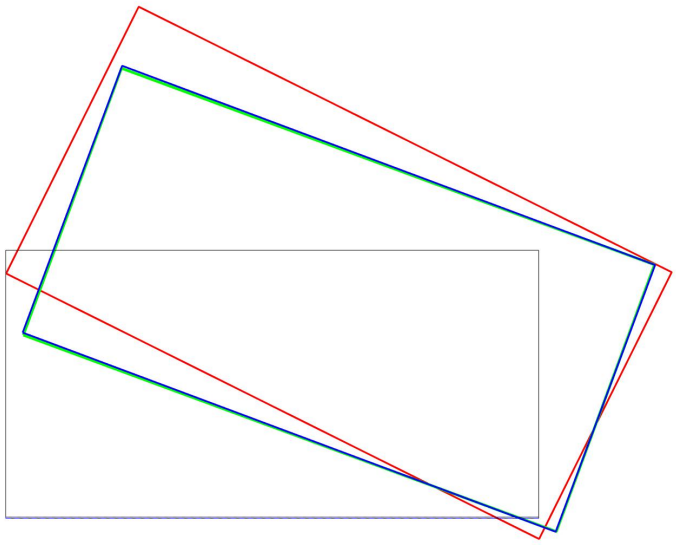

Figure 19: Testing a single block with the material 3 of Tab. 4 for the interface: Comparison of the overturning mechanism obtained with Linear theory (red line), Moderate Rotations (green line) and Finite Rotations (blue line).

```
Optimal solution found.

it =    1     err = 1.0000e+00
Optimal solution found.

it =    2     err = 0.0000e+00lambda = 2.0000e+00
Internal forces from equilibrium
interface =    1   Shear =  2.0000e+01     Normal = -1.0000e+01     Moment = -2.0000e+01
```

Figure 20: Testing a single blockwith the material 3 of Tab. 4 for the interface: Upper-Bound Limit Analysis algorithm to evaluate the Limit load [89].

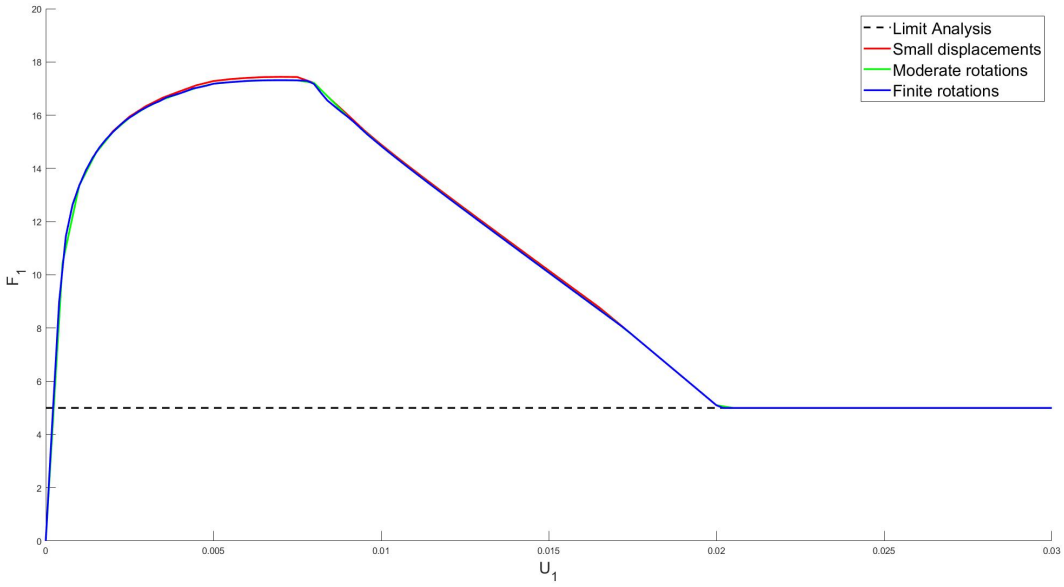

Figure 21: Testing a single block with the material 2 of Tab. 4 for the interface: Limit load (dashed line) and numerical results obtained considerng the Linear Theory (red line), Moderate Rotations (green line) and Finite Rotations (blue line).

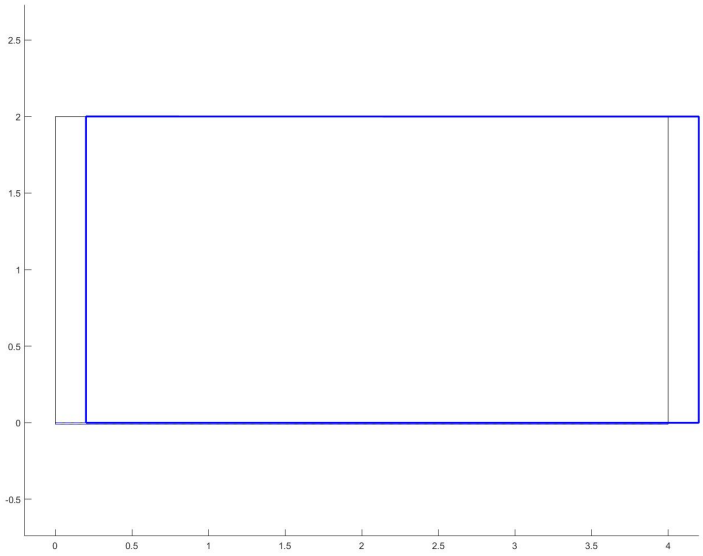

Figure 22: Testing a single block with the material 2 of Tab. 4 for the interfacee: sliding mechanism (Scale factor 10).

```
Optimal solution found.

it =    1     err = 1.0000e+00
Optimal solution found.

it =    2     err = 5.0000e-01
Optimal solution found.

it =    3     err = 0.0000e+00lambda = 5.0000e-01
Internal forces from equilibrium
interface =    1   Shear =  5.0000e+00     Normal = -1.0000e+01     Moment = -5.0000e+00
```

Figure 23: Testing a single block with the material 2 of Tab. 4 for the interface: Upper-bound Limit Analysis algorithm to evaluate the Limit load [89].

7.2 Application 2: Analysis of Triliths

This subsection analyzes a multi-block structure to assess the capabilities of the proposed model. The study specifically explores the behavior of the trilithon structure, a configuration known for its simplicity and impact in large displacement studies. An example of this application is the study of Lourenço et al. concerned with Rocking Motion dynamics [55]. The analysis includes sensitivity assessments for the geometric parameters, such as the base-to-height ratio of the pillar, and material parameters, such as the friction coefficient. In the following subsection, the simulations are purely theoretical, aimed at testing the algorithm's correct functioning as the number of blocks and interfaces increases.

The trilith is composed of three rigid blocks: a lintel and two pillars. The columns have base-to-height ratios of 0.5, 0.75, and 1, respectively, with the base denoted as s and the height as h in Fig.24. In the simulations that follow, both the geometry of the blocks and the friction coefficient were set to capture overturning and sliding mechanisms. In the case of small displacements and limit analysis, sliding occurs when the following condition is met:

$$\mu < \frac{s}{h} \tag{7.1}$$

where μ represents the static coefficient of friction.

The study focuses on a trilith loaded in compression and shear. The structure has a simple design, as shown in Fig.24. The lintel has a base of 14 and a height of 2. The columns have a base (s) of either 2, 3, or 4 and a height (h) of 4 (resulting in base-to-height ratios of 0.5, 0.75, and 1, respectively). The mechanical parameters used for the simulations are listed in Tab.4 with the exception of the friction coefficient value, μ, which will be varied according to Eq.(7.1).

Three different sets of material properties are considered for each of the three triliths. These materials differ in the values assumed for the friction coefficient, μ:

- for the trilith with a base-to-height ratio of 0.5, the friction coefficient takes on the values of 0.1, 0.3, and 0.7;
- for the trilith with a base-to-height ratio of 0.75, the friction coefficient takes on values of 0.1, 0.3, and 0.9;
- for the trilith with a base-to-height ratio of 1, the friction coefficient takes on values of 0, 0.9, and 5.

The contact interface between the block and its support, and between the blocks themselves, is modeled by 5 Gauss points into 10 subdomains.

The compression process begins by applying a vertical force at the centroid of each block to obtain a vertical load of either $F_{2p} = -10, -15$, or -20 for pillars and $F_{2l} = -35$ for lintel. These vertical forces remain constant throughout the analysis. The horizontal force at the centroid of each block changes until the horizontal displacement of the lintel reaches $U_{1l} = 2$. To capture the mechanical response of the structure, numerical analysis is conducted using the arc-length technique described in Sub.6.4. The analysis includes local control of the horizontal displacement at the centroid of the lintel, U_{1l}. The subscript $_l$ is omitted below.

Three analyses are performed to test the unilateral nature of the contact and the friction effect in large displacements, considering three different mechanical properties of

the interface. The mechanical response of the trilith in large displacements is compared with the solution in small displacements and the limit load value obtained from the Limit Analysis algorithm [89].

The graphs below depict the mechanical response of the structure for the trilith's various geometrical configurations, as follows:

- In Figure 25, the horizontal force F_1 is plotted as a function of the horizontal displacement U_1 of the lintel centroid for the trilith with $s/h = 0.5$. In the context of this specific geometric configuration, different friction coefficients are considered: $\mu = 0.1$ (blue lines), $\mu = 0.3$ (red lines), and $\mu = 0.7$ (black lines) for the interface.

- In Figure 26, the horizontal force F_1 is plotted as a function of the horizontal displacement U_1 of the lintel centroid for the trilith with $s/h = 0.5$ and $\mu = 0.7$. The graph also includes the Limit Load evaluated using the Kinematic Approach of Limit Analysis.

- In Figure 27, the horizontal force F_1 is plotted as a function of the horizontal displacement U_1 of the lintel centroid for the trilith with $s/h = 0.5$ and $\mu = 0.1$. The graph shows the algorithm's progression towards convergence. Each blue point on the curve represents a corresponding configuration.

- In Figure 28, the horizontal force F_1 is plotted as a function of the horizontal displacement U_1 of the lintel centroid for the trilith with $s/h = 0.5$ and $\mu = 0.3$. The graph shows the algorithm's progression towards convergence. Each blue point on the curve corresponds to the accompanying configuration.

- in Figure 29, the horizontal force F_1 is plotted as a function of the horizontal displacement U_1 of the lintel centroid for the trilith with $s/h = 0.75$. For this specific geometric configuration, different friction coefficients are considered: $\mu = 0.1$ (blue lines), $\mu = 0.3$ (red lines), and $\mu = 0.9$ (black lines) for the interface.

- in Figure 30, the horizontal force F_1 is plotted as a function of the horizontal displacement U_1 of the lintel centroid for the trilith with $s/h = 1$. For this specific geometric configuration, different friction coefficients are considered: $\mu = 0$ (blue lines), $\mu = 0.9$ (red lines), and $\mu = 5$ (black lines) for the interface.

The solid curves represent finite rotations, the dashed curves represent moderate rotations, and the dot-dashed curves represent small displacements. The graph displays the response curves for large and small displacements, as well as the actual configurations obtained for large displacements, while varying the friction coefficient. The colors of the response curves correspond to the colors of the actual configurations.

Figure 25 shows the equilibrium configuration of the trilith for different interface materials with varying friction coefficients. Each configuration corresponds to an assigned lintel horizontal displacement of 2. An overturning failure mechanism is observed with a friction coefficient of $\mu = 0.7$. In contrast, if the friction coefficient satisfies the Eq.(7.1), a sliding failure mechanism will occur.

In particular:

- When $\mu > s/h$, a overturning failure mechanism is observed. The load multiplier is evaluated using the Kinematic Approach of Limit Analysis and is equal to 0.5. The collapse load deduced by the limit analysis represents the upper bound of the ultimate strength of the trilith, as shown in Fig.26. The solution in small displacements asymptotically tends to the ultimate load, while the curves in large displacements initially approximate each other and then differentiate as the displacement increases, reaching the value of 2.

- When $\mu < s/h$, a sliding failure mechanism is observed. An overturning-sliding mechanism is observed for $\mu = 0.3$, while only a sliding mechanism is observed for $\mu = 0.1$.

Figure 27 illustrates a specific focus on the evolution of the response curve for the case $\mu = 0.1$. The algorithm initially yields a result of overturning, followed by

a mixed mechanism involving both overturning and sliding, before finally stabilizing into sliding mechanism, instead of immediately transitioning to the expected solution of sliding. The algorithm for the proposed model follows the observations highlighted in the previous subsection.

Figure 28 illustrates a specific focus on the evolution of the response curve for the case $\mu = 0.3$. For this intermediate scenario, the algorithm identifies different equilibrium configurations before the solution shows a final mixed mechanism involving sliding for the left pillar and overturning for the right one.

Finally, Figures 29 and 30 confirm the observations highlighted by the analyzed case in Figure 25. Specifically, three types of mechanisms in large displacement can always be observed by varying the interface friction coefficient:

- Overtuning mechanism when $\mu > s/h$;
- Sliding mechanism when $\mu < s/h$;
- There is also an intermediate scenario where one pillar exhibits a sliding mechanism and another exhibits a rocking mechanism. This observation is consistent with various studies conducted in the field of dynamics to investigate rocking behavior, such as the work by Lourenço [55].

Furthermore, when comparing the response curves obtained from large and small displacement procedures, it is evident that:

- When the overturning mechanism occurs, the solution for large displacements differs significantly from that for small displacements. However, the solution for small displacements asymptotically tends to the ultimate load. When analyzing the curves for large displacements, it is noticeable that they tend to have two distinct softening branches when utilizing the implementation of finite rotations or the approximation of moderate rotations.

- When the sliding mechanism occurs, the solutions in large and small displacements overlap. In this case, the horizontal displacement obtained is small compared to the dimension of the structure. Therefore, the response curves of linear theory and nonlinear theory overlap.

- In the case of the mixed mechanism, the curve may diverge from the ultimate load value after a horizontal segment along the x-axis typical of the sliding mechanism, and continue with a softening branch typical of the overturning mechanism (refer to the study of $\mu = 0.3$ in Fig.25 and $\mu = 0.9$ in Fig. 30). Alternatively, there may be a prevalence of the sliding mechanism, where the solutions in large and small displacements tend to overlap (refer to the study of of $\mu = 0.3$ in Fig. 29).

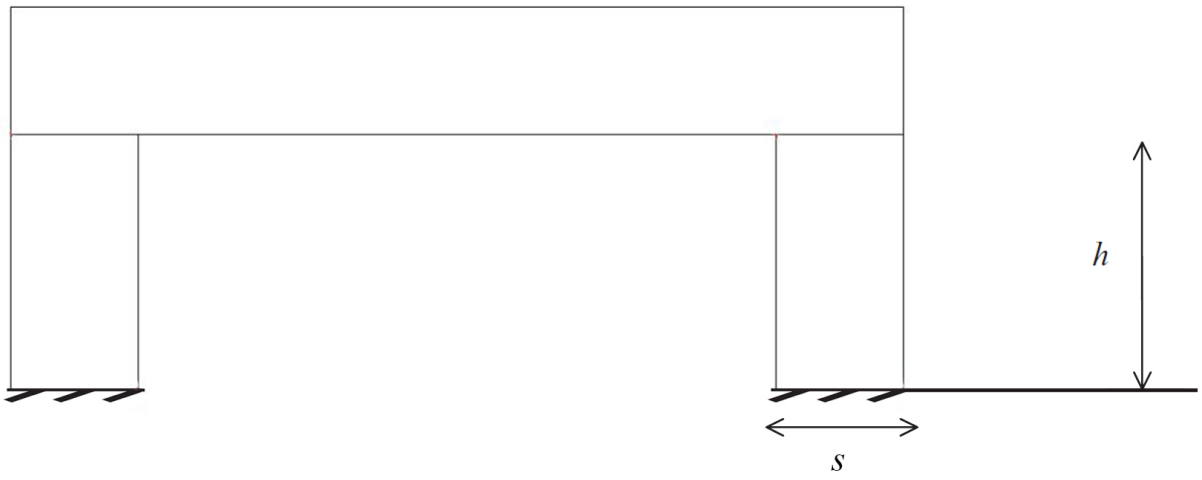

Figure 24: Trilith joined with a rigid base.

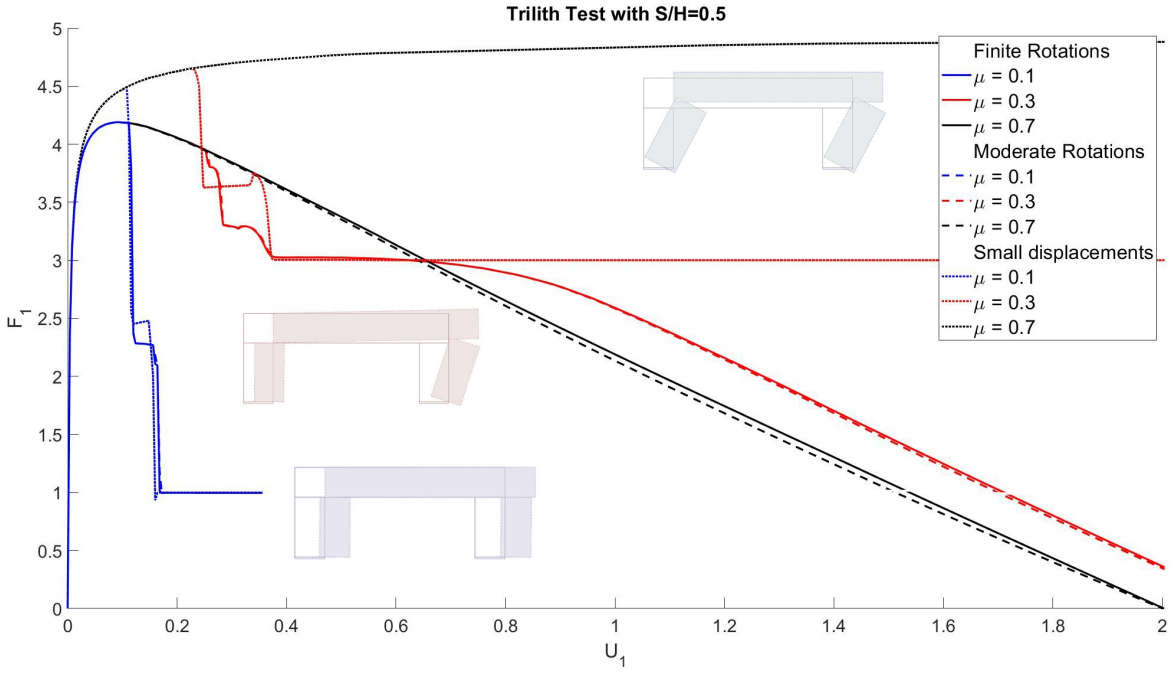

Figure 25: Horizontal reaction force F_1 as a function of the horizontal displacement U_1 of trilith's lintel with a base-to-height ratio (S/H) of 0.5, varying the friction coefficient.

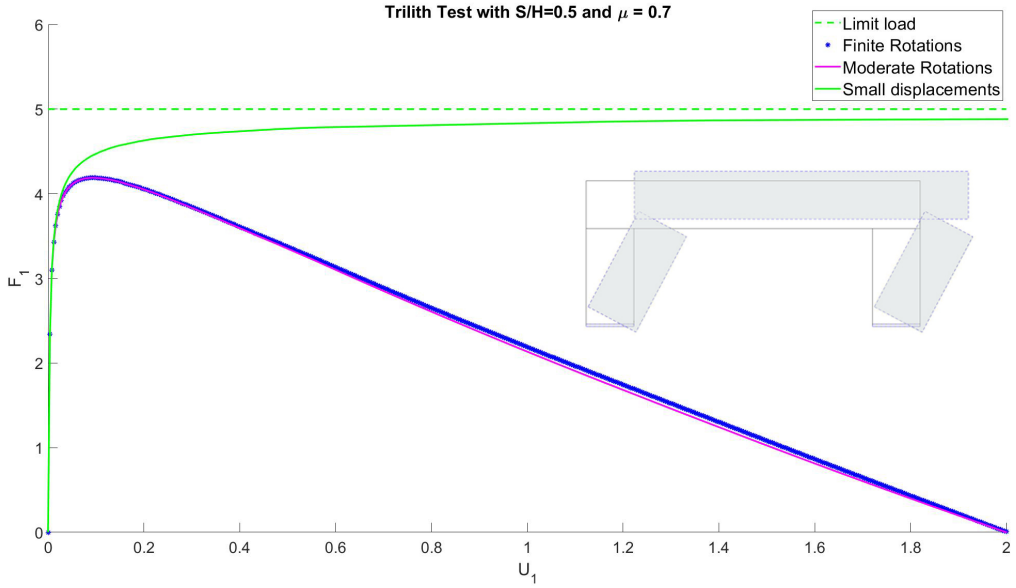

Figure 26: Horizontal reaction force F_1 as a function of the horizontal displacement U_1 of trilith's lintel with a base-to-height ratio (S/H) of 0.5, for $\mu = 0.7$.

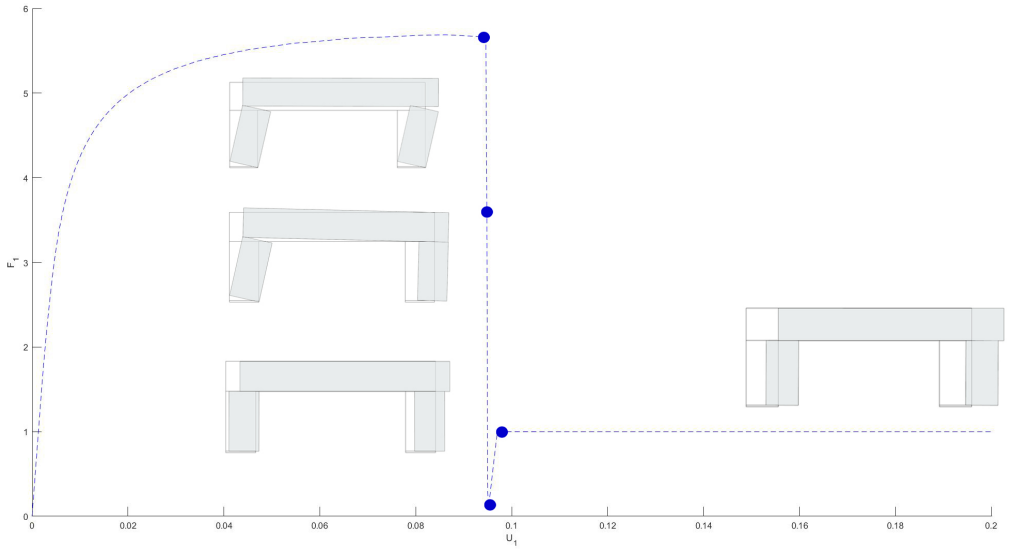

Figure 27: Horizontal reaction force F_1 as a function of the horizontal displacement U_1 of trilith's lintel with a base-to-height ratio (S/H) of 0.5, for $\mu = 0.1$, by implementing the iterations for step load. Evolution of response from overturning-sliding mechanism to sliding failure mechanism. The equilibrium configurations are plotted by applying a scale factor of 10.

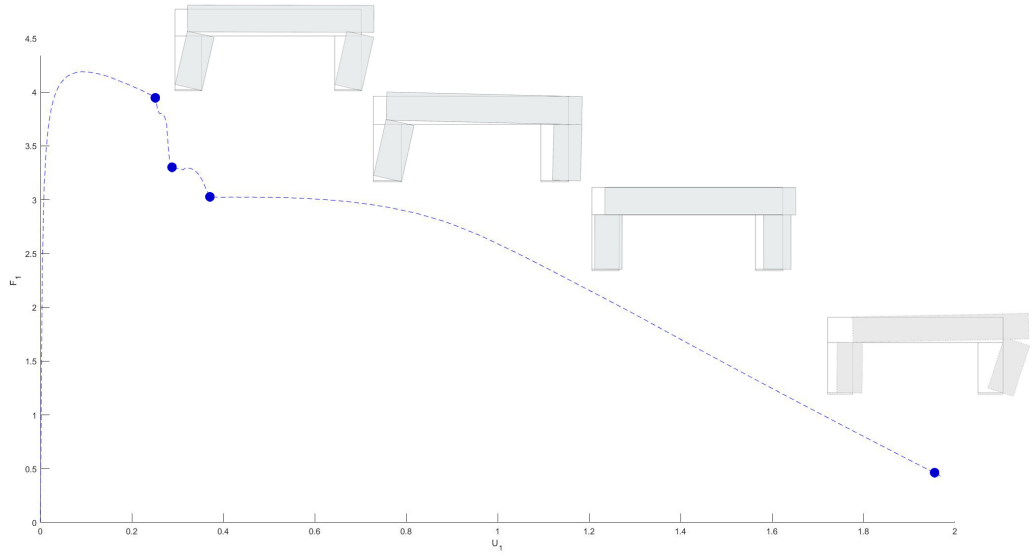

Figure 28: Horizontal reaction force F_1 as a function of the horizontal displacement U_1 of trilith's lintel with a base-to-height ratio (S/H) of 0.5, for $\mu = 0.3$. Evolution of response from overturning mechanism to mixed mechanism. The equilibrium configurations are plotted by applying a scale factor of 10.

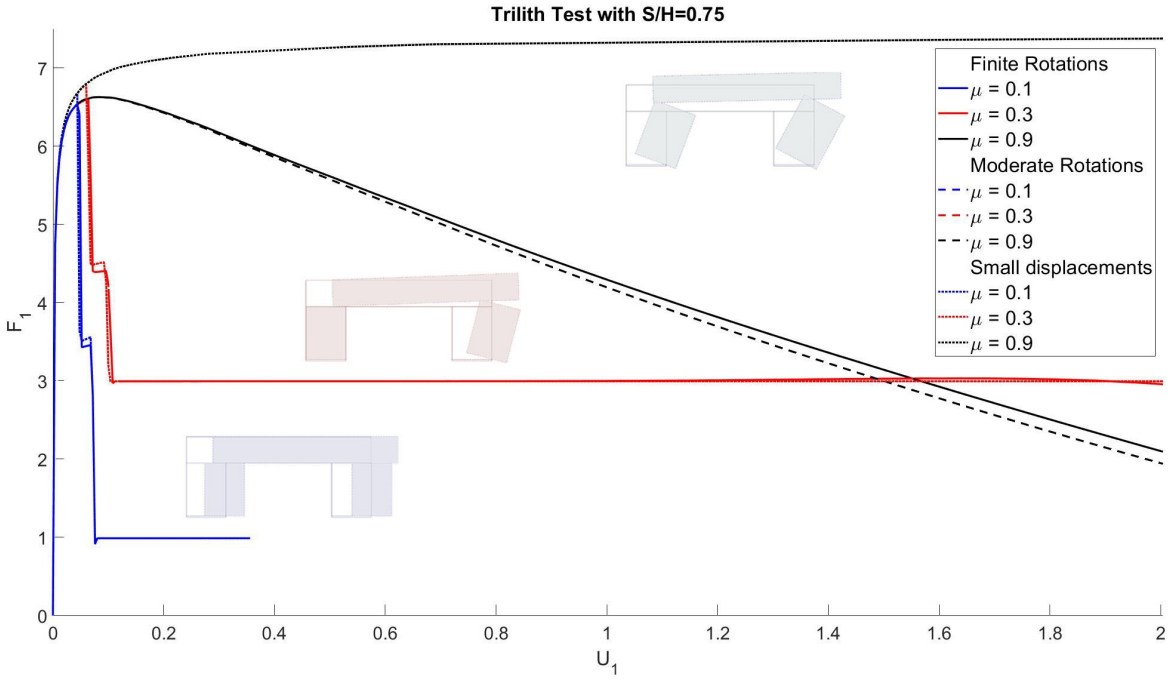

Figure 29: Horizontal reaction force F_1 as a function of the horizontal displacement U_1 of trilith's lintel with a base-to-height ratio (S/H) of 0.75, varying the friction coefficient.

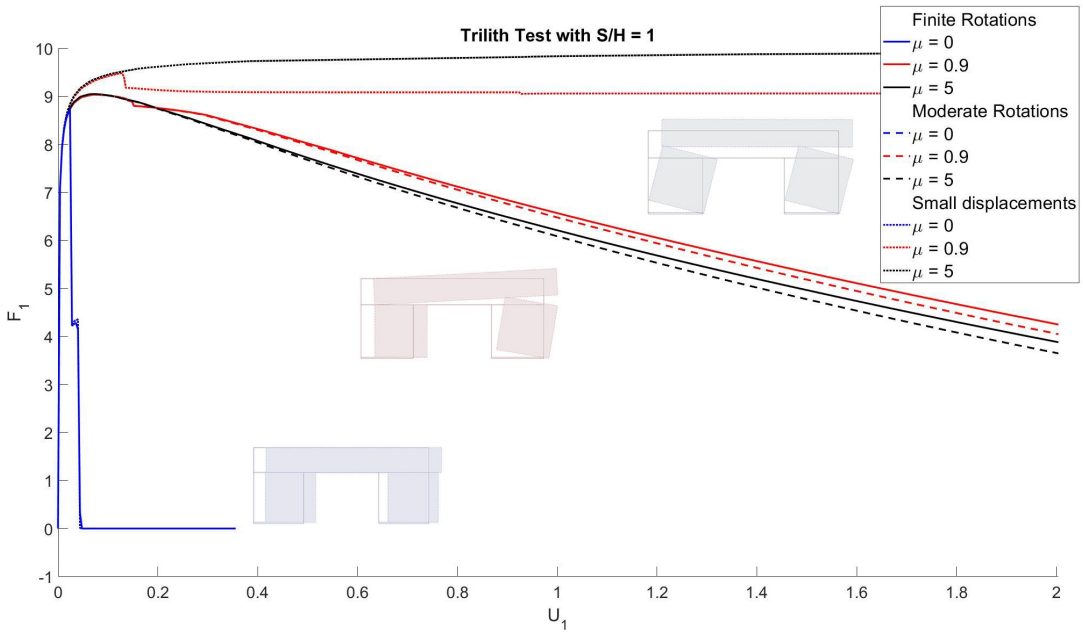

Figure 30: Horizontal reaction force F_1 as a function of the horizontal displacement U_1 of trilith's lintel with a base-to-height ratio (S/H) of 1, varying the friction coefficient.

7.3 Application 3: Analysis of Masonry Arches

After validating the proposed numerical procedure through theoretical applications in the previous subsections, this section delves into a practical engineering-oriented case of significant interest in the study of masonry constructions.

This section examines a circular arch that has been previously studied by Como [61] and Brandonisio et al. [72].

Using Heyman's assumptions for analyzing masonry structures under horizontal forces, Como applied the theorems of Limit Analysis to evaluate the potential collapse of masonry structures. The examination focused on the effect of geometry on horizontal capacity. Brandonisio et al. utilized Como's numerical example and load multiplier result as a benchmark value to validate the proposed model within the Kinematic Approach of Limit Analysis with infinite friction.

This section conducts a discrete element analysis of the reference arch in large displacements. The discrete element modeling strategy involves adopting a nonlinear material and geometrical model for the interfaces and calibrating contact mechanical parameters to compare the obtained mechanisms with the work of Como and Brandonisio.

The geometrical data of the round arch, schematically depicted in Fig.31, are as follows: span length $L = 15$ m, internal radius $R = 7.5$ m, thickness $t = 1.2$ m. The mechanical parameters used for the computations are listed in Table 5. The contact interface between the block and its support, and between the blocks themselves, is modeled by 5 Gauss points into 10 subdomains.

The arch is discretized into 9 blocks and 10 interfaces to study the mechanism of 4 hinges [61], based on the hinge positions obtained in the works of Como and Brandonisio.

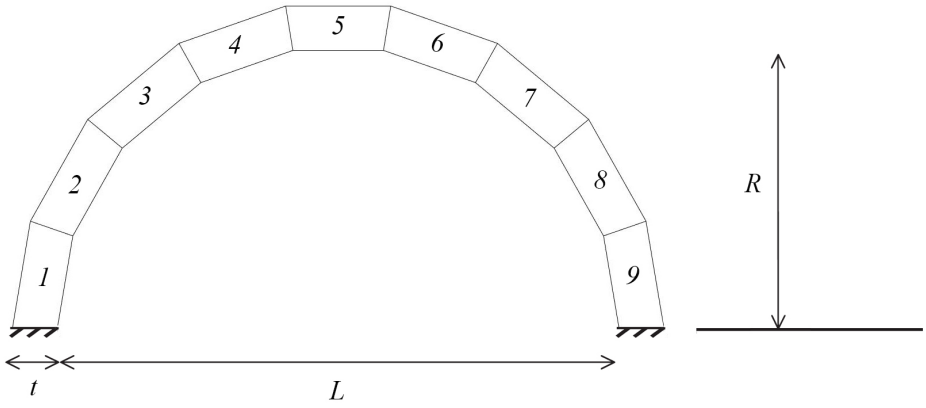

Figure 31: Round arch joined with a rigid base. The arch consists of 9 blocks and 10 interfaces.

Table 5: Interface mechanical properties adopted for the analysis of the arch.

	K_n [kN/m^3]	K_t [kN/m^3]	$\Delta\tilde{u}_n^0$ [m]	$\Delta\tilde{u}_n^f$ [m]	$\Delta\tilde{u}_t^0$ [m]	$\Delta\tilde{u}_t^f$ [m]	μ
1	1000000	1000000	0.005×10^{-2}	0.05	0.02×10^{-1}	0.05	5
2	1000000	1000000	0.005×10^{-2}	0.05	0.02×10^{-1}	0.05	0.098

During the simulation, the weight of the arch remains constant ($\gamma = 16$ kN/m^3), and the horizontal forces are applied at the centroids of the blocks until block 5 reaches a horizontal displacement of 0.18 m (U_1). To fully capture the mechanical response of the structure, a numerical analysis is performed with local control of the horizontal displacement at the centroid of block 5.

The mechanical response of the structure is expressed in terms of the horizontal reaction force, F_1 [kN], versus the horizontal displacement component, U_1 [m], at the centroid of the controlled block 5, as shown in Fig.32. The graph compares the response curve for large displacements with finite rotations to the response curve for moderate rotations, as well as the results for small displacements and limit load. It is worth noting that:

- the collapse load (dashed line), deduced by applying the kinematic theorem of the limit analysis with no cohesion represents the upper bound of the ultimate strength of the arch;
- the solution for small displacements (green line) asymptotically tends to the ultimate load;
- the response curves obtained with the implementation of finite rotations (blue star points) and moderate rotations (pink line) overlap;
- the analysis remains stable even when using a greater number of blocks compared to previous simulations. The results are consistent with those obtained in the simulations described in the previous sections (Sub. 7.1 and Sub. 7.2).

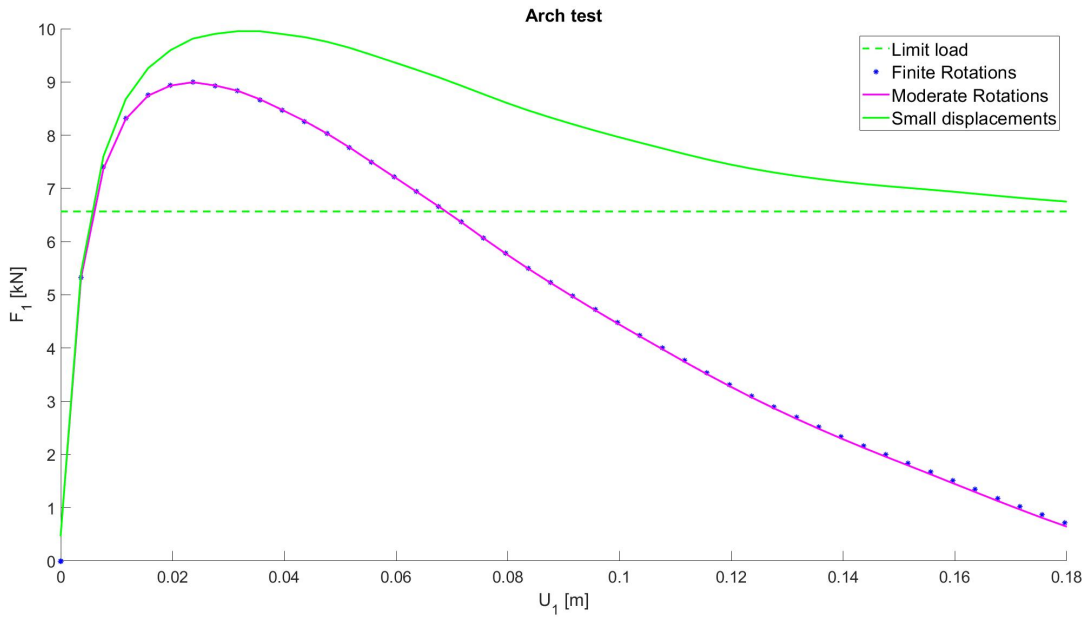

Figure 32: Horizontal reaction force F_1 [kN] as a function of the horizontal displacement U_1 [m] of the centroid of block 5: Limit load (dashed line) and numerical results obtained considering the Linear Theory (green line), Moderate Rotations (pink line), and Finite Rotations (blue star points).

```
Optimal solution found.

it =    1     err = 1.0000e+00
Optimal solution found.

it =    2     err = 5.6968e-15lambda = 9.5521e-02
Internal forces from equilibrium
interface =    1   Shear = -6.0912e+01     Normal = -2.2082e+02     Moment = -2.8323e+01
interface =    2   Shear = -6.3475e+00     Normal = -1.8266e+02     Moment = -1.0960e+02
interface =    3   Shear =  2.2651e+01     Normal = -1.3758e+02     Moment = -7.5188e+01
interface =    4   Shear =  2.4242e+01     Normal = -9.9938e+01     Moment =  2.5536e+00
interface =    5   Shear =  6.5672e+00     Normal = -8.2255e+01     Moment =  4.9353e+01
interface =    6   Shear = -1.6410e+01     Normal = -8.8730e+01     Moment =  3.5362e+01
interface =    7   Shear = -2.6582e+01     Normal = -1.1776e+02     Moment = -3.0943e+01
interface =    8   Shear = -1.1065e+01     Normal = -1.6120e+02     Moment = -9.6718e+01
interface =    9   Shear =  3.4594e+01     Normal = -2.0382e+02     Moment = -7.3530e+01
interface =   10   Shear =  9.9323e+01     Normal = -1.8131e+02     Moment =  1.0878e+02
```

Figure 33: Testing the circular arch of reference with the material 1 of Tab.5 for the interface: Upper-bound Limit Analysis algorithm to evaluate the Limit load [89].

The implemented interface model takes into account the coupling of mode I and mode II of fracture by defining the following mechanical parameters $\Delta\tilde{u}_n^0$, $\Delta\tilde{u}_n^f$, $\Delta\tilde{u}_t^0$, $\Delta\tilde{u}_t^f$. Tab.5 describes material 1 of the interface, which captures failure mode I as the actual mechanism.

Furthermore, Fig.34 illustrates the mechanism obtained under large displacements.

Tab.6 shows the hinge arrangement determined by the proposed model and compares it to the configurations corresponding to the two failure mechanisms identified in the investigations conducted by Como and Brandonisio. The pushover analysis produced results that closely align with those derived from limit analysis for the equilibrium configuration at $U_1 = 0.18$ m.

For such nonlinear problems, the absence of a unique solution is recognized, as opposed to limit analysis scenarios. Consequently, an exploration of the algorithm's functionality is initiated by increasing the block discretization from $n_b = 9$ to $n_b = 15$. Throughout the pushover analysis simulation, the interface material, constraint conditions, and loading conditions remain unchanged. Specifically, the horizontal displacement of the centroid of block 8 is monitored. The hinge positions obtained from the model with 15 blocks are also shown in Tab.6, and the corresponding configuration for a

horizontal displacement at the centroid of block 8 equal to 0.07 m is depicted in Fig.35.

Tab.6 compares the results of the proposed model with different discretization configurations (n_b) to those of benchmark case studies conducted by Como in 2013 and Brandonisio in 2017. The hinge mechanism's angular positions of hinge points (θ_A, θ_B, θ_C, θ_D) are used to present the results. It is evident that:

- The proposed model shows variations in the angular positions of hinge points as the number of blocks (n_b) used in discretization changes. This highlights the model's sensitivity to spatial resolution. Hinge points A and B show a variation of 8 degrees, while hinge point C shows a variation of 4 degrees. Hinge point D remains unchanged.

- Fig.36 shows a comparison of the load-displacement curves. The solid curves represent the behavior of the arch with $n_b = 9$, while the dashed curves represent the behavior with $n_b = 15$. The results are shown for both moderate rotations (pink lines) and small displacements (green lines). The star points and square points identify the solutions obtained with finite rotations. A change in discretization clearly affects the overall stiffness of the structure and its global response.

- Both obtained configurations agree with Como and Brandonisio's results in terms of hinge point positions and predicted collapse mechanism. This suggests that the proposed model accurately captures the system's behavior and provides consistent results with well-known benchmark cases.

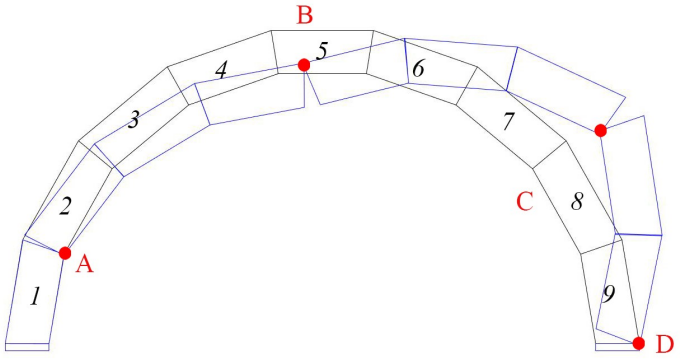

Figure 34: Configuration in large displacements of the arch with 9 rigid blocks and 10 interfaces (material 1 of Tab. 5) corresponding to the horizontal displacement of block 5 equal to 0.18 m. The positions of the hinges are marked with a red dot. The equilibrium configuration is plotted by applying a scale factor of 10.

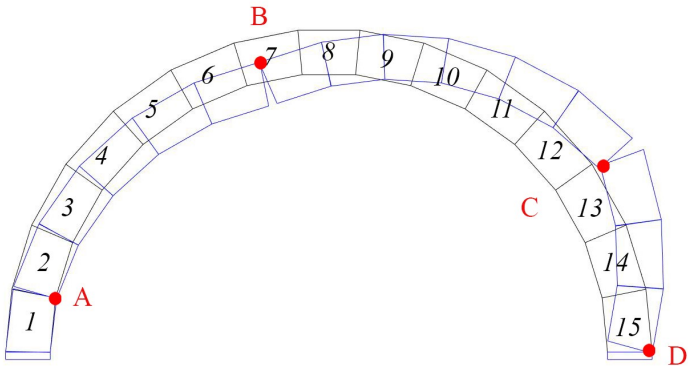

Figure 35: Configuration in large displacements of the arch with 15 rigid blocks and 16 interfaces (material 1 of Tab. 5) corresponding to the horizontal displacement of block 8 equal to 0.07 m. The positions of the hinges are marked with a red dot. The equilibrium configuration is plotted by applying a scale factor of 10.

Table 6: Comparison between the results of benchmark case studies and proposed numerical model procedure, in terms of equilibrium configuration at the end of the analysis for the proposed model (Pushover Analysis in Large Displacements, denoted PA) and in terms of collapse mechanism for the limit analysis with infinite friction procedure (denoted LA).

	θ_A	θ_B	θ_C	θ_D	Analysis Approaches
Proposed model with $n_b = 9$	20°	80°	140°	180°	PA
Proposed model with $n_b = 15$	12°	72°	144°	180°	PA
Como, 2013	25°	79°	141°	180°	LA
Brandonisio, 2017	28°	83°	135°	180°	LA

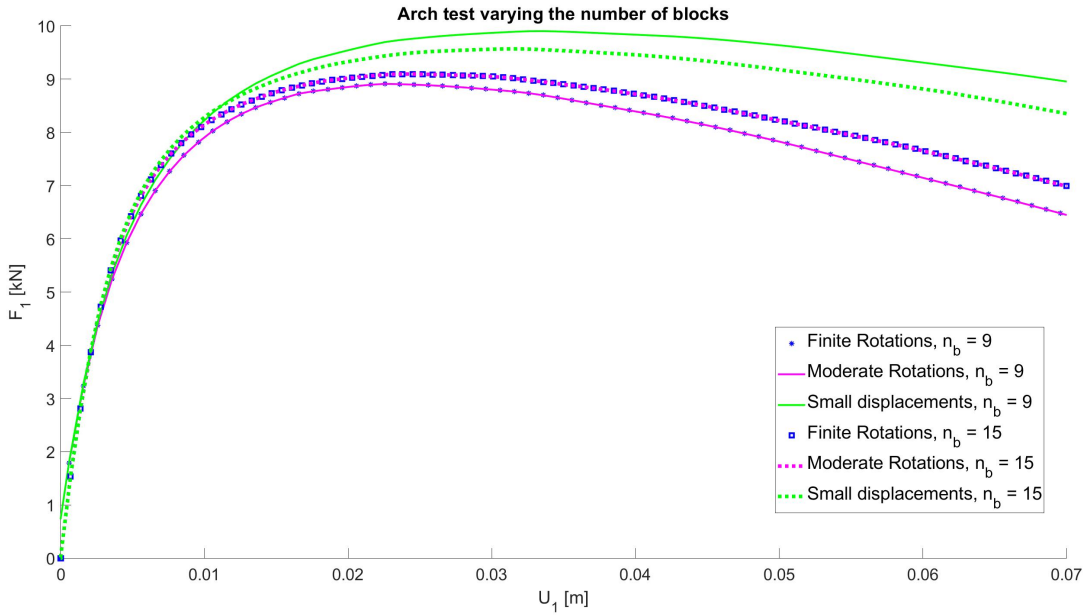

Figure 36: Horizontal reaction force F_1 [kN] is presented as a function of the horizontal displacement U_1 [m] for the centroids of block 5 in the case of the arch with $n_b = 9$ and block 8 in the case of the arch with $n_b = 15$. The solid curves depict the behavior of the arch with $n_b = 9$, while the dashed curves represent the behavior with $n_b = 15$. Results are shown for both moderate rotations (pink) and small displacements (green). Star points and square points identify the solutions obtained with finite rotations.

To analyze how the interface mechanical parameters and geometry affect the arch's behavior, addition simulations are performed with the following adoptions:

1. The friction coefficient value for material 2 in Tab.5 varies from 5 to 0.098.

2. The thickness value (t in Fig.31) varies from 1.2 m to 2.4 m. The computations

were performed considering the mechanical properties of the interface, which are indicated as material 1 and material 2 in Tab.8.

For the first study, the geometrical data and the constraint condition remain unchanged. During the simulation, the weight of the arch remains constant ($\gamma = 16$ kN/m^3), and the horizontal forces are applied at the centroids of blocks until block 5 reaches a horizontal displacement of 0.05 m. To accurately capture the mechanical response of the structure, a numerical analysis is performed with local control of the horizontal displacement at the centroid of block 5, U_1.

Figure 37 shows the equilibrium configuration of the arch model under large displacements. In this scenario, the value of μ is set to 0.098, and a horizontal displacement of 0.05 m is applied at the centroid of the key-block. The mechanical response of the structure is expressed in terms of the horizontal reaction force, F_1 [kN], versus the horizontal displacement component, U_1 [m], at the centroid of the controlled block 5, as shown in Fig.38. The graph compares the response curve for large displacements with finite rotations to the response curve for moderate rotations, and for small displacements. It is evident that:

- The study examines a new mechanism involving the sliding of block 9 in large displacements by varying the friction coefficient, as depicted in Fig.37.
- The solutions for large displacements shown in Fig.38 that implement finite rotations (star points) and those that approximate moderate rotations (pink line) overlap. In general, even in the case of sliding, the rotations are of such magnitude that the approximation of moderate rotations can be used without losing the same accuracy as the implementation of finite rotations.

Tab.7 compares the results of the proposed model with those of a benchmark case study using an Upper Bound Limit Analysis algorithm (see Figs.39-40).

In this limit analysis scenario, no-tension and frictional joints are considered, ignoring cohesion in both normal and tangential directions [89]. The hinge mechanism's

angular positions of hinge points (θ_A, θ_B, θ_C) are used to present the results. The proposed model only varies in the angular positions of hinge point θ_A. In both cases, the sliding involves the block 9. Generally, the mechanism obtained is the same, considering that the proposed model implements a cohesive interface. This suggests that the proposed model accurately captures the system's behavior and provides consistent results with the benchmark case.

Table 7: Comparison between the results of benchmark case studies and proposed numerical model procedure, in terms of equilibrium configuration at the end of the analysis for the proposed model (Pushover Analysis in Large Displacements, denoted PA) and in terms of collapse mechanism for the limit analysis procedure (denoted LA).

	θ_A	θ_B	θ_C	Analysis Approaches
Proposed model with $n_b = 9$	20°	80°	140°	PA
Lasorella, 2023	40°	80°	140°	LA

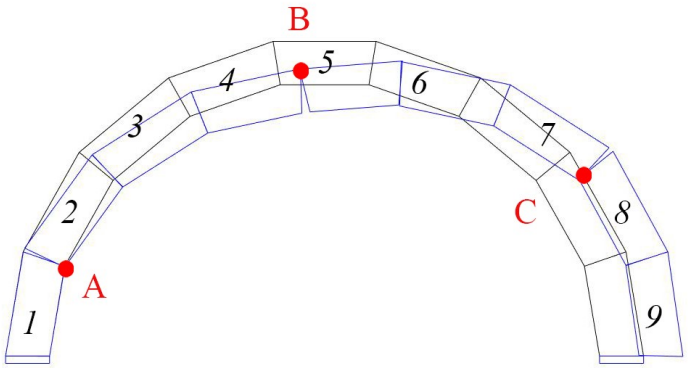

Figure 37: Configuration in large displacements of the arch with 9 rigid blocks and 10 interfaces (material 2 of Tab. 5) corresponding to the horizontal displacement of block 5 equal to 0.05 m. The positions of the hinges are marked with a red dot. The equilibrium configuration is plotted by applying a scale factor of 10.

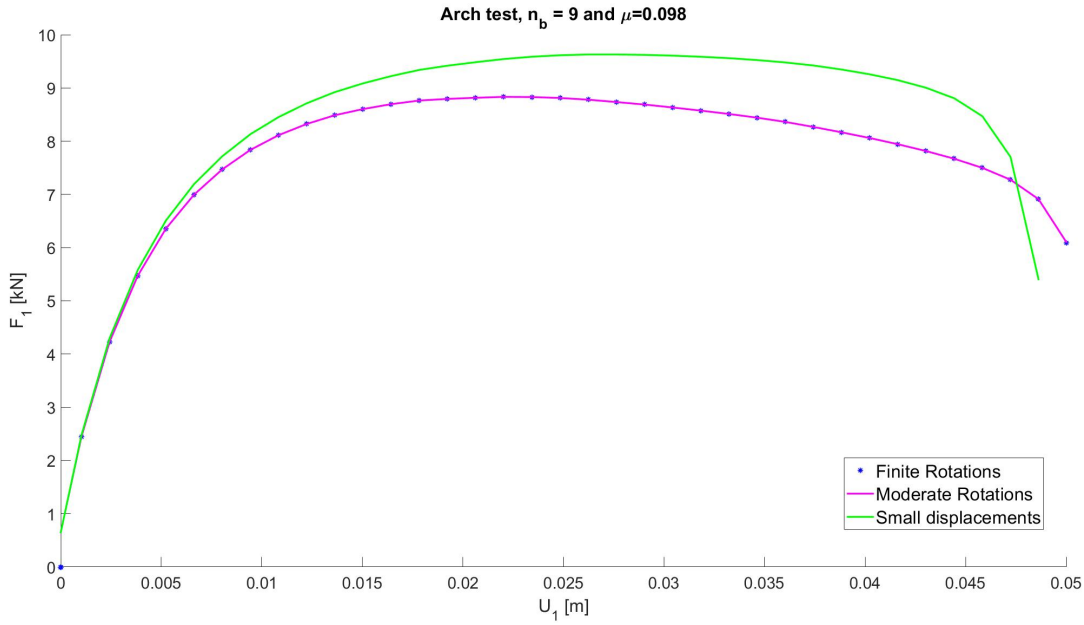

Figure 38: Horizontal reaction force F_1 [kN] as a function of the horizontal displacement U_1 [m] of the centroid of block 5: Numerical results obtained considering the Linear Theory (green line), Moderate Rotations (pink line), and Finite Rotations (blue star points), when $\mu = 0.098$.

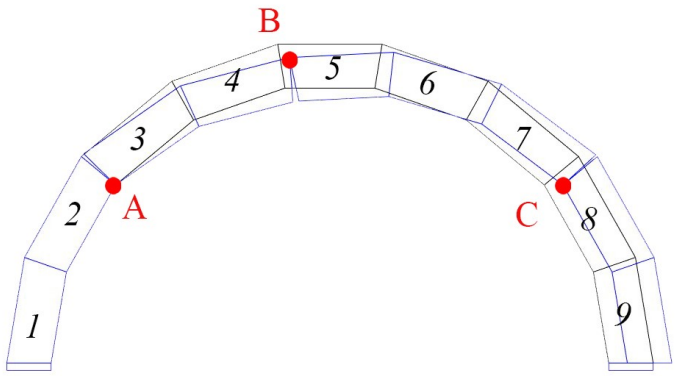

Figure 39: Testing the circular arch of reference with the material 2 of Tab.5 for the interface: Upper-bound Limit Analysis algorithm to evaluate the Limit load [89].

```
Optimal solution found.

it =    7     err = 3.4326e-05lambda = 5.0626e-02
Internal forces from equilibrium
interface =    1   Shear = -6.8865e+01     Normal = -2.2368e+02     Moment = -1.4041e+01
interface =    2   Shear = -1.0793e+01     Normal = -1.8723e+02     Moment = -1.1212e+02
interface =    3   Shear =  2.1839e+01     Normal = -1.4198e+02     Moment = -8.5188e+01
interface =    4   Shear =  2.6164e+01     Normal = -1.0237e+02     Moment = -5.3329e+00
interface =    5   Shear =  9.5696e+00     Normal = -8.1657e+01     Moment =  4.8994e+01
interface =    6   Shear = -1.4118e+01     Normal = -8.4979e+01     Moment =  4.2464e+01
interface =    7   Shear = -2.6815e+01     Normal = -1.1149e+02     Moment = -2.0406e+01
interface =    8   Shear = -1.5266e+01     Normal = -1.5398e+02     Moment = -9.2386e+01
interface =    9   Shear =  2.5983e+01     Normal = -1.9780e+02     Moment = -8.7826e+01
interface =   10   Shear =  8.9221e+01     Normal = -1.7844e+02     Moment =  6.9014e+01
```

Figure 40: Testing the circular arch of reference with the material 2 of Tab.5 for the interface: Upper-bound Limit Analysis algorithm to evaluate the Limit load [89].

For the second study, the geometrical data, except for thickness, and the constraint conditions remain unchanged. During the simulation, the weight of the arch remains constant ($\gamma = 16$ kN/m^3), and the horizontal forces are applied at the centroids of blocks until the block 5 reaches a horizontal displacement of 0.35 m. To fully capture the mechanical response of the structure, a numerical analysis is conducted with local control of the horizontal displacement at the centroid of block 5, U_1.

By varying the friction coefficient, one can observe that:

- When $\mu = 5$, a mechanism of 4 hinges is studied, as shown in Fig.41. Additionally, Fig.42 illustrates the response of the structure in terms of the horizontal reaction force, F_1 [kN], versus the horizontal displacement component, U_1 [m], at the centroid of the controlled block 5. The collapse load (dashed line), deduced by applying the kinematic theorem of the limit analysis with no cohesion represents the upper bound of the ultimate strength of the arch. In particular, the solution for small displacements (green line) asymptotically tends to the ultimate load, $F_{1lim} = 24.47$ kN. The response curves obtained with the implementation of finite rotations (blue star points) and moderate rotations (pink line) overlap.

- When $\mu = 0.08$, a mechanism involving three hinges (θ_A, θ_B, θ_C) and the sliding of block 9 is studied, as shown in Fig.43. This mechanism is the same as the one

studied for the arch with $t = 1.2$ m and $\mu = 0.098$. It is formed by two intrados rotation hinges near each of the arch springs, an extrados rotation hinge close to the arch key, and sliding of the arch at one of its springs. It is a typical mechanism for low-friction values [90].

Additionally, Fig.44 shows the response of the structure in terms of the horizontal reaction force, F_1 [kN], versus the horizontal displacement component, U_1 [m], at the centroid of the controlled block 5. The solutions in small and large displacements are nearly overlapping. The solution obtained from linear theory is equivalent to that of nonlinear theory because the displacement obtained is very small compared to the dimensions of the structure, $\frac{U_{1fin}}{t} = \frac{1}{60}$.

The analysis remains stable even when using a larger value of thickness compared to previous simulations. The results are consistent with those obtained in the simulations described above with $t = 1.2$ m.

When analyzing a thick arch like this compared to the previous reference by Como and Brandonisio, one would expect a stiffer overall response of the structure. This is indeed observed when comparing the study of the arch for $t = 1.2$ m and $t = 2.4$ m.

Referring to Figs. 34, 35, 37, 41 and Fig.43, it is evident that the numerical simulations accurately predict the collapse kinematics, including overturning and sliding mechanisms.

Table 8: Interface mechanical properties adopted for the analysis of the arch with $t = 2.4$ m.

	K_n [kN/m^3]	K_t [kN/m^3]	$\Delta\tilde{u}_n^0$ [m]	$\Delta\tilde{u}_n^f$ [m]	$\Delta\tilde{u}_t^0$ [m]	$\Delta\tilde{u}_t^f$ [m]	μ
1	1000000	1000000	0.005×10^{-2}	0.05	0.02×10^{-1}	0.05	5
2	1000000	1000000	0.005×10^{-2}	0.05	0.02×10^{-1}	0.05	0.08

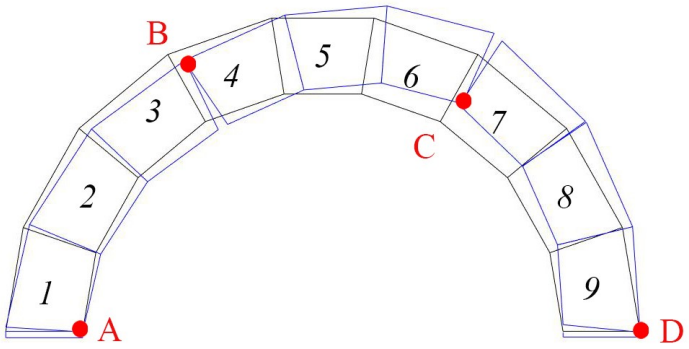

Figure 41: Configuration in large displacements of the arch with 9 rigid blocks and 10 interfaces (material 1 of Tab. 8) corresponding to the horizontal displacement of block 5 equal to 0.35 m. The positions of the hinges are marked with a red dot. The equilibrium configuration is plotted by applying a scale factor of 10.

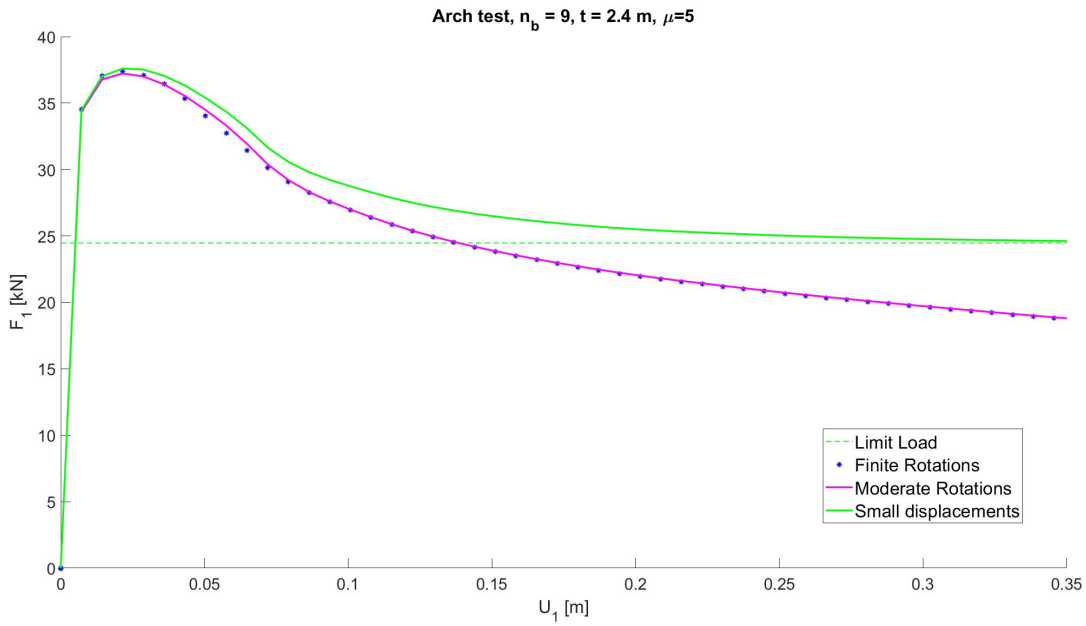

Figure 42: Horizontal reaction force F_1 [kN] as a function of the horizontal displacement U_1 [m] of the centroid of block 5: Limit load (dashed line) and numerical results obtained considering the Linear Theory (green line), Moderate Rotations (pink line), and Finite Rotations (blue star points), when $t = 2.4$ m and $\mu = 5$.

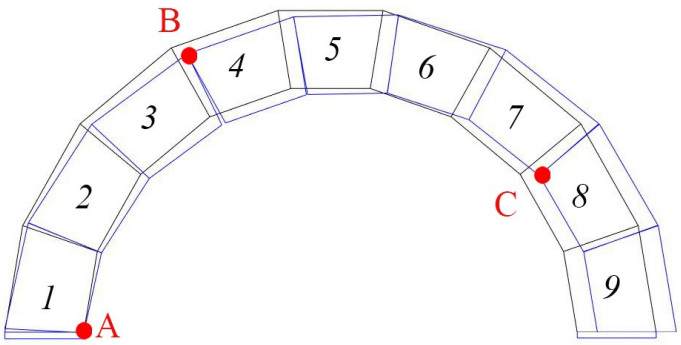

Figure 43: Configuration in large displacements of the arch with 9 rigid blocks and 10 interfaces (material 2 of Tab. 8) corresponding to the horizontal displacement of block 5 equal to 0.04 m. The positions of the hinges are marked with a red dot. The equilibrium configuration is plotted by applying a scale factor of 10.

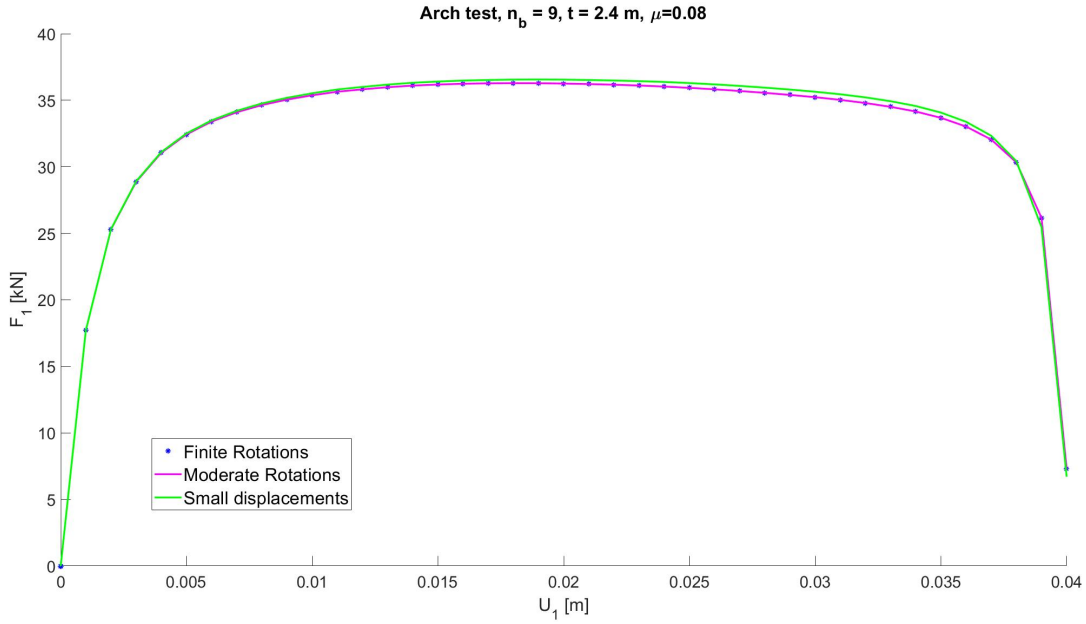

Figure 44: Horizontal reaction force F_1 [kN] as a function of the horizontal displacement U_1 [m] of the centroid of block 5: Numerical results obtained considering the Linear Theory (green line), Moderate Rotations (pink line), and Finite Rotations (blue star points), when $t = 2.4$ m and $\mu = 0.08$.

8 Conclusion

This dissertation proposes the 2D-Rigid Block Model with Interfaces for analyzing masonry structures, considering geometrical and material nonlinearity. The cohesive zone model, which combines damage and friction with geometrical nonlinearity, is implemented as a constitutive model for interface elements in the discrete element code.

The present model is formulated for large displacements by introducing a co-rotational reference system that aligns with the middle-line between the two deformed sides of the interface shared by two rigid blocks. The derivation process begins with analyzing the interface's contribution to the Principle of Virtual Work, which involves virtual variation, discretization, and linearization. The use of rigid body kinematics has made the models more complex compared to deformable bodies, which may be unexpected. The proposed formulation is not only simple and compact but also operationally efficient, distinctly identifying the contributions of both geometrical and material aspects to the interface stiffness matrix.

The dissertation has been presented and discussed the theoretical formulation and numerical procedure of the rigid block model with geometrical and material nonlinearity, covering three main scenarios: large displacements with finite rotations, large displacements approximating moderate rotations, and small displacements.

This model was used to develop simple structural analyses. The simulations involve large displacements with finite rotations and the approximation of moderate rotations. The results, in terms of response curves, are compared with those obtained in small displacements and the limit load. The simulations demonstrate the accuracy and convergence of the numerical procedure.

Finally, there is a specific focus on masonry arches. The proposed model's numerical results were compared to the literature references, confirming a satisfactory agreement in terms of failure mechanism. This demonstrates the algorithm's ability to predict the collapse kinematics, including overturning and sliding mechanisms.

However, the simulations presented in this dissertation demonstrate that the failure

mechanisms of isolated masonry arches can be studied using linear theory. Therefore, implementing large displacements in this type of problem is unnecessary. On the other hand, when dealing with massive structures such as trilithon structures, implementing large displacements allows for the study of specific scenarios that cannot be analyzed through linear theory alone.

Additionally, the response curves obtained from considering finite rotations were compared to those obtained from approximating moderate rotations. For larger rotations and displacements, approximating moderate rotations may result in inaccuracies. The decision to use finite rotations or moderate rotations should be based on the specific application and precision requirements of the problem. Based on the cases examined in this dissertation, it is clear that the solution provided by moderate rotations closely approximates the solution obtained by implementing finite rotations in large displacements. Moderate rotations can be as effective as finite rotations in analyzing the behavior of masonry structures. This approach also reduces the computational burden of the highly nonlinear problem, which considers the interaction between material and geometrical nonlinearity. This evidence is interesting for future development of the 3D model as it reduces computation cost without sacrificing appreciation of nonlinear response.

This research paves the way for the study of the effect of large displacements in more complex masonry structures, where elements such as round arches or triumphal arches are integrated into large structures such as historical masonry churches. The seismic behavior of historical buildings is a complex task due to several reasons. These include limited knowledge of material properties, highly nonlinear behavior of masonry, and the complexity of geometric configuration. Seismic analysis of historical masonry buildings can be complex due to the dynamic response of the structure. Therefore, it is necessary to implement large displacement in an iterative analysis approach to analyze them.

When analyzing seismic phenomena, second-order geometrical nonlinearity is acti-

vated. Neglecting the study of nonlinearities by evaluating the governing equations of the problem in the undeformed configuration is to be avoided. Only by using models like the one proposed in this dissertation, which consider large displacements, is it possible to undertake a study that allows investigating the actual behavior of a masonry structure. When considering a frame subject to seismic forces, which are more complex than a theoretical sinusoidal force, it displaces the structure. When the structure is subjected to force again, it will clearly be in a deformed configuration, different from the initial one. To appreciate this phenomenon, it is necessary to use a model that accounts for large displacements.

The present model is suitable for dynamics involving rocking motion phenomena, typically when masonry structures are subjected to seismic loads. For future applications, the system of inertial forces should be included as external forces acting on the structure. To enhance the code for the dynamic part, it is necessary to solve a time differential equation. This requires studying and implementing appropriate techniques, such as the Newmark method. Another aspect to address, related to the use of rigid bodies in dynamics, is the problem of impact. Within the code, while working in dynamics, it will be necessary to introduce coefficients that simulate impact dissipation.

Because the code is developed and implemented in-house, It is possible and easy to extend the model for dynamics (or to implement other aspects), which underlines the versatility of the presented tool. Therefore, when performing the structural analysis of masonry, the user must interpret the results instead of relying solely on the code. In this open context, the user can interact with the model while considering the nature of the problem and the structure.

References

[1] D.S. Dugdale. Yielding of steel sheets containing slits. *J. Mech. Phys. Solids*, vol. 8, no. 2, pp. 100–104, 1960.

[2] G.I. Barenblatt. The mathematical theory of equilibrium cracks in brittle fracture. *Adv. Appl. Mech.*, vol. 7, pp. 55–129, 1962.

[3] G. Housner. The behavior of inverted pendulum structures during the earthquakes. *Bull. Seismol. Soc. Am.*, vol. 53, pp. 403–417, 1963.

[4] J. Heyman. The stone skeleton. *International Journal of solids and structures*, 2 (2): 249-279, 1966.

[5] O.C. Zienkiewicz, S. Valliappan, and I.P. King. Stress analysis of rock as a 'no-tension' material. *Geotechnique*, 18: 56-66, 1968.

[6] A. Cundall. A computer model for simulating progressive, large-scale movements in blocky rock systems. *Proceedings of the Symposium of the International Society of Rock Mechanics*, Nancy, France, vol. I, paper II–8, 1971.

[7] T. Kawai. A new discrete analysis of nonlinear solid mechanics problems involving stability, plasticity and crack. *Proceedings of the Symposium on Applications of Computer Methods in Engineering*, Los Angeles, Calif., pp. 1029–1038, 1977.

[8] A. Page. Finite element model for masonry. *ASCE J Struct Div.*, 104, pp. 1267–1285, 1978.

[9] G. Romano and M. Romano. Sulla soluzione di problemi strutturali in presenza di legami costitutivi unilateri. *Rendiconto dell'Accademia Nazionale dei Lincei*, 67, pp. 104–113, 1979.

[10] E. Benvenuto. La Scienza delle Costruzioni e il suo sviluppo storico. *Sansoni*, Roma, 1981.

[11] A.K. Noor, J.M. Peters, and C.M. Andersen. Mixed models and reduction techniques for large-rotation nonlinear problems. *Comput Methods Appl Mech Eng*, 44(1), pp.67–89, 1984.

[12] G. Romano and E. Sacco. Analisi limite e collasso plastico per materiali non standard ben posti. *Riv. Ital. Geotecnica*, 1, pp. 37–41, 1985.

[13] K. Meguro and M. Hakuno. Fracture analyses of structures by the modified distinct element method, *Struct. Engrg./Earthquake Engrg.*, 6(2), 283s-294s, 1989.

[14] G. Del Piero. Constitutive equation and compatibility of the external loads for linear elastic masonry like materials. *Meccanica*, 24, pp. 150–162, 1989.

[15] A. Hillerborg. Fracture mechanics concepts applied to moment capacity and rotational capacity of reinforced concrete beams. *Eng Fract Mech*, 35, pp. 233–240, 1990.

[16] A. Needleman. An analysis of decohesion along an imperfect interface. *Int. J. Fract.*, vol. 42, no. 1, pp. 21–40, 1990.

[17] E. Sacco. Modellazione e calcolo di strutture in materiale non resistente a trazione. *Atti della Accademia Nazionale dei Lincei. Classe di Scienze Fisiche, Matematiche e Naturali. Rendiconti Lincei. Matematica e Applicazioni, Serie 9*, 1(3): 235–258, 1990.

[18] G. Crisfield. Nonlinear Finite Element Analysis of Solids and Structures. *Essentials, Wiley and Sons*, Vol. 1, pp. 266–276, 1991.

[19] E. Sacco and J.N. Reddy. On first and second-order moderate rotation theories of laminated plates. *International Journal for Numerical Methods in Engineering*, Vol. 33, pp. 1–17, 1992.

[20] G.H. Shi. Discontinuos Deformation Analysis: A new numerical model for the static and dynamic of deformable block structures. *Engineering Computations*, Vol. 9, Iss. 2, pp. 157–168, 1992.

[21] M. Angelillo. Costitutive relations for no-tension materials. *Meccanica*, 28, pp. 195–202, 1993.

[22] D. De Tommasi and S. Marzano. Small strain and moderate rotation. *J. Elasticity*, 32, pp. 37–50, 1993.

[23] B. Wang and V.K. Garga. A numerical method for modeling large displacements of jointed rocks-Part I: fundamentals. *Can Geotech J*, 30, pp. 96–108, 1993.

[24] M. Xiong and Q. Lingxi. Rigid finite element and limit analysis. *Acta Mech Sinica*, 9, pp. 156–162, 1993.

[25] S.G. Creaghan and A.N. Palazotto. Nonlinear large displacement and moderate rotational characteristics of composite beams incorporating transverse shear strain. *Computers and Structures*, 51(4), pp. 357–371, 1994.

[26] M. Gilbert and C. Melbourne. Rigid-block analysis of masonry structures. *Struct. Eng*, 72 (21):356–361,1994.

[27] H.R. Lotfi and P.B. Shing. Interface Model Applied to Fracture of Masonry Structures. *Journal of Structural Engineering*, vol. 120, No. 1, pp. 63–80, 1994.

[28] T.C. Ke. The issue of rigid-body rotation in DDA. *Proceedings of the first international forum on Discontinuous Deformation Analysis (DDA) and simulations of discontinuous media. USA: TSI Press*, pp. 318–25,1996.

[29] P.B. Lourenço. Computational strategies for masonry structures. *PhD dissertation, Delft University of Technology*, 1996.

[30] M.M. MacLaughlin and N. Sitar. Rigid body rotations in DDA. *Proceedings of the first international forum on Discontinuous Deformation Analysis (DDA) and simulations of discontinuous media. USA: TSI Press*, pp. 620–35, 1996.

[31] L. Gambarotta and S. Lagomarsino. Damage Models for the Seismic Response of Brick Masonry Shear Walls, Part I: The Mortar Joint Model and its Applications. *Earthquake Engineering and Structural Dynamics*, vol. 26, pp. 423–439, 1997.

[32] G. Giambanco and L. Di Gati. A Cohesive Interface Model for the Structural Mechanics of Block Masonry. *Mechanics Renear and Communications*, vol.24, no. 5, pp. 503–512, 1997.

[33] P.B. Lourenço and J.G. Rots. A multi-surface interface model for the analysis of masonry structures. *Journal of Engineering Mechanics*, 123(7): 60–668, 1997.

[34] C. Baggio and P. Trovalusci. Limit analysis for no-tension and frictional threedimensional discrete systems. *Mech Struct Mach*, 26(3):287–304, 1998.

[35] C.Y. Koo and J.C. Chern. Modification of the DDA method for rigid block problems. *Int J Rock Mech Mining Sci*, 35:683–93, 1998.

[36] O. Allix and A. Corigliano. Geometrical and interfacial non-linearities in the analysis of delamination in composites. *Int. J. Solids Struct.*, vol. 36, no. 15, pp. 2189–2216, 1999.

[37] M. Ortiz and A. Pandolfi. Finite deformation irreversible cohesive elements for three-dimensional crackpropagation analysis. *Int J Num Meth Engng*, 44:1267–1282, 1999.

[38] B. Skallerud and B. Haugen. Collapse of thin shell structures: Stress resultant plasticity modeling within a co-rotated ANDES finite element formulation. Int. J. Numer. Methods Engrg., 46:1961–1986, 1999.

[39] J.C. Simo and T.J.R. Hughes. Computational Inelasticity. *Springer*, New York, 2000.

[40] Y. Qiu, M.A. Crisfield, and G. Alfano. An interface element formulation for the simulation of delamination with buckling. *Eng. Fract. Mech.*, vol. 68, no. 16, pp. 1755–1776, 2001.

[41] M.C. Ferris and F. Tin-Loi. Limit analysis of frictional block assemblies as a mathematical program with complementarity constraints. *Int J Mech Sci*, 43:209–224, 2001.

[42] M. Gilbert. RING: A 2D rigid-block analysis program for masonry arch bridges, pp. 459–464, 2001.

[43] A. Becchi and F. Foce. Degli archi e delle volte: arte del costruire tra meccanica e stereotomia. *Marsilio*, Venezia, Italy, 2002.

[44] K. Meguro and H. Tagel-Din. Applied Element Method Used for Large Displacement Structural Analysis. *Journal of Natural Disaster Science*, 24, pp. 25–34, 2002.

[45] J. Ochsendorf. Collapse of masonry structures. *PhD Dissertation, Department of Engineering, Cambridge University*, 2002.

[46] G.N. Wells, R. de Borst, and L.J. Sluys. A consistent geometrically non-linear approach for delamination. *Int. J. Numer. Methods Eng.*, vol. 54, no. 9, pp. 1333–1355, 2002.

[47] A. Pandolfi. Corso: Analisi non lineari di strutture con il metodo degli Elementi Finiti. 2003.

[48] P. Trovalusci and R. Masiani. Non-linear micropolar and classical continua for anisotropic discontinous materials. *Int. J. Solids Struct.*, 40, pp. 1281–1297, 2003.

[49] A. Cecchi and K. Sab. A comparison between a 3D discrete model and two homogenized plate models for periodic elastic brickwork. *Int J Solids Struct*, 41:2259–2276, 2004.

[50] A. Muñjiza. The Finite/Discrete Element Method. *John Wiley and Sons*, Chicester, England, 2004.

[51] G. Alfano and E. Sacco. Combining Interface Damage and Fiction in a Cohesive-zone Model. *International Journal for Numerical Methods in Engineering*, Vol. 68, pp. 542–582, 2006.

[52] G. Alfano, E. Sacco, and S. Marfia. Interface Model Accounting for Water Pressure on Crack Propagation. *Computer Methods in Applied Mechanics and Engineering*, Vol. 196, pp. 192–209, 2006.

[53] S. Huerta. Structural Design in the Work of GaudÃ. *Architectural Science Review*, 49(4), pp. 324–339, 2006.

[54] J.V. Lemos, J.V. Discrete element modeling of masonry structures. *Int. J. Arch. Herit.*, 1, pp. 190–213, 2007.

[55] F. Peña, P.B. Lourenço, and C. Costa. Experimental Dynamic Behavior of Free-Standing Multi-Block Structures Under Seismic Loadings. *Journal of Earthquake Engineering*, Vol. 12, pp. 953–979, 2008.

[56] M.G. Botero. Finite element formulation for large displacement analysis. 2009.

[57] E. Sacco. A nonlinear homogenization procedure for periodic masonry. *European Journal of Mechanics - A/Solids*, Vol. 28, pp. 209–222, 2009.

[58] E. Sacco and J. Toti. Interface Elements for the Analysis of Masonry Structures. *International Journal for Computational Methods in Engineering Science and Mechanics*, 11:6, pp. 354–373, 2010.

[59] Q. Ma and J. Butterworth. Simplified Expressions for Modelling Rigid Rocking Structures on Two-spring Foundations. *Bulletin of the New Zealand Society for Earthquake Engineering*, Vol. 45, pp. 31–39, 2012.

[60] R. Marques and P.B. Lourenço. Pushover seismic analysis of quasi-static tested confined masonry buildings through simplified model. In: *Proceedings of the 15th international brick and block masonry conference*, Florianopolis, 2012.

[61] M. Como. Statics of Historic Masonry Constructions. *Springer Verlag,Berlin-Heidelberg*, 2013.

[62] S. Nazir and M. Dhanasekar. Modelling the failure of thin layered mortar joints in masonry. *Engineering Structures*, Vol. 49, pp. 615–627, 2013.

[63] K.J. Bathe. Finite Element Procedures. *Prentice-Hall*, pp. 485–538, 2014.

[64] M. Paggi and J. Reinoso. A consistent interface element formulation for geometrical and material nonlinearities. *Computational Mechanics*, Vol. 54, pp. 1569–1581, 2014.

[65] A.D.M.S. Borri and A. De Maria. Indice di QualitÃ Muraria (IQM): correlazione con le caratteristiche meccaniche e livelli di conoscenza. *Progettazione sismica 3*, 2015.

[66] W. Jiang and H. Zhen. An efficient remedy for the false volume expansion of DDA when simulating large rotation. *Computers and Geotechnics*, Vol. 70, pp. 18–23, 2015.

[67] D. Addessi and E. Sacco. Nonlinear analysis of masonry panels using a kinematic enriched plane state formulation. *International Journal of Solids and Structures*, Vol. 90, pp. 194–214, 2016.

[68] C. Casapulla, L. Giresini, and P.B. Lourenço. Rocking and Kinematic Approaches for Rigid Block Analysis of Masonry Walls: State of the Art and Recent Developments. *Buildings*, 7(3):69, 2017.

[69] A. Chiozzi, G. Milani, and A. Tralli. A Genetic Algorithm NURBS-based new approach for fast kinematic limit analysis of masonry vaults. *Computers and Structures*, 182, pp. 187–204, 2017.

[70] D. Baraldi and A. Cecchi. A full 3D rigid block model for the collapse behaviour of masonry walls. *European Journal of Mechanics - A/Solids*, Vol. 64, 2017.

[71] E. Bertolesi, G. Milani, and S. Casolo. Homogenization towards a mechanistic Rigid Body and Spring Model (HRBSM) for the non-linear dynamic analysis of 3D masonry structures. *Meccanica*, 53, pp. 1–37, 2017.

[72] G. Brandonisio, E. Mele, and A. De Luca. Limit analysis of masonry circular buttressed arches under horizontal loads. *Meccanica*, Vol. 52, pp. 2547–2565, 2017.

[73] A. Orduña. Non-linear static analysis of rigid block models for structural assessment of ancient masonry constructions. *International Journal of Solids and Structures*, Vol. 128, pp. 23–35, 2017.

[74] D. Baraldi, E. Reccia, and A. Cecchi. In plane loaded masonry walls: DEM and FEM/DEM models. A critical review. *Meccanica*, 53: 1613–1628, 2018.

[75] A.M. D'Altri, S. de Miranda, G. Castellazzi, and V. Sarhosis. A 3D detailed micromodel for the in-plane and out-of-plane numerical analysis of masonry panels. *Computers and Structures*, Vol. 206, pp. 18–30, 2018.

[76] A.M. D'Altri, V. Sarhosis, G. Milani, J. Rots, S. Cattari, S. Lagomarsino, E. Sacco, A. Tralli, G. Castellazzi, and S. de Miranda. A review of numerical models for masonry structures. *Numerical Modeling of Masonry and Historical Structures, Elsevier*, pp. 3–53, 2019.

[77] S. Degli Abbati, A.M. D'Altri, D. Ottonelli, G. Castellazzi, S. Cattari, S. de Miranda, and S. Lagomarsino. Seismic assessment of interacting structural units in complex historic masonry constructions by nonlinear static analyses. *Computers and Structures*, 213, pp. 51–71, 2019.

[78] A. Fraddosio, N. Lepore, and M.D. Piccioni. Thrust Surface Method: An innovative approach for the three-dimensional lower bound Limit Analysis of masonry vaults. *Engineering Structures*, 202, 2020.

[79] F.P.A. Portioli. Rigid block modelling of historic masonry structures using mathematical programming: a unified formulation for non-linear time history, static pushover and limit equilibrium analysis. *Bulletin of Earthquake Engineering*, Vol. 18, pp. 211–239, 2020.

[80] A. Castellano, A. Fraddosio, M. Piccioni, E. Ricci, and E. Sacco. Experimental Data for the Calibration of a Non-Linear Numerical Model for Describing the Response of Masonry Constructions under Cyclic Loading. *12th International Conference on Structural Analysis of Historical Constructions*, 2021.

[81] R. Gagliardo, F.P.A. Portioli, L. Cascini, R. Landolfo, and P.B. Lourenço. A rigid block model with no-tension elastic contacts for displacement-based assessment of historic masonry structures subjected to settlements. *Engineering Structures*, Vol. 229, 2021.

[82] Y. Liu, J. Páez Chávez, P. Brzeski, and P. Perlikowski. Dynamical response of a rocking rigid block. *Chaos: An Interdisciplinary Journal of Nonlinear Science*, 31(7), 2021.

[83] M. Pepe, M. Pingaro, and P. Trovalusci. Limit analysis approach for the in-plane collapse of masonry arches. *Proceedings of the Institution of Civil Engineers - Engineering and Computational Mechanics*, 174(2):66–81, 2021.

[84] A. Pagani, R. Azzara, B. Wu, E. Carrera. Effect of different geometrically nonlinear strain measures on the static nonlinear response of isotropic and composite shells with constant curvature. *Int J Mech Sci*, 209, pp. 106713, 2021.

[85] F.P.A. Portioli, M. Godio, C. Calderini, and P.B. Lourenço. A variational rigid-block modeling approach to nonlinear elastic and kinematic analysis of failure mechanisms in historic masonry structures subjected to lateral loads. *Earthquake Engineering & Structural Dynamics*, 50(12): 3332–3354, 2021.

[86] G. Borino and F. Parrinello. A symmetric tangent stiffness approach to cohesive mechanical interfaces in large displacements. *International Journal for Computational Methods in Engineering Science and Mechanics*, 23(6): 551–566, 2022.

[87] G. Milani and V. Sarhosis. (eds) From Corbel Arches to Double Curvature Vaults: Analysis, Conservation and Restoration of Architectural Heritage Masonry Structures. Springer Nature, 2022.

[88] S.D. Torre and L. Cantini. Historical Review of Masonry Arches and Vaults. Trends in Historic Preservation and the Relevance of Understanding Curved Masonry Structures. *In: Milani, G., Sarhosis, V. (eds) From Corbel Arches to Double Curvature Vaults. Research for Development*, Springer, Cham., 2022.

[89] M. Lasorella. Optimal design of reinforcement of masonry arches. *Phd Thesis*, Politecnico di Bari, 2023.

[90] A. Jiménez Rios, B. Nela, M. Pingaro, E. Reccia, and P. Trovalusci. Parametric analysis of masonry arches following a limit analysis approach: Influence of joint friction, pier texture, and arch shallowness. *Math. Mech. Solids*, 10812865231175385, 2023.

[91] F. Nerilli. Novel Lagrangian-based and NURBS-based beam elements for the modeling of no-tension masonry arch. *Structures*, Elsevier, Vol. 61, p. 105985, 2024.